Observation and analysis of unexplored low-energy electron emission processes revealed using a low-energy positron beam

by

Alexander Jarrett Fairchild

Presented to the faculty of the Graduate School of the University of Texas at Arlington in partial fulfillment of the requirements for the degree of

Doctor of Philosophy

The University of Texas at Arlington

August, 2020

Supervising Committee:

Alexander H. Weiss, Supervising Professor

Varghese A. Chirayath

Muhammad N. Huda

Ali R. Koymen

Joseph Ngai

Qiming Zhang

Dedication

Acknowledgments

Abstract

Observation and analysis of unexplored low-energy electron emission processes revealed using a low-energy positron beam

Alexander Jarrett Fairchild, Ph.D

The University of Texas at Arlington, 2020

Supervising professor: Alexander Herman Weiss

This dissertation presents measurements of the kinetic energy distributions of low-energy, positron-induced electrons emitted from single-layer of graphene (SLG), highly oriented pyrolytic graphite (HOPG), Si, Cu and TiO_2 surfaces. The electron kinetic energies were measured using UTA's 1m flight path ToF spectrometer attached to a variable energy positron beam. The unique capability of this system to transport extremely low-energy positrons ($\sim$1 eV) to the sample surface while simultaneously measuring the energies of outgoing electrons with high collection efficiencies down to 0 eV has made possible the measurement of the full, background-free spectra of electrons

emitted as a result of annihilation-induced Auger transitions. These capabilities have enabled the measurements presented here, which provide an unambiguous identification of the hitherto unexplored LVV Auger transition in oxygen and the first direct observation of an Auger process occurring entirely within the valence band of SLG. The TiO_2 O LVV and SLG VVV line shapes have been theoretically investigated using a first principals-based model which incorporates the distribution of annihilation-induced holes, the self-convolution of the valence band density of states (DOS), and estimates of the electron escape probabilities. These results have important implications for the understanding of Auger-stimulated ion desorption, Coulombic decay, photodynamic cancer therapies, and may yield important insights into the radiation-induced reactive sites for corrosion and catalysis. Numerical simulations of the ToF spectrometer have made possible the direct comparison between the measured and calculated line shapes and have allowed the characterization of the system's transport efficiency, timing resolution, and energy resolution for the set of low-energy transport settings used in this work. Lastly, measurements of the kinetic energy distributions of electrons emitted as a result of Auger-mediated positron sticking (AMPS) at the surfaces of Cu, HOPG, SLG, and Si are presented and analyzed. First principles based modeling of the AMPS line shape provides an estimate of the positron surface state binding energy and suggests that a more detailed analysis may provide the basis for a novel, top-layer selective positron-induced electron spectroscopy.

Table of Contents

List of Figures

List of Tables

Chapter 1

Introduction

1.1 Overview

In this dissertation, I will present the results of simulations and experiments using a time-of-flight positron annihilation-induced Auger electron spectrometer (ToF-PAES) to measure low-energy electron emission following the incidence of low-energy positrons. The major results of this work are summarized below.

1. Numerical simulations of UTA's time-of-flight positron annihilation-induced Auger electron spectrometer (ToF-PAES) have enabled the characterization of the system's transport efficiency, timing and energy resolution, and instrument response function for the set of low-energy transport settings used in this work. The simulations of the electron transport through the ToF-PAES spectrometer indicate a nearly 100% transport efficiency to the electron detector for electron energies 1 to 200 eV. The simulated relative energy resolution is less than 25% for electron

energies from 1 to 1000 eV. The timing resolution was found to be 2.35 ns. The instrumental contributions to the measured electron energy spectra predicted by these numerical simulations have made possible the detailed comparison of experimentally measured and theoretically generated spectra.

2. We present direct evidence of a hitherto unexplored O LVV Auger transition occurring at oxygen-exposed Cu and Si surfaces and a TiO_2 surface. We have calculated theoretically the O LVV electron energy distribution from TiO_2 using a first principals based model which incorporates the self-convolution of the density of states, an estimate of the distribution of annihilation-induced O 2s holes, and an estimate of the electron escape function. We found excellent agreement between the measured O LVV Auger spectrum from the TiO_2 surface and this calculation. We have estimated the positron annihilation probability with the oxygen 2s levels at the surface of TiO_2 using the measured O LVV and O KVV integrated PAES intensities and calculated them theoretically. The agreement between our measured and theoretical ratio supports the idea that O LVV Auger processes are highly efficient.

3. We present the first direct observation and investigations of Auger processes occurring entirely within the valence band of single-layer graphene (SLG). We have calculated theoretically the C VVV electron energy distribution from SLG using a first principals based model which incorporates the self-convolution of the density of states, the distribution of annihilation-induced O 2s holes, and an estimate of the electron escape

function. We found excellent agreement between the measured C VVV Auger spectrum and this calculation. We have estimated the efficiency of the C VVV Auger process to be between 0.8 and 1 by comparing a theoretical calculation of the ratio of the C VVV to C KVV integrated intensities to the measured ratio.

4. Finally, we have measured and modelled the Auger-mediated positron sticking (AMPS) line shapes from HOPG and Si. The experimental spectra were decomposed into two modelled spectra, one containing electrons emitted as a result of positron annihilation-induced Auger processes and one containing electrons emitted as a result of AMPS processes. The AMPS line shapes have been understood in terms of the density of states, the positron beam kinetic energy distribution, and the electron escape function. The modelled AMPS line shapes have provided estimates of the positron surface state binding energies and suggests that a more detailed analysis may provide the basis for a novel, top-layer selective positron-induced electron spectroscopy.

1.2 Background

This section will provide a brief introduction to the following topics:

1. Positron-Matter Interactions

2. Positron annihilation-induced Auger electron spectroscopy (PAES)

1.2.1 Positron-Matter Interactions

Positrons can have numerous interactions with the atoms of a solid. Fig. 1.1 provides a visual overview of the most common positrons-matter interactions. Each of these interactions forms the basis of a positron spectroscopy which as a class have become established, non-destructive techniques in the study of the atomic, electronic, and chemical structure of condensed matter systems [1, 2, 3]. In this dissertation, we will concern ourselves solely with the interactions of positrons at surfaces. That is to say, with the thermalization and diffusion of positrons to the surface and the channels of secondary electron emission, positronium formation, and annihilation-induced Auger emission.

After implantation, positrons thermalize within picoseconds. If the implantation energy is less than a few keV, then the majority of implanted positrons will diffuse to the surface [3]. After diffusing to the surface, positrons can be emitted as an epithermal positrons, be emitted as positronium, or become trapped in the surface state and annihilate. If the implantation energy is low, less than 100 eV, then these processes are roughly equally likely [4].

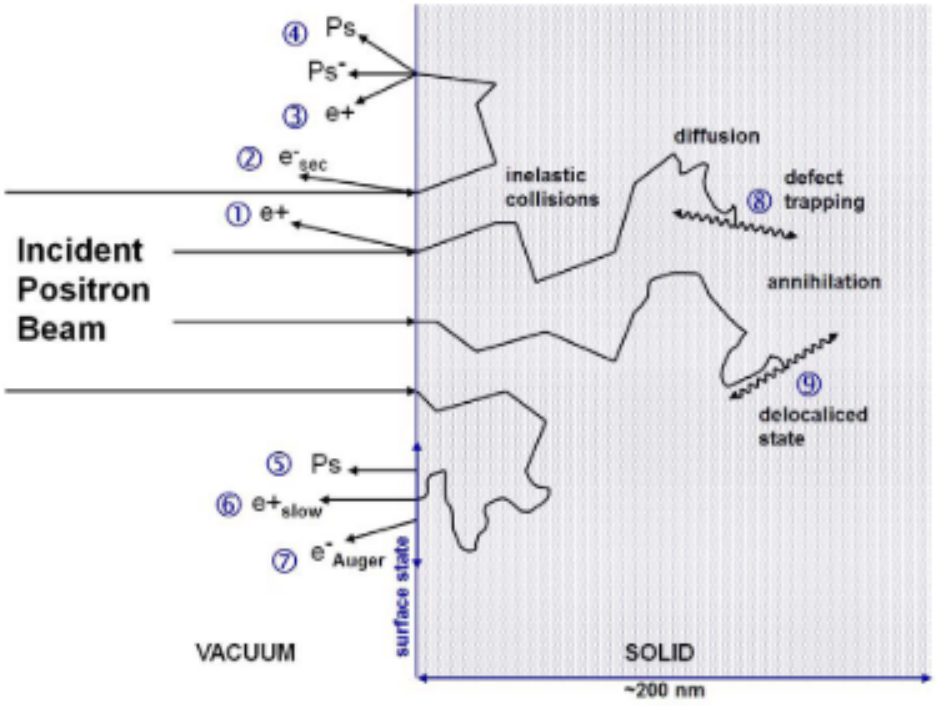

Figure 1.1: Visual overview of positron interactions with matter. At the surface positrons can: (1) be reflected and diffracted, (2) eject secondary electrons, (3) be emitted as epithermal positrons, or (4) as positronium. After thermalization and diffusion to the surface positrons can (5) be emitted as positronium, (6) be emitted as moderated positrons, or (7) can annihilate in the surface state causing Auger electron emission. In the bulk, positrons annihilate either (8) after defect trapping, or (9) as delocalized positrons. Taken from [3].

1.2.2 Positron Annihilation-induced Auger Electron Spectroscopy (PAES)

Positron annihilation-induced Auger electron spectroscopy (PAES) is a non-destructive surface analysis technique with top-most atomic layer selectivity. In PAES, a surface trapped positron annihilates with a surface bound electron resulting in the emission of an electron via an Auger process. This Auger process occurs when a less tightly bound electron comes to occupy the energy level of the hole, coupling the energy associated with this filling of the hole to a third electron, which escapes into the vacuum. The Auger process is schematically represented in fig. 1.2. For studying clean and adsorbate covered surfaces, Auger electron spectroscopy (AES) has found widespread success and has become an almost indispensable technique for determining surface cleanliness, adsorbate coverage, and surface electronic information [5].

In PAES, positron beam energies well below the electron work function can be used to initiate the Auger process allowing for the complete elimination of the obscuring secondary electron background found in other similar techniques [6]. Fig. 1.3 illustrates schematically the different excitation methods between electron-stimulated and positron annihilation-induced Auger electron spectroscopy. In EAES, electrons with a few keV are required to ionize the atoms by impact generating large secondary electron backgrounds. In PAES, arbitrary low incident positron beam energies can be used which means the secondary electron background can be minimized or eliminated entirely. This is illustrated in fig. 1.4 in which EAES and PAES measurements of Cu(100) are compared. In the EAES measurement the Cu $M_{2,3}VV$ peak appears only as a small shoulder but in the PAES measurement the peak is clearly

defined. This experimental determination of the background-free, spectra of electrons emitted as a result of Auger transitions, down to 0 eV, is important for unravelling the complex, correlated Auger decay pathways of core and deep valence holes [7, 8, 9, 10, 11].

An added advantage of using positron annihilation to initiate the Auger process is the selectivity to the top-most atomic layer due to the trapping of the positrons at the image potential-induced well on the vacuum side of the sample surface [12, 13]. This is illustrated in fig. 1.5 in which PAES measurements were made of a Cu sample with varying sub-monolayer coverages of S. The Cu $M_{2,3}VV$ Auger signal nearly disappears entirely with only a half monolayer of S. The surface selectivity of PAES stems from the fact that the positron wave function in the surface state decays rapidly below the top-most atomic layer. This is shown in fig. 1.6 in which the positron ground-state probability density and potential are calculated for a single-layer of graphene on Cu. The wave function of the surface trapped positron rapidly decays and has appreciable overlap solely with electrons of the surface terminating atomic species. Thus, the majority of the annihilation-induced holes and the resulting Auger electrons originate almost entirely from the top-most atomic layer.

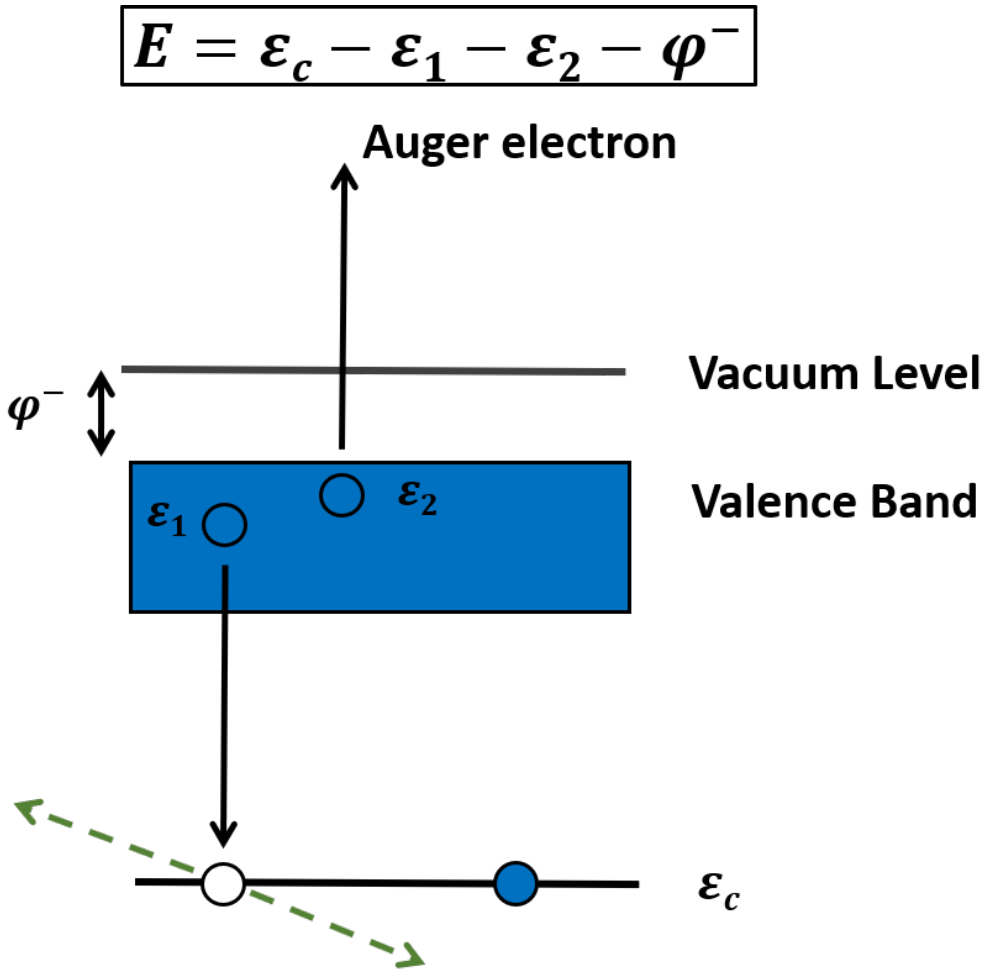

Figure 1.2: Schematic representation of the positron-induced Auger process. A positron annihilates with a core electron at the surface. The resulting core hole decays via an Auger transition in which a valence electron comes to occupy the core hole energy level. The energy associated with this core hole filling is coupled to another valence electron in the solid which escapes into the vacuum.

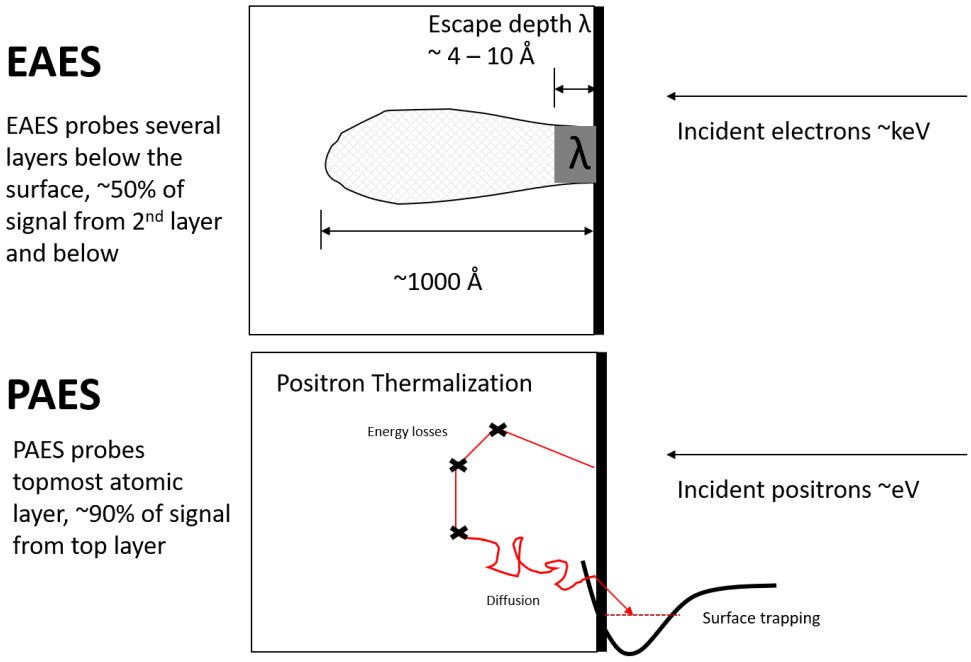

Figure 1.3: Schematic representation comparing the Auger excitation mechanisms between EAES and PAES. In EAES, the Auger process is initiated by impact ionization requiring an incident beam energy of a few keV. The surface sensitivity of the Auger signal originates from the escape depth of the Auger electrons which is typically a few atomic layers. In PAES, the Auger process is initiated through annihilation requiring only a few eV incident beam energy. The surface sensitivity originates from annihilation in the surface state with selectively to the top-most atomic layer.

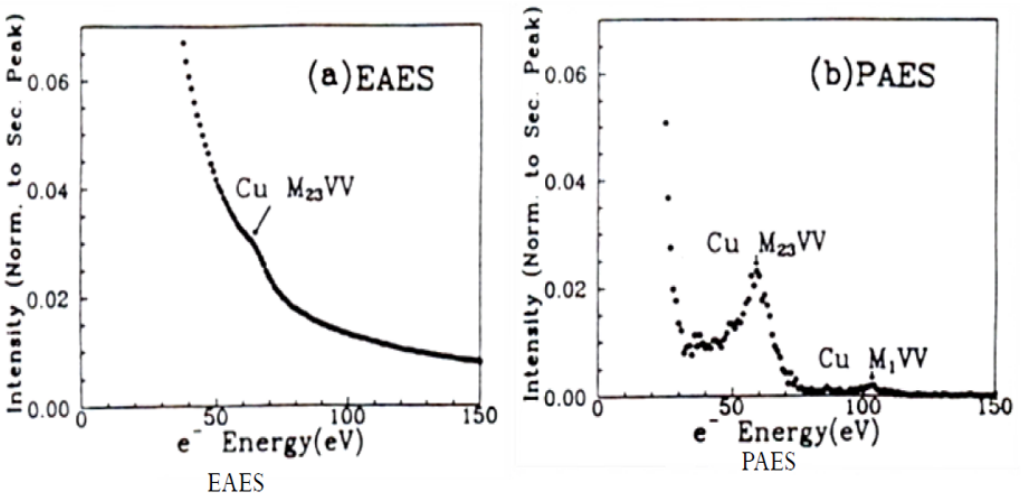

Figure 1.4: Comparison of PAES and EAES spectra from Cu(100). The incident beam energies were 3 keV and 25 eV for the electron and positron beam respectively. Data taken from [14].

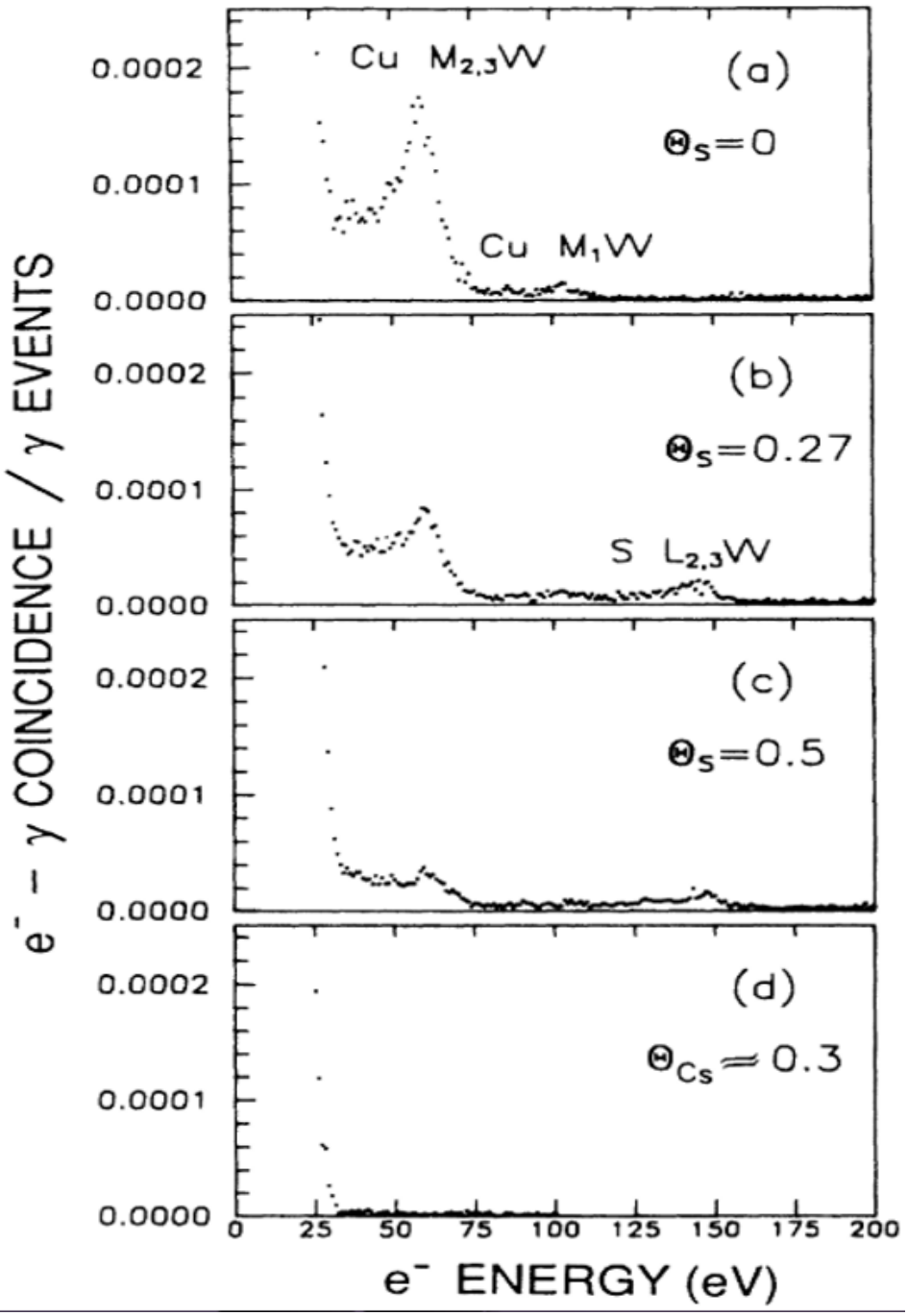

Figure 1.5: Positron annihilation induced Auger spectra of Cu with various sub-monolayer coverages of S or Cs. Data taken from [12].

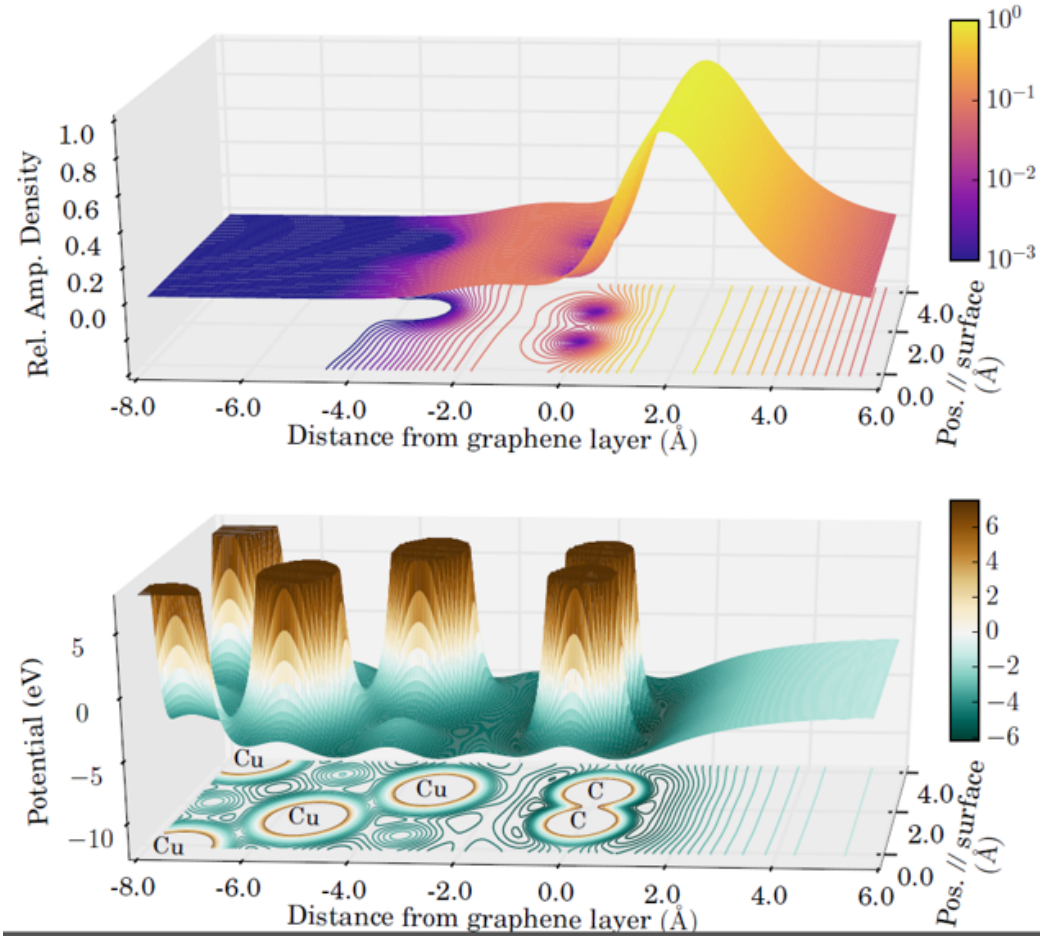

Figure 1.6: Theoretical calculation of the ground-state positron probability density (top) and potential (bottom) experienced by the positron near the surface of SLG on Cu(111). The decay of the positron wave function as it penetrates the solid explains the origin of the surface selectivity of PAES.

1.3 Dissertation Outline

This dissertation is organized as follows: chapter 1 will begin with an overview and introduction of this dissertation including the brief review of PAES and positron surface physics, chapter 2 will provide a detailed description of UTA's ToF-PAES apparatus, chapter 4 will present the results of measurements of O LVV Auger electron emission from oxide surfaces, chapter 5 will present the results of measurements of VVV Auger electron emission, and chapter 6 will present results of the measurement and analysis of the line shape of Auger-mediated positron sticking (AMPS).

Chapter 2

Experimental ToF-PAES Apparatus

2.1 Introduction

The purpose of this chapter is to describe and discuss the topics which relate to the time-of-flight positron annihilation-induced Auger electron spectrometer (ToF-PAES) used in the measurements presented in this dissertation. The unique capability of the University of Texas at Arlington's ToF-PAES system to transport extremely low-energy positrons ($\sim$1 eV) to the sample surface while simultaneously measuring the energies of outgoing electrons, emitted over a nearly 2π solid angle, with kinetic energies ranging from 0 eV to 1000 eV, has made possible the measurement, down to 0eV, of the full, background-free spectra of electrons emitted as a result of annihilation-induced Auger transitions.

An overview of the experimental apparatus is given in section 2.2. An

introduction to the ultra-high vacuum (UHV) system is given in section 2.3. Details of the positron beam generation and transport will be given in section 2.4. The detection and data acquisition system will be discussed in section 2.5. The methodologies for converting the measured electron ToF spectra to electron kinetic energy spectra will be given in section 2.6.

2.2 Overview of the Apparatus

The positron beam system at UTA is comprised of three parts: a positron beam with magnetic transport, a ToF energy spectrometer, and a sample preparation chamber. More complete descriptions of the system and its capabilities have been published previously [6, 15]. A schematic drawing of the apparatus is provided in fig. 2.1. The whole system is 5.5 meters end-to-end. The radioactive source chamber is located at the south end while the sample preparation chamber is at the north end. A UHV gate valve (MDC GV 1500M) is placed between the radioactive source chamber and the rest of the system. Another UHV gate valve is placed between the micro-channel plate (MCP) chamber and the sample preparation chamber in order to keep the source and MCP chambers under UHV during sample introduction, cleaning, and preparation.

Fast positrons from a ^{22}Na source are moderated using a thin tungsten foil in transmission geometry and are guided toward the sample by an axial magnetic field produced by a series of Helmholtz coils. These moderated positrons are drifted underneath the MCP assembly by an $\mathbf{E}\times\mathbf{B}$ field and then drifted back onto the beam axis by an additional $\mathbf{E}\times\mathbf{B}$ field. The

slow positrons arriving at the sample are focused by a strong magnetic field gradient produced by a permanent magnet mounted a few mm behind the sample. A majority of the incident positrons will eventually annihilate with electrons of the sample producing either two or three gamma photons. Some of the time, these positron-electron interactions at the surface will result in the emission of Auger or secondary electrons. These outgoing electrons have their momentum parallelized by the magnetic field gradient, are guided to the MCP by the axial magnetic field, and finally, are drifted vertically onto the MCP detector plates. The sample is mounted on a linear transfer arm capable of moving the sample between the analysis position and the sample preparation chamber. The sample can be biased using a copper feedthrough in order to change the kinetic energies of the incident positrons.

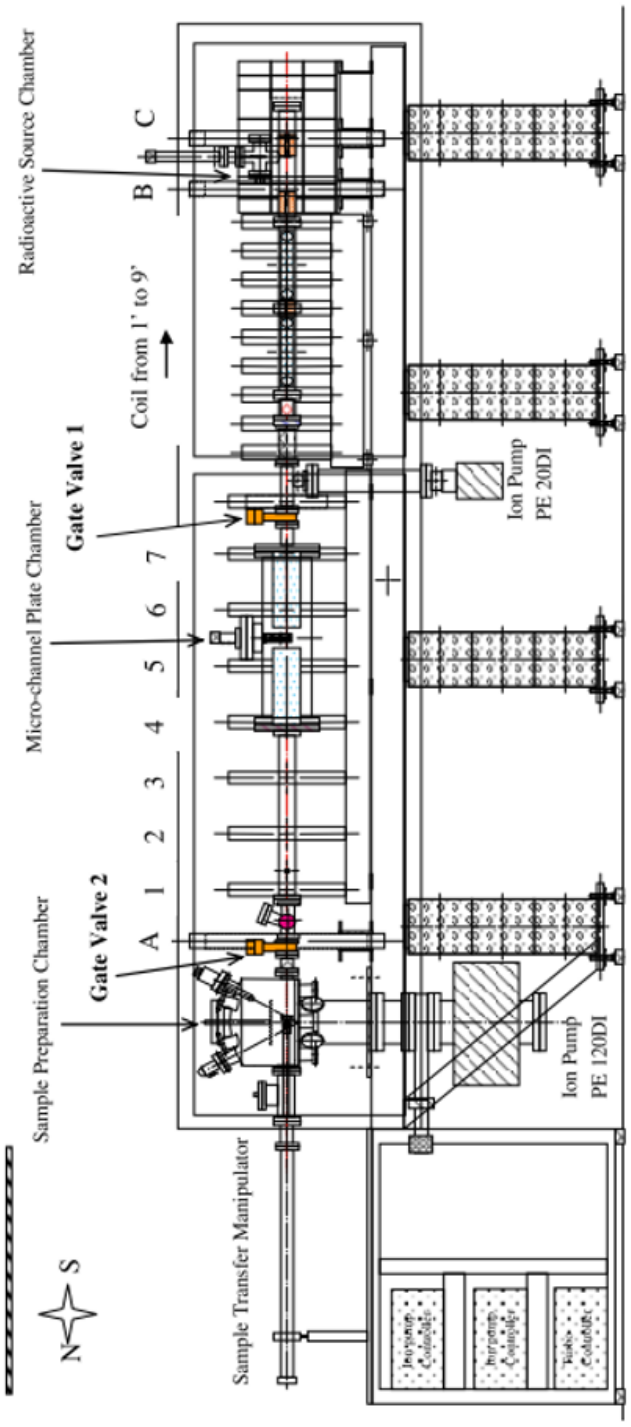

Figure 2.1: Schematic diagram of the UTA positron beam system. The red circle near gate valve 2 indicates the location of the sample during measurements.

2.3 Ultra-High Vacuum System

Ultra-high vacuum is characterized by pressures lower than $\sim 10^{-9}$ torr (10^{-7} pascal or 10^{-9} mbar). UHV pressures are necessary in order to maintain contaminant free surfaces for the duration of the experiment and to permit the transport of electrons and positrons through the system. Since the mean free path of a gas molecule in UHV is over 40 km, any electrons or positrons travelling through the system are extremely unlikely to encounter any residual gas molecules. Residual gases will also, over time, contaminate the surface. The monolayer formation time, which is the amount of time required for a surface to form 1 monolayer of adsorbed atoms or molecules at room temperate, is given by:

$$t_{ML} = \frac{2.25 \times 10^{-6}\, torr \cdot seconds}{P} \tag{2.1}$$

where the sticking probability is assumed to be unity and P is the pressure in torr. For a chamber keep at merely a high vacuum pressure of 2×10^{-6} torr it takes $\sim$1 s for a monolayer to form. It is impossible to conduct the experiments detailed in this dissertation in a matter of seconds and hence UHV is required.

The UHV vacuum system uses a rotary vane pump, a turbomolecular pump, two ion pumps, and a titanium sublimation pump (TSP) to achieve UHV pressures. The pressure is monitored using an Bayard-Alpert ionization gauge installed in the sample preparation chamber. The procedure to achieve UHV after the sample preparation chamber has been vented to atmosphere will now be sketched. First, the rotary vane pump works from atmosphere down to mm torr range, which is monitored using a cathode gauge mounted

above the pump. Next, the sample chamber is heated uniformly to ∼100 °C with the rotary vane pump on to remove water vapor from the chamber walls. The table of heater tape currents is listed in table 2.1. After two days the pressure should be low 10^{-6} torr and the heater tapes are turned off. The chamber is allowed to pump for a day with the turbomolecular on. After a day the pressure should reach low 10^{-8} torr and the ion pumps can be switched on. This will bring the chamber to low 10^{-10} torr from which the pressure can be lowered further using the TSP. This system is capable of maintaining sample chamber pressures less than 1×10^{-10} torr just through firing of the TSP several times a week.

Heater Tape	Current (A)
1	1.0
2	1.0
3	1.0
4	1.0
5	2.0
6	2.0
7	2.0
8	2.0

Table 2.1: Heater tape currents used to bake the sample preparation chamber.

2.4 Positron Beam Production and Transport

In this section, information concerning the positron beam production and transport is given. A schematic representation of the positron source chamber is given in fig. 2.3. The source of positrons is radioactive ^{22}Na which undergoes β decay, whereby a proton is converted to a neutron emitting a positron and a neutrino:

$$^{22}_{11}Na \rightarrow {}^{14}_{2}Ne + {}^{0}_{1}e + {}^{0}_{0}\nu_e \tag{2.2}$$

The β^+ spectrum from ^{22}Na is schematically represented in fig. 2.2. The relatively long half-life for ^{22}Na ($\sim$2.6 years) has ensured widespread use. The high-energy and extremely broad positron kinetic energy distribution is ill suited for controlled experiments and so the emitted fast positrons are moderated to lower kinetic energies. The long life time means the positron count rate is constant over typical experiment times. The source is housed in an assembly and shielded using lead.

The moderation process is done using a 1 μm thick, 9 mm diameter polycrystalline tungsten foil in transmission geometry. It works because tungsten has a negative positron work function. The positrons thermalize inside the W, diffuse to the surface and are emitted with energy equal to the work function. Tungsten has -3.0 eV positron work function [**citation**]. The width of the energy distribution is given by thermal distribution. The moderation process efficiency is $\sim 10^{-4}$.

Some amount of high-energy positrons remain in the beam despite the presence of the tungsten moderator requiring additional energy filtering.

Additional, energy filtration is done using tungsten barriers, B and A in fig. 2.3 in combination with the **E**×**B** plates between the barriers, labeled A. Tuning the **E**×**B** plate voltages allows the user to reduce the maximum energy of the incoming positron beam since positrons with too high energy with not experience enough vertical drift make it to the off-center aperture in tungsten barrier B. A large asymmetric voltage ensures that no secondary electrons generated along the way contaminate the beam.

The ToF tube was used as a retarded field analyzer to measure the axial component of the positron beam's kinetic energy distribution by recording the MCP counts as a function of the positive retarding bias on the ToF tube. The spectrum was differentiated using a centroid differential method. The resulting positron kinetic energy distribution is shown in fig. 2.4. The Helmholtz coil currents, **E**×**B** voltages, and moderator and source bias utilized to generate the positron beam and transport the low-energy electrons is listed in table 2.2. Coil values are read from the ammeters given the convention that a positive current means red to + and black to -.

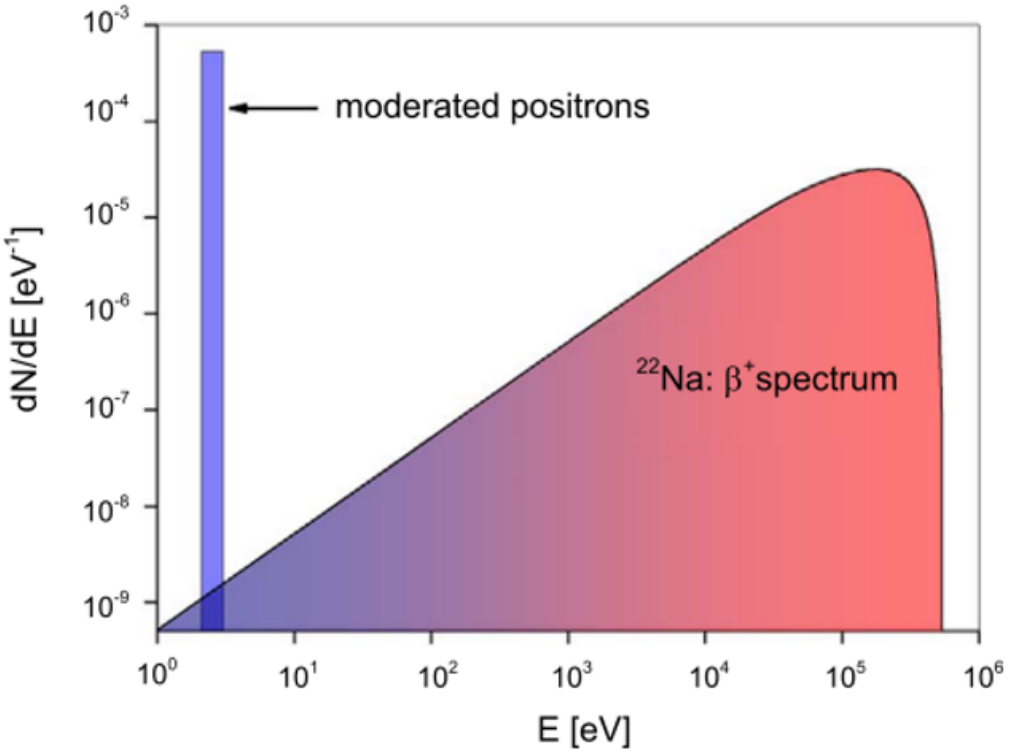

Figure 2.2: Schematic representation of the β^+ spectrum of ^{22}Na and the positron intensity after moderation. Taken from reference [3].

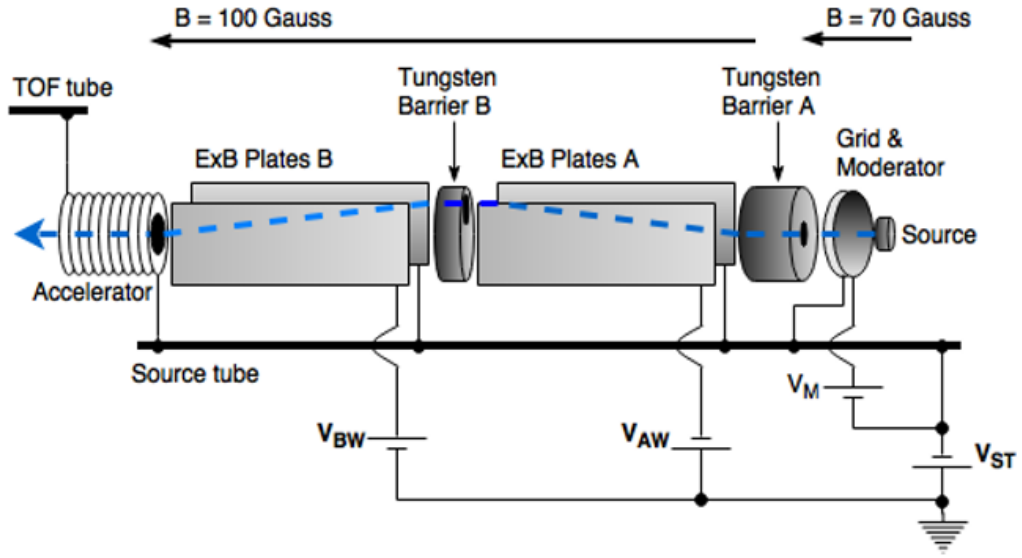

Figure 2.3: Schematic representation of the positron source chamber.

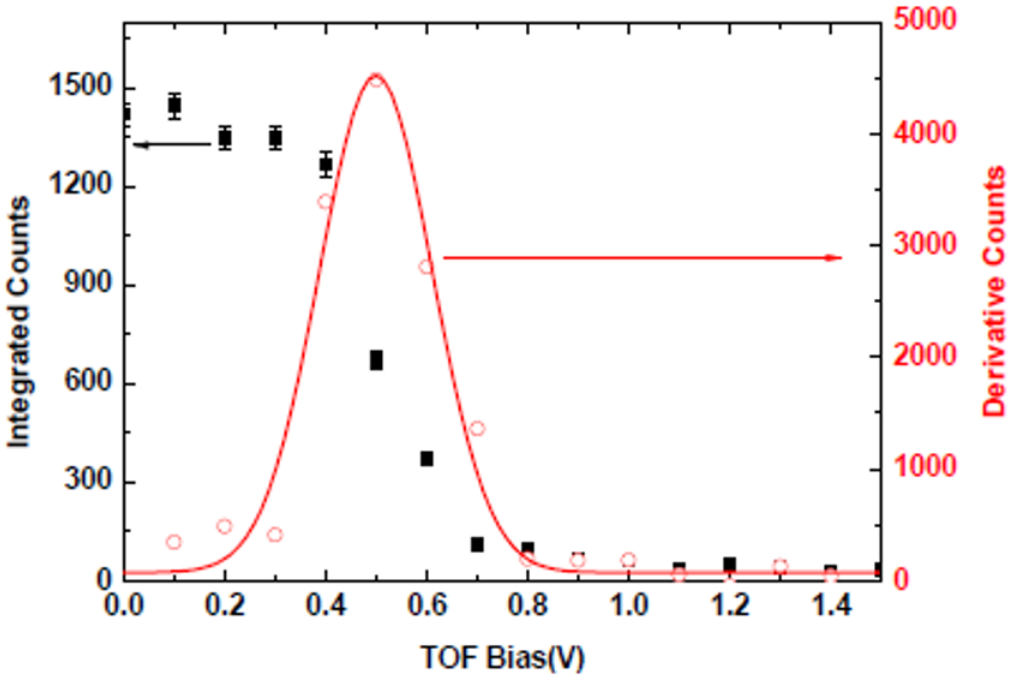

Figure 2.4: Positron beam kinetic energy distribution measured at the ToF tube.

Item	Voltage (V)	Helmholtz Coil	Current (A)
Moderator	-.832	Coil 1	+4.5
Source Tube	-15.80	Coil 2	+3.2
E×**B** 1W	+5.512	Coil 3	+2.7
E×**B** 1E	-15.81	Coil 4	+9.0
E×**B** 2W	-85.6	Coil 4'	+7.7
E×**B** 2E	-15.81	Coil 5	-2.25
E×**B** 3W	+3.193	Coil 6	-1.0
E×**B** 3E	-2.797	Coil 7	+2.1
E×**B** 4W	-2.797	Coil 8	-3.2
E×**B** 4E	+3.193		

Table 2.2: Voltage and current settings used to generate a 1 eV positron beam. The Helmholtz coil currents, **E**×**B** voltages, moderator voltage, and source tube voltage settings that result in a positron beam kinetic energy distribution that peaks at 0.5 eV, has a 0.25 eV FWHM, and a maximum kinetic energy of 1 eV. All values are referenced with respect to chamber ground.

2.5 ToF Spectrometer

A schematic representation of the ToF spectrometer is presented in fig. 2.5. Moderated positrons coming from the source chamber are drifted under the MCP and back onto the beam using an $\mathbf{E}\times\mathbf{B}$ field. The slow positrons arriving at the sample are focused by a strong magnetic field gradient produced by a permanent magnet mounted a few mm behind the sample. A majority of the incident positrons will eventually annihilate with electrons of the sample producing either two or three gamma photons. Some of the time, these positron-electron interactions at the surface will result in the emission of Auger or secondary electrons. These outgoing electrons have their momentum parallelized by the magnetic field gradient, are guided to the MCP by the axial magnetic field, and finally, are drifted vertically onto the MCP detector plates.

The ToF of the electrons is measured as the time difference between the detection of the 511 keV annihilation gamma rays by a fast scintillator, BaF_2 or NaI(Tl), and the detection of the electrons by a microchannel plate (MCP). The high voltage bias applied to the BaF_2 is -1640 V while NaI is +900 V. The MCP anode voltage is +2910 V and front plate +200 V. A schematic representation of the coincidence timing circuit is shown in fig. 2.6. The output signal of the fast scintillator and MCP are fed into constant fraction discriminators (CFD, Canberra 2126). Typical threshold voltages for the CFD are 70 mV for the fast scintillator and 10 mV for the MCP. The outputs are fed into gate and delay generators (Ortec 416A). The scintillate output is delayed by 3.2 μs and is used as the STOP signal into a time-to-amplitude converter (TAC, ORTEC 437A). The MCP signal out of the CFD is used

as the START signal for the TAC. This results in a reverse timing signature that helps reduce the accidental coincidence count rate and reduce the dead time of the TAC. the TAC window is set at 4 μs, 10 V max, and 1 Ω. The TAC output is a voltage pulse proportional to the time difference between the START and STOP inputs. The TAC signal is fed to a multichannel analyzer (MCA). The resulting histogram of times is recorded using a computer.

The recorded ToF histograms are converted to electron ToF by:

$$ToF(\mu s) = \left(TAC - \frac{TAC \cdot \#}{MCA}\right) - \left(TAC - \frac{TAC \cdot INFINITY}{MCA}\right) \quad (2.3)$$

For the measurements in this dissertation, TAC = 4 μ s, MCA = 2048 channels. # is the bin (channel) number.

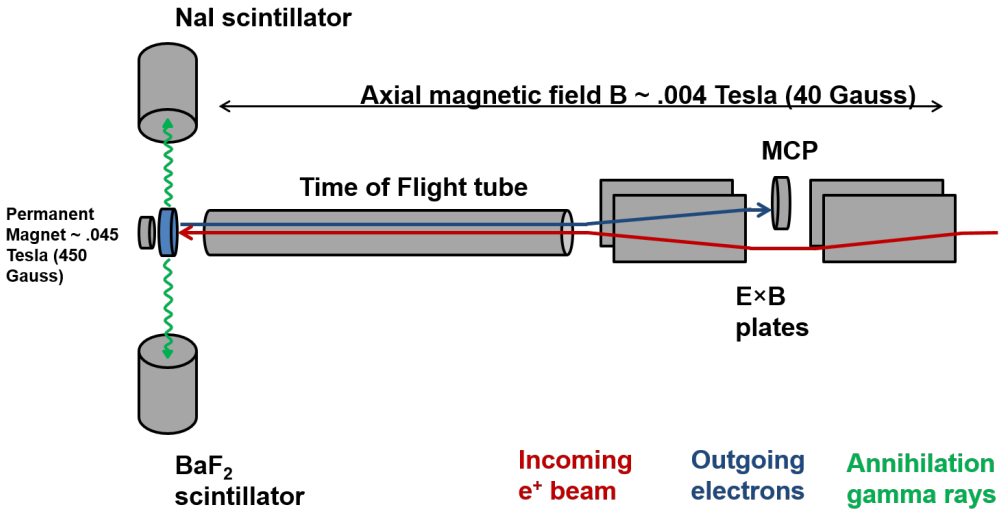

Figure 2.5: Schematic representation of the ToF spectrometer.

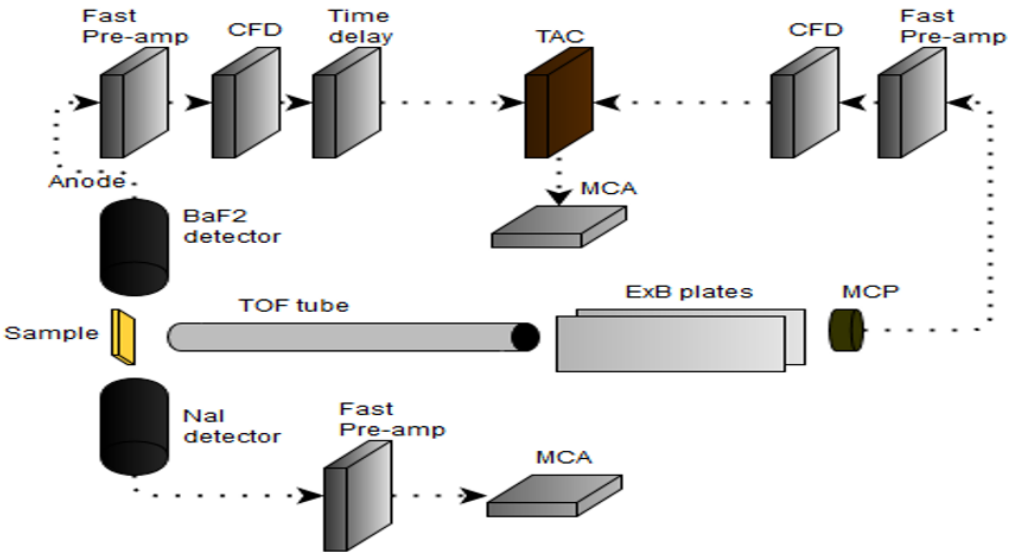

Figure 2.6: Schematic representation of the coincidence timing circuit.

2.6 Energy Conversion

The TOF spectra presented in this dissertation are converted to electron kinetic energy using an experimentally determined calibration function. The calibration function is determined experimentally by collecting representative secondary electron spectra at various sample biases. A series of positron-induced electron spectra are taken at selected sample biases, typically from -1 V to -900 V with ∼30 data points chosen in between. The low-energy (high ToF) edges of these spectra are taken to represent electrons that have escaped the sample with 0 eV. These 0 eV electrons are accelerated by the electric field due to the sample bias, V_{sample}, and travel the majority of their flight time as electrons with energy equal to eV_{sample}. The experimentally measured ToF of these eV_{sample} electrons is plotted versus $\frac{1}{\sqrt{eV_{sample}}}$, see fig. 2.7. The resulting data points are fit to a fifth order polynomial and this function, along with an appropriate Jacobian, is used to convert the ToF spectra to electron kinetic energy.

Suppose we have N(t) counts in each ToF bin t. We want to know how many counts N(E) in each energy bin E this would correspond to. Let's assume that the total number of measured electrons is conserved i.e.:

$$\int_{t_1}^{t_2} N(t)\ \mathrm{d}t = \int_{E_1}^{E_2} N(E)\ \mathrm{d}E \tag{2.4}$$

This can be rewritten as:

$$\int_{t_1}^{t_2} N(t)\ \frac{\mathrm{d}t(E)}{dE} dE = \int_{E_1}^{E_2} N(E)\ \mathrm{d}E \tag{2.5}$$

and hence we conclude:

$$N(E) = N(t(E)) \frac{\mathrm{d}t(E)}{dE} \tag{2.6}$$

Therefore, using our experimentally derived relationship between ToF and energy, we can determine the proper Jacobian to give us the number of counts per energy bin E.

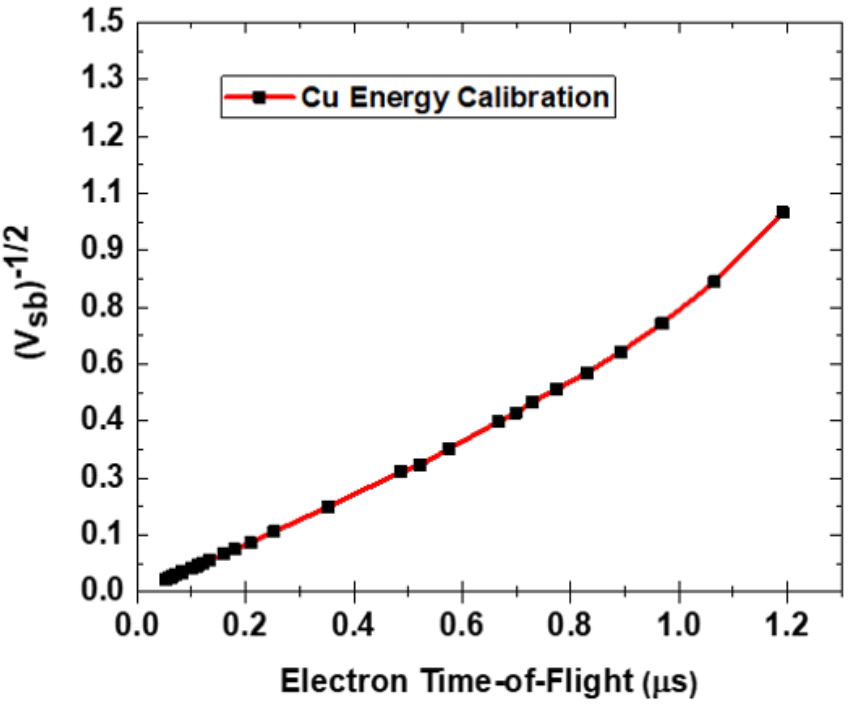

Figure 2.7: Energy calibration curve for Cu and the settings listed in table 2.2. The solid line through the points is a guide to the eye.

Chapter 3

3.1 Introduction

In this chapter, we report on the methods and results of numerical simulations of UTA's time-of-flight positron annihilation-induced Auger electron spectrometer (ToF-PAES). The ToF-PAES spectrometer is capable of transporting extremely low-energy positrons (< 1 eV) to the sample surface while simultaneously measuring the energy of outgoing electrons with energies from 0 eV to 500 eV. We have used SIMION® 8.1 to calculate the ToF spectra of electrons leaving the sample surface with energies and angles dispersed according to distribution functions chosen to model the positron-induced electron emission processes presented in this dissertation. Fig. 3.1 shows a SolidWorks drawing of the ToF-PAES spectrometer alongside the simulated spectrometer used in the SIMION simulations.

These numerical simulations have made possible quantitative estimates of the transport efficiency, the energy resolution, and the instrument response function of UTA's ToF-PAES spectrometer. For the set of low-energy transport settings presented here: (1) the simulations of the electron transport

through the ToF-PAES spectrometer indicate a nearly 100% transport efficiency to the electron detector for electron energies 1 to 200 eV, (2) the simulated relative energy resolution, $\frac{\Delta E}{E}$, is less than 25% over electron energies from 1 eV to 1000 eV, and (3) the instrumental contributions to the measured electron energy spectra predicted by these numerical simulations have made possible the detailed comparison of experimentally measured and theoretically generated spectra. In particular, they have made possible the direct comparison between measured and calculated line shapes for Auger-mediated positron sticking (AMPS) and positron annihilation-induced Auger electron emission (C VVV and O LVV). See chapters 4, 5, and 6 for the details of these calculations and comparisons for the O LVV, C VVV, and AMPS line shapes respectively.

Lastly, we have confidence in the results of our simulations due to the agreement between analytic expressions for the $\mathbf{E}\times\mathbf{B}$ drift distances and electron cyclotron radii, as well as our successful modelling of the experimental energy conversion curves. Ultimately, the accuracy of these simulations resides in our ability to accurately reproduce the experimentally measured line shapes using input distribution functions which are informed by the relevant physics to each process.

3.2 Simulation Details

We have performed numerical electron trajectory simulations utilizing the Monte Carlo type approach implemented within SIMION® 8.1. SIMION is a commercial 3D software package which obtains electrostatic fields as the

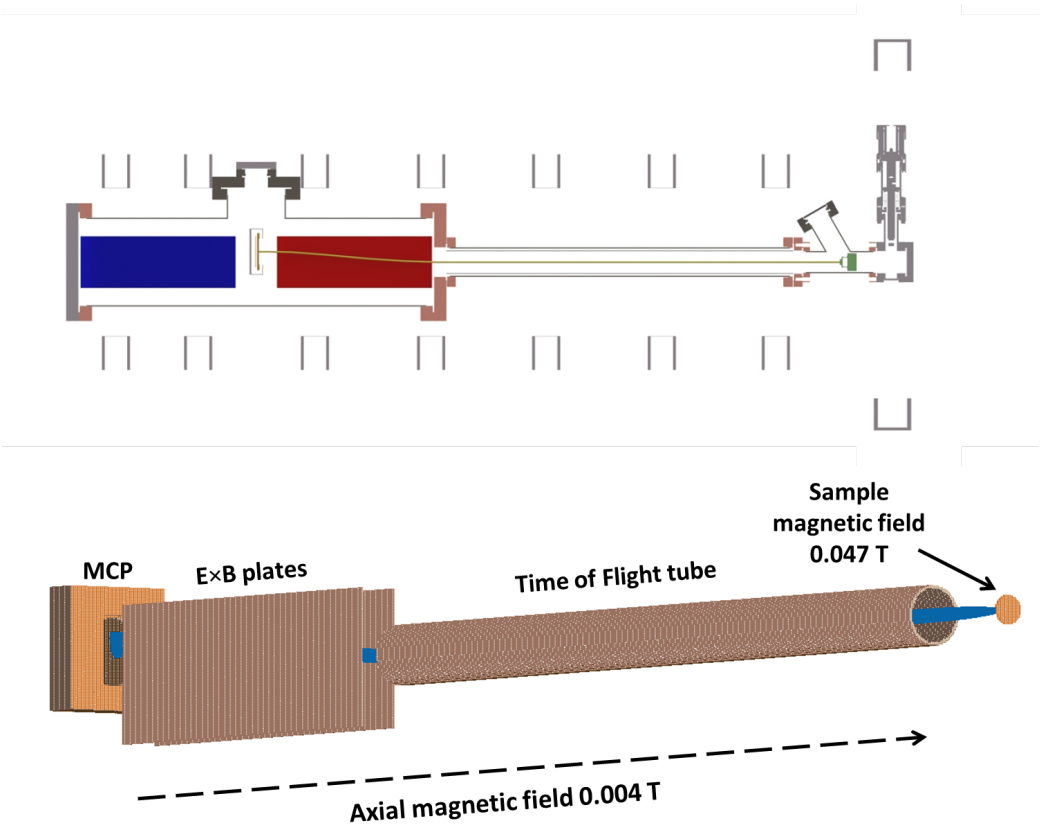

Figure 3.1: SolidWorks drawing and SIMION render of the time-of-flight positron annihilation-induced Auger electron spectrometer (ToF-PAES) at UT Arlington. The top panel is a SolidWorks drawing of the cross-sectional view of the spectrometer. The Helmholtz coils used to generate the transverse magnetic fields are represented in gray. The bottom panel is a render of the SIMION simulated spectrometer. The yellow (blue) lines in the top (bottom) panel represent the electron trajectories through the simulated spectrometer.

solutions to the Laplace equation using user-specified boundary conditions. SIMION solves the Laplace equation using a finite difference method called over-relaxation, in which a three-dimensional potential array (PA) of points represents the electrode geometry. Once the fields have been obtained, the charged particle trajectories are calculated using the Lorentz force law.

We have constructed our simulated spectrometer using SIMION's internally defined geometry functions with the parameters listed in table 3.1. The geometry script used to generate the simulated spectrometer geometry is provided in appx. A.I.. The simulated geometries consisted of: the grounded chamber walls, the sample, a 1 meter stainless steel tube (ToF tube), 2 sets of $\mathbf{E}\times\mathbf{B}$ plates, and the micro-channel plate (MCP) assembly housed in a grounded box. The magnetic fields were simulated using solenoids whose parameters were chosen to best match the measured magnetic field gradient of the experimental spectrometer determined using a Gauss meter. The Lua script used to define these solenoids is provided in appx. A.II.. The positron generation and transport portion of the ToF-PAES apparatus was not simulated.

The accuracy of the simulated electric and magnetic fields were checked by comparing the amount of $\mathbf{E}\times\mathbf{B}$ drift for mono-energetic electrons against an analytic expression derivable from energy conservation requirements. The analytic expression for the vertical drift an electron experiences between a set of $\mathbf{E}\times\mathbf{B}$ plates, y(x), is given by:

$$y(x) = \frac{\Delta V}{d}\frac{L}{B}\sqrt{\frac{m}{2(E - qV(x))}} \tag{3.1}$$

where ΔV is the potential difference between the plates, d is the distance

between the plates, L is the length of the plates, B is the magnitude of the magnetic field, m is the electron mass, q is the charge of the electron, E is the kinetic energy of the electron, and V(x) = $\frac{V_2 - V_1}{d}x + V_1$ is the potential the electron experiences at position x, assuming the origin y = x = 0 is placed at the bottom of the positive **E**×**B** plate V_1. Good agreement was found between the simulated results and equation 3.1 for all tested electron energies.

Measured Quantity	Value
Axial Magnetic Field	0.004 T
Sample Magnetic Field	0.047 T
East **E**×**B** Plate Voltage	-2.797 V
West **E**×**B** Plate Voltage	+3.193 V
E×**B** Plate Length	0.267 m
E×**B** Plate Height	0.089 m
E×**B** Plate Separation	0.025 m
MCP Box Thru Slot (W x H)	.02 m x .043 m
ToF Tube Length	0.597 m
Total Flight Distance	1 m

Table 3.1: Experimental values used in the SIMION simulations of the ToF-PAES spectrometer. These settings correspond to an incident positron beam energy with maximum cutoff ∼1 eV. The axial magnetic field points along the beam axis (south to north). All voltages are referenced to chamber ground.

The electron trajectory simulations were performed for single-valued ki-

netic energy distributions with uniformly randomized angular distributions. These electrons were generated uniformly on a circle of diameter 2.6 mm, which is the estimated positron beam spot size at the sample. The estimate of the positron beam spot size was obtained using the adiabatic invariance of the magnetic flux [16]:

$$\frac{r_m}{r_s} = (\frac{B_s}{B_m})^{1/2} \tag{3.2}$$

where $r_m(B_m)$ and $r_s(B_s)$ are the cyclotron radii(magnetic field) at the moderator and sample respectively. The ratio $\frac{B_s}{B_m}$ is $\sim$10, while r_m is given by the 8 mm aperture in the tungsten barrier just after the moderator [15].

Lastly, the experimentally determined energy calibration curves were successfully modelled for both the Cu and HOPG data sets giving excellent confidence in the accuracy of our simulated spectrometer. As it is necessary for the present discussion, we will briefly summarize the experimental calibration method detailed in chapter 2. A series of positron-induced electron spectra are taken at selected sample biases, typically from -1 V to -900 V with $\sim$30 data points chosen in between. The low-energy (high ToF) edges of these spectra are taken to represent electrons that have escaped the sample with 0 eV. These 0 eV electrons are accelerated by the electric field due to the sample bias, V_{sample}, and travel the majority of their flight time as electrons with energy equal to eV_{sample}. The experimentally measured ToF of these eV_{sample} electrons is plotted versus V_{sb}. These plots for Cu and HOPG are shown in fig. 3.2. The same procedure was adopted in the simulated case with one exception. Instead of fitting the low-energy edge of the simulated spectra to determine the time-of-flight-energy relationship we take directly

the ToF distribution of 0 eV energy electrons generated and associate the lowest of these ToFs to V_{sb}. Different reasonable choices of the representative 0 eV ToF, such as the peak of the distribution, do not significantly alter the results. The experimental and simulated results are compared in the left panels of fig. 3.2. The right panels of fig. 3.2 are the same as the left panels except that a rigid energy shift were applied to the simulated curve. Different rigid energy shifts were applied to the simulated curve to bring them into agreement the experimental Cu and HOPG curves.

The rigid energy shift can be attributed to the combination of two effects. First, the total rigid energy shift can be partly attributed to an off-axial center of the positron beam spatial distribution; and hence, an off-axial center of the outgoing electron spatial distribution. These off-axial trajectories effect the measured electron kinetic energy distributions in two ways: (1) the electrons will experience a slightly different magnetic field gradient and (2) the electrons will come slightly closer to one side of the $\mathbf{E}\times\mathbf{B}$ plates. Both of these will cause slight changes in the measured electron kinetic energies. Initial simulations of off-axial trajectories supports this hypothesis provided the deviation is not much more than 1 or 2 mm giving typical energy shifts of ≤ 0.5 eV.

Second, the total rigid energy shift can be partly attributed to the difference in work functions of the sample and analyzer (contact potential difference). This contact potential difference exists when two materials are brought into electrical contact, even indirectly through conductive wiring, causing electrons to flow from the material with a higher Fermi level into the material with a lower Fermi level until these two Fermi levels are equal [17]. While the Fermi

levels are equal, however, this does not mean that the electric potentials are equal. In fact, when the two material's Fermi levels are equilibrated, an electrostatic potential difference and electric field between sample and analyzer are established. This potential difference is also typically small, less than < 1 eV. Without measuring directly these contact potential differences or the positron beam spatial distributions, these two effects cannot be uncoupled easily.

The rigid energy shift for Cu was 1.22 eV. The rigid energy shift for HOPG was 0.85 eV. The rigidly shifted simulated calibration curves are displayed in the right panels of fig. 3.2. The sizes of these total rigid energy shifts are small and consistent with shifts expected to arise from the combined effects of an off-axis incident positron beam and contact potential differences.

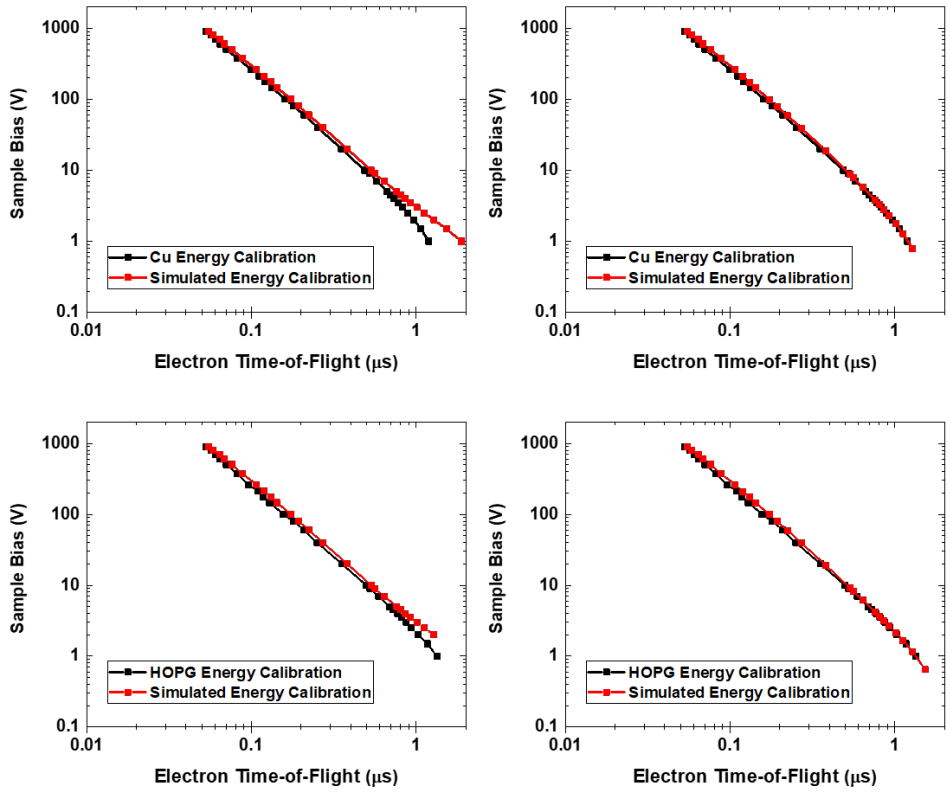

Figure 3.2: Comparison between simulated and experimentally determined energy calibration curves for Cu and HOPG. The left panels show the experimental and simulated calibration curve. The simulated calibration curve is the same in both left panels. The right panels are the same curves as in the left panels except that the simulated curve has been rigidly shifted in the energy. Different rigid energy shifts were applied to the simulated curve to bring them into agreement with the experimental Cu and HOPG curves. The agreement, with only a constant shift, provides support that the modelling of the ToF-PAES spectrometer has been successful. The solid lines through the points are a guide to the eye.

3.3 Transport Efficiency

We have estimated the transport efficiency of the ToF-PAES spectrometer has using single-valued electron energy trajectory simulations. The transport efficiency is defined as the number of electrons that reached the simulated detector divided by the number of electrons generated and was recorded as a function of the initial electron kinetic energies at the sample. 5000 electrons per single-valued energy were flown with uniformly randomized (isotropic) angular distributions for each sample bias simulated. We note that reducing the number of simulated particle trajectories per single-valued energy was not found to significantly influence the transport efficiency results and that a small representative number of electron energies was sufficient to determine the overall shape.

Fig. 3.3 shows the simulated transport efficiency as a function of the initial electron kinetic energy at the sample. The simulations indicate that for all sample biases relevant to this dissertation, there is a wide-range of initial electron kinetic energies (1 eV to 200 eV) that show a transport efficiency of $\sim$100%. For sample biases $\leq$ -1.0 V, the reduction in the transport efficiency of electron trajectories initiated with kinetic energies less than 1 eV is due to either reflection off the $\mathbf{E}\times\mathbf{B}$ plates or termination at the top of the MCP box due to too much vertical drift while in the $\mathbf{E}\times\mathbf{B}$ field. Both of these effects are due to the small kinetic energies these electrons have relative to the $\mathbf{E}\times\mathbf{B}$ voltages. For all sample biases, the reduction in the transport efficiency of electron trajectories initiated with kinetic energies $>$ 200 eV is due to either termination at the $\mathbf{E}\times\mathbf{B}$ plates or termination at the bottom of the MCP box due to too little vertical drift while in the $\mathbf{E}\times\mathbf{B}$ field. Both of these

effects are due to the large kinetic energies these electrons have relative to the **E**×**B** voltages. The termination at the **E**×**B** plates happens because these high-energy electrons have Larmor radii that are comparable to the **E**×**B** spacing. In SI units, the Larmor radius, r_g, is given by:

$$r_g = \frac{mv}{qB} \tag{3.3}$$

where m is the mass of the electron, v is the velocity of the electron, q is the charge of the electron, and B is the strength of the magnetic field. For a 500 eV electron (which corresponds to a velocity of $1.33 \times 10^7 \ \frac{m}{s}$) in a magnetic field of 0.004 T, the Larmor radius is ∼0.019 m. This is comparable to the **E**×**B** spacing of 0.025 m.

Finally, the -0.5 V simulated transport efficiency data was fit to an analytic function. This fitting function was used in chapters 4, 5, 6 in the modelling of the experimental intensities. The fitting function used was:

$$\eta(E) = 0.01 \cdot (A_2 + \frac{A_1 - A_2}{1 + (\frac{E}{E_0})^p}) + c \cdot \exp(-\frac{E}{d}) + e \cdot \exp(-\frac{E}{f}) + g \cdot x^2 \tag{3.4}$$

where E is the kinetic energy of the electron at the sample and the remaining coefficients are all fitting parameters. The list of fitting parameters used to parameterize the simulated transport efficiency in this dissertation is listed in table 3.2. The first three terms are the most important in getting the overall shape of the transport efficiency curve. The degree of the polynomial term can be varied to obtain fits to the various sample bias curves and transport settings provided they are not too dissimilar to those presented in table 3.1.

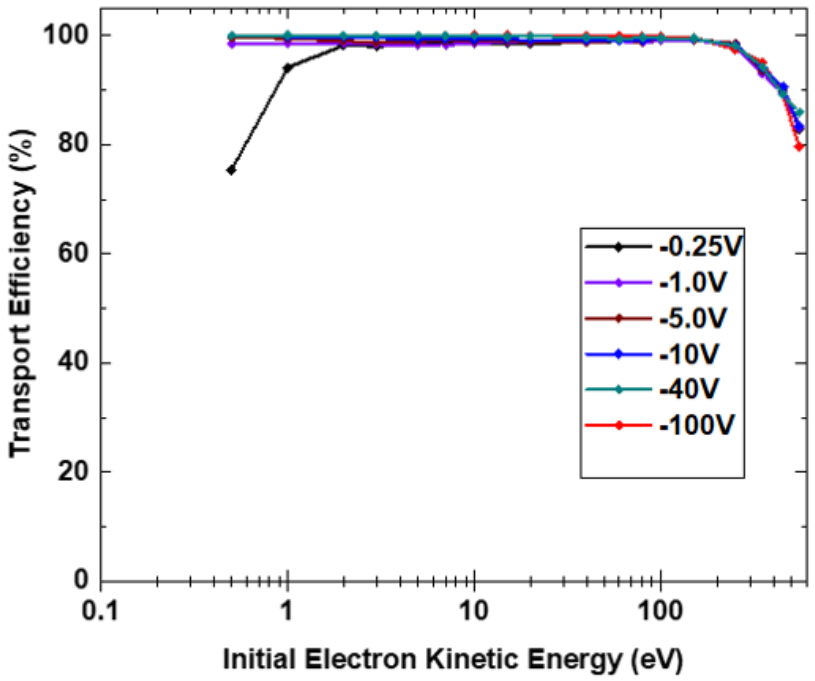

Figure 3.3: Simulated electron transport efficiency as a function of the initial electron kinetic energy for various sample biases. The legend indicates the negative bias applied to the sample. A wide-range of electron energies, between 1 eV and 200 eV, travel through the spectrometer with nearly ∼100% transport efficiency. The solid lines through the points are a guide to the eye.

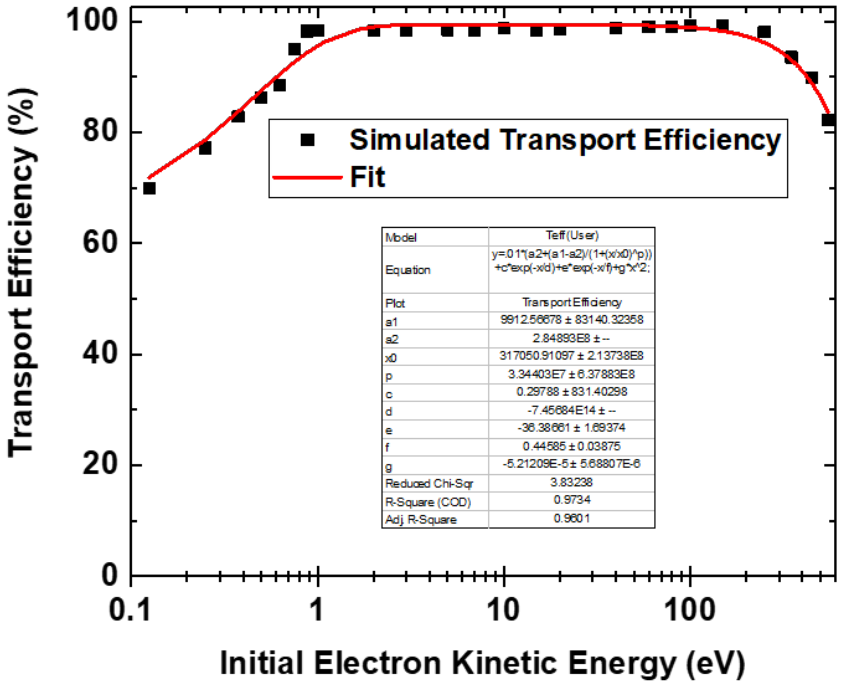

Figure 3.4: Fit to the -0.5 V simulated electron transport efficiency data using equation 3.4. This fitting function was used in chapters 4, 5, 6 in the modelling of the experimental intensities.

Fitting Parameter	Value
A_1	9912.56678
A_2	$2.848\,93 \times 10^{8}$
E_0	317050.91097
p	$3.344\,03 \times 10^{7}$
c	0.29788
d	$-7.456\,84 \times 10^{14}$
e	-36.38661
f	0.44585
g	$-5.212\,09 \times 10^{-5}$

Table 3.2: Fitting parameters obtained from fitting equation 3.4 to the -0.5 V simulated transport efficiency data.

3.4 Energy Resolution

The uncertainty in the measurement of the electron kinetic energy distribution by the ToF-PAES spectrometer is determined by: (1) the angular divergence of the electron momentum entering the ToF analyzer, (2) the uncertainty in the determination of the ToF (timing resolution) of the spectrometer, and (3) the influence of any electric fields along the flight path of the electrons. In order to minimize the angular divergence of the electrons entering the ToF analyzer, a permanent magnet mounted behind the sample is used to create a magnetic field gradient that parallelizes the outgoing electron momentum along the beam axis. The relative uncertainty in measuring the electron kinetic energy due to the angular divergence of the emitted electrons at the ToF analyzer is given by:

$$(\frac{\Delta E}{E})_{angular\ \ divergence} = \frac{B_a}{B_s} \tag{3.5}$$

where B_a refers to the magnetic field strength at the ToF analyzer and B_s refers to the magnetic field strength at the sample. Equation 3.5 arises from energy conservation requirements and the adiabatic invariance of the magnetic moment $\mu = \frac{mv_{\perp}^2}{2B}$ [18]. For the experiments presented in this dissertation, $\frac{B_a}{B_s} \approx \frac{1}{10}$. It is important not to mistake the uncertainty associated with the angular divergence of the emitted electrons as due to a variance in the amount of time electrons with various energies or angles take to parallelize. This is not the case since the parallization time is negligible compared to the total flight time.

Since the electrons spend the majority of their flight time in the relatively field-free ToF tube we can approximately treat the electron kinetic energy measured by the ToF spectrometer as $E = \frac{1}{2}m\frac{L^2}{t^2}$, where L is the length of the electron flight path and t is the measured ToF. Differentiating and rearranging this equation yields:

$$(\frac{\Delta E}{E})_{time\ uncertainty} = \frac{2\Delta t}{t} \tag{3.6}$$

where Δt is the timing resolution of the ToF-PAES spectrometer and involves the timing resolution of the MCP electron detector, the timing resolution of the gamma detector, and the timing resolution of the associated timing electronics and timing algorithms. Assuming that the timing resolution and uncertainty due to the angular divergence are uncorrelated, we can express them in total as the summation in quadrature of the individual errors:

$$\frac{\Delta E}{E} = \sqrt{(\frac{2\Delta t}{t})^2 + (\frac{B_a}{B_s})^2} \tag{3.7}$$

Finally, an additional source of uncertainty in the measurement of the electron kinetic energy is the influence of electric fields along the flight path of the electrons, in particular the $\mathbf{E}\times\mathbf{B}$ regions. The amount of time electrons spend in the $\mathbf{E}\times\mathbf{B}$ region can be an appreciable fraction of the total ToF and is particularly important for low-energy electrons. For example, a 1 eV electron with a -1 V sample bias that travels perfectly axial with no angular divergence will spend more than $\frac{1}{4}$ of its total ToF in the $\mathbf{E}\times\mathbf{B}$ region before entering the ToF tube.

We have used numerical electron trajectory simulations in order to estimate the energy resolution of the ToF-PAES spectrometer taking into account

the the combined effects of all three broadening mechanisms. The timing resolution was determined by convolving a simulated secondary electron spectra with Gaussians of various FWHMs until a best fit with the experimental -900 V secondary electron spectra was found. The secondary electron distribution, N(E), used in simulating the experimental -900 V spectrum was taken from the literature describing secondary electron distributions and is given by:

$$N(E) = A\,\frac{E}{E+E_0}\,(E+\phi)^m \tag{3.8}$$

where $E_0 = 0.35\ eV$, $\phi = 4.6\ eV$, and m = -2.5 [19, 20]. We choose a large sample bias, and hence large secondary electron energy, because the uncertainty due to the angular divergence will be negligible compared to the timing uncertainty. The reasons for this are that the applied negative bias results in electron emission with larger parallel velocity components and that positron-induced secondary electrons can be emitted from a few atomic layers below the surface meaning their angular distributions are less isotropic [21].

To determine the energy resolution as a function of the electron kinetic energy at the ToF tube, 500 electrons per single-valued electron energy were flown with uniformly randomized (isotropic) angular distributions for each sample bias simulated. We note that increasing the number of simulated particle trajectories per single-valued energy was not found to significantly influence the energy resolution results. The ToF of the electrons reaching the simulated MCP was recorded internally to SIMION and used to generate a ToF histogram with bin width equal to the experimental spectrum of $\sim$2 ns per bin. For every initial single-valued electron kinetic energy, a ToF histogram was constructed. The resulting simulated ToF spectra was convoluted with a Gaussian with FWHM of 2.35 ns in order to take into account the timing

uncertainty of the detectors and electronics. The simulated ToF spectra were converted into energy using a fit to the simulated calibration curve from fig. 3.2 along with an appropriate Jacobian, see chapter 2. The energy resolution was determined by fitting each energy-converted ToF spectrum to a Gaussian function whose FWHM was taken as the energy resolution. Fig. 3.5 shows the simulated energy resolution as a function of the electron kinetic energy at the ToF tube for several sample biases. The simulated relative energy resolution is less than 25% for electron energies from 1 to 1000 eV.

Fig. 3.6 is a comparison between our simulated results for 60 eV electrons with the analytical expression given in ref. [21] for 59 eV electrons. Both results are for -5 V on the sample. The additional width associated with our simulated results is due to the differences in $\frac{B_a}{B_s}$ ratios ($\frac{1}{10}$ versus $\frac{1}{13}$) and the inclusion of additional broadening effects. Despite these differences we can see the overall shape is similar and gives confidence to the accuracy of our simulated results. Additionally, we can draw some basic conclusions about the effect the spectrometer has on the measured electron kinetic energy distribution. The spectra do not peak at initial electron kinetic energy of 60 eV, but are shifted to lower electron kinetic energies by 3 or 4 eV. They are sharper on their low-energy side and most of the broadening is towards the high-energy side after the peak of the distribution.

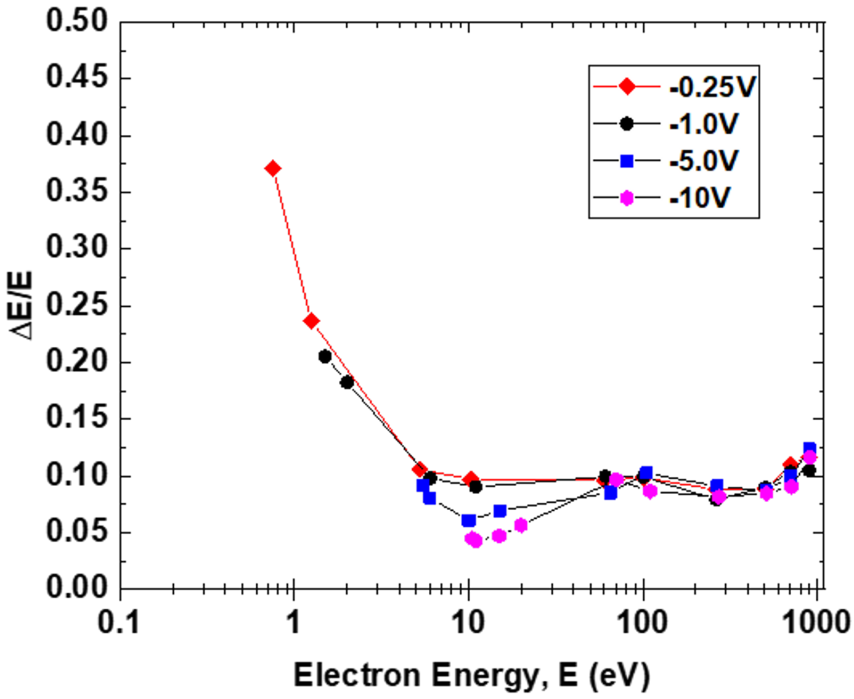

Figure 3.5: Simulated relative energy resolution as a function of the electron kinetic energy at the entrance of the ToF tube for various sample biases. The simulated relative energy resolution is less than 25% for electron energies from 1 to 1000 eV. The solid lines through the points are a guide to the eye.

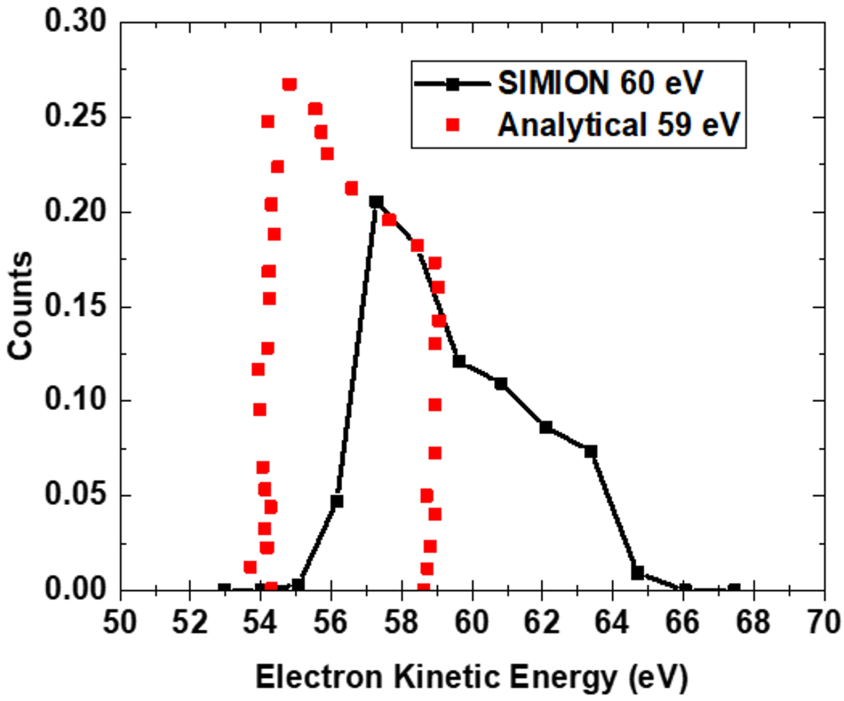

Figure 3.6: Comparison between simulated and analytical electron kinetic energy distributions for - 5 V sample bias. Data digitized from ref. [21]. The lack of sharpness of the low-energy and high-energy edges for the analytic results is due to digitization errors. The solid line through the points is a guide to the eye.

3.5 Instrument Response Function

The measured positron-induced electron kinetic energy distributions are artificially broadened due to instrumental effects. The sources of this instrumental broadening have been discussed above and are: (1) the angular divergence of the electron momentum entering the ToF analyzer, (2) the uncertainty in the determination of the ToF (timing resolution) of the spectrometer, and (3) the influence of any electric fields along the flight path of the electrons. Due to the large range of energies and angles, 0 eV to 1000 eV and $\sim$2 π solid angle, the ToF spectrometer accepts it is not possible to associate with each ToF one unique initial electron kinetic energy. This makes correction of the measured electron spectrum due to instrumental effects impossible. Therefore, in order to quantify the instrumental broadening present in our measured spectra, we have generated theoretical electron energy distributions, which are informed by the relevant physics, and simulated their corresponding electron trajectories using SIMION. SIMION has been successfully used previously in the modelling of instrument response functions of electron spectrometers including time-of-flight systems [22, 23, 24].

If we take the measurement of the electron ToF using the ToF-PAES spectrometer as a linear time-invariant system, then the resulting output signal Y(T) is given as the convolution of the input signal X(T) and the system's impulse response function h(T):

$$Y(T) = (X * h)(T) = \int_{-\infty}^{\infty} X(T-\tau) \cdot h(\tau) \mathrm{d}\tau \tag{3.9}$$

where h(T) is the system's response to an impulse $X(T) = \delta(T)$. For our system the output signal is the measured ToF and the input signal is the

initial electron kinetic energy distribution. Then, h(T) is the ToF spectrum corresponding to a single-valued (delta function) electron energy distribution input. The principal of superposition (linearity) means that any complicated input can be generated from unit impulses with different amplitudes. Therefore, the instrumental response to any theoretically generated electron kinetic energy distribution can be found from appropriately weighting the instrument response to a uniform distribution of single-valued electron energy trajectory simulations.

In order to estimate our system's impulse response function, we ran electron trajectory simulations for 500 electrons per single-valued electron energy with uniformly randomized (isotropic) angular distributions in energy steps from 0 eV up to an appropriate endpoint energy and for multiple sample biases. For simulating the low-energy Auger processes (O LVV and C VVV), an endpoint energy of 15 eV with 121 energy bins was selected (60,500 particles flown). For simulating the AMPS processes, an endpoint energy of the sample bias and 101 energy bins was selected (50,500). The ToF of the electrons that reached the simulated MCP were recorded internally to SIMION and used to generate a ToF histogram with bin width equal to the experimental spectrum of $\sim$2 ns per bin. These single-valued energy, ToF spectra were indexed by their initial kinetic energy at the sample and were weighted by theoretical electron energy distributions in accordance with the principal of superposition. The resulting ToF spectrum of these theoretical distributions were convoluted with a Gaussian with FWHM of 2.35 ns in order to take into account the timing uncertainty of the detectors and electronics before being compared to experimental spectrum in both the ToF and energy

space. The weighting was done using an offline analysis algorithm:

$$S(t) = \frac{1}{N} \sum_{E} S_E^{BOX}(t) \cdot S(E) \tag{3.10}$$

where S(t) is the ToF spectrum corresponding to the initial theoretical electron energy distribution S(E), N is the number of particles flown for the single-valued electron energy trajectory simulations, and $S_E^{Box}(t)$ is the ToF spectra indexed by their single-valued incident electron energies. The use of this offline algorithm necessitates only one simulation per sample bias and saves considerable computational time in comparison to programming the theoretical positron-induced electron spectra directly into SIMION. A small, but crucial, technical detail is that the energy bin sizes between the simulations and the theoretical electron spectrum must be the same. Typically, the theoretical electron spectrum is generated in a very small step size for high accuracy and simply interpolated to the generally larger bin size of the simulation. The code that performs all these steps is included in appx. A.IV..

A comparison between several theoretical initial electron kinetic energy distributions and their instrumentally-broadened and energy-converted outputs are presented in fig. 3.7. In each panel the black spectrum is the initial theoretical electron energy distribution and the red spectrum is the resulting energy-converted, ToF spectrum after instrument response and subtracting the sample bias. Panel (a) shows the instrument response function to the calculated TiO_2 O LVV Auger electron spectrum, discussed in chap. 4, for a sample bias of -0.5 V. There is a slight broadening of the high-energy edge by $\sim$1 eV, as well as a loss in counts at electron energies $<$1 eV due to the transport efficiency, see fig. 3.3. The overall shape of the spectrum is

retained with no shifting of the peak. Panel (b) shows the instrument response function to the calculated SLG C VVV Auger electron spectrum, discussed in chap. 5, for a sample bias of -0.25 V. Like the TiO_2 spectrum there is minor broadening of the high-energy edge and a loss in counts at electron energies $<$1 eV. Additional broadening of the second prominent spectral feature at $\sim$4 eV is also present. Again, the overall shape remains in tact and there is no shift of the peak intensities. Panel (c) and panel (d) show the instrument response function to the calculated HOPG (Si) AMPS spectra, discussed in chap. 6, for a sample bias of -2.5 V (-3.0 V). Since these AMPS electrons are of much lower energies the instrumental effects on the theoretical spectra are much more dramatic. There is significant broadening of the high-energy edges and shifting of the peaks due to the transport losses below 1 eV. However, we can see from panel (d) that the double peak structure in the Si AMPS is preserved. The relative heights of the two peaks are distorted due to the transport losses below 1 eV and the significant broadening of the high-energy makes the second peak appear more as a shoulder but each feature is still discernible with some degree of separation. This demonstrates that even at these very low electron energies, spectral features which are representative of the electronic structure of the sample are still preserved despite the effects of the instrument response function.

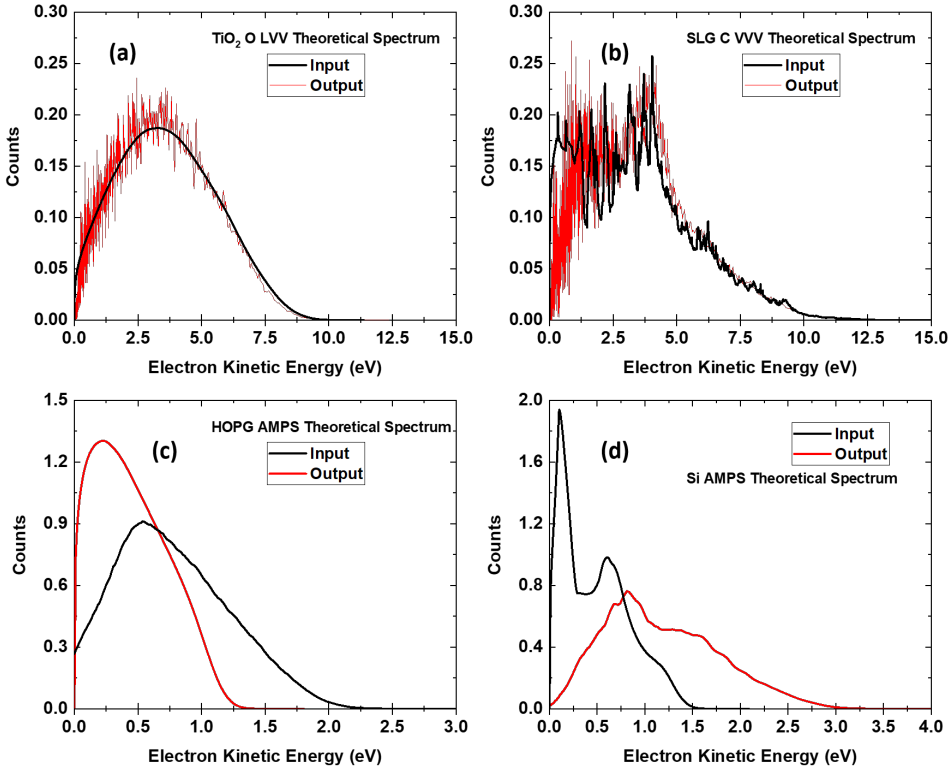

Figure 3.7: Calculated positron-induced electron kinetic energy distributions before and after experiencing instrumental effects. Panel (a) is the instrument response to the calculated TiO_2 O LVV Auger electron spectrum for a sample bias of -0.5 V. Panel (b) is the instrument response to the calculated SLG C VVV Auger electron spectrum for a sample bias of -0.25 V. Panel (c) and panel (d) are the instrument responses to the calculated HOPG (Si) AMPS spectrum for a sample bias of -2.5 V (-3.0 V). The instrumental effects are not as important for the Auger spectra but are considerably important for accurate modelling of the AMPS spectra.

3.6 Concluding Remarks

In this chapter, we have presented the methods and results of numerical simulations of UTA's time-of-flight positron annihilation-induced Auger electron spectrometer (ToF-PAES). The system has been characterized including its transport efficiency, timing and energy resolution, and instrument response function. We have investigated each of these quantities in terms of the electric field near the sample due to the sample bias. For the set of low-energy transport settings presented here, and for small variations from these settings, the following conclusions can be drawn:

(1) The simulations of the electron transport through the ToF-PAES spectrometer indicate a nearly 100% transport efficiency to the electron detector for electron energies 1 to 200 eV. The reduction in the transport efficiency of electron trajectories initiated with kinetic energies less than 1 eV is due to either reflection off the $\mathbf{E}\times\mathbf{B}$ plates or termination at the top of the MCP box due to too much vertical drift while in the $\mathbf{E}\times\mathbf{B}$ field. The reduction in the transport efficiency of electron trajectories initiated with kinetic energies > 200 eV is due to either termination at the $\mathbf{E}\times\mathbf{B}$ plates or termination at the bottom of the MCP box due to too little vertical drift while in the $\mathbf{E}\times\mathbf{B}$ field.

(2) The simulated relative energy resolution is less than 25% for electron energies from 1 to 1000 eV. The timing resolution was found to be 2.35 ns. The effects of the electric fields from the sample and $\mathbf{E}\times\mathbf{B}$ are important to consider in addition to the angular divergence of electrons entering the ToF tube and the timing resolution of the spectrometer.

(3) The instrumental contributions to the measured electron energy spectra predicted by these numerical simulations have made possible the detailed comparison of experimentally measured and theoretically generated spectra. In particular, they have made possible the direct comparison between measured and calculated line shapes for Auger-mediated positron sticking (AMPS) and positron annihilation-induced Auger electron emission (C VVV and O LVV). The most prominent effects of the instrument response function are to broaden the high-energy edges and to shift peaks in the electron spectrum below 1 eV due to transport losses. These effects are barely discernible in the Auger spectra, but are essential for the accurate modelling of the AMPS spectra. We have demonstrated that even at these very low electron energies, spectral features which are representative of the electronic structure of the sample are still preserved despite the effects of the instrument response function. Lastly, we note that the offline algorithm developed for applying the instrument response function to a theoretically generated positron-induced electron spectra necessitates only one simulation per sample bias saving considerable computational time.

Chapter 4

4.1 Introduction

In this chapter, we present direct evidence of a hitherto unexplored O LVV Auger transition occurring at oxygen-exposed Cu and Si surfaces and a TiO_2 surface. There has neither been a definitive experimental observation nor any quantitative analysis of this O LVV Auger transition in oxide surfaces previously [25, 26, 27]. In order to eliminate the secondary electron background —which has made previous definitive identification and quantitative investigation of this Auger transition impossible —we have utilized positrons with kinetic energies <1.5 eV to initiate the Auger process via positron-electron annihilation [28, 7]. The lack of previous work, and the notable omission of the O LVV Auger transition from standard Auger handbooks [29], illustrates the difficulty that conventional Auger techniques have in studying this increasingly important Auger electron energy range of 0 to 10 eV.

The O LVV Auger emission process is initiated when a surface trapped positron annihilates with an O 2s electron. The resulting hole is subsequently filled by a valence electron, causing a third electron in the valence band to be

emitted into the vacuum. This process is schematically represented in Fig. 4.1 for the calculated TiO_2(110) density of states [30]. An added advantage of using positron annihilation to initiate the Auger process is the selectivity to the top-most atomic layer due to the trapping of the positrons at the image potential-induced well on the vacuum side of the sample surface [12]. The wave function of the surface trapped positron rapidly decays and has appreciable overlap solely with electrons of the surface terminating atomic species. Thus, the majority of the annihilation-induced holes and the resulting Auger electrons originate almost entirely from the top-most atomic layer.

We have measured the kinetic energies of electrons emitted following O LVV Auger transitions for three surfaces: Cu, Si, and TiO_2. Each sample was sputter cleaned and exposed to O_2 prior to measurements. Our experimental and theoretical work demonstrate that most of the spectral weight in these positron annihilation-induced Auger electron spectra, in the energy range of 0-10 eV, is associated with the presence of oxygen on the surfaces and provides compelling, direct evidence that the O LVV Auger electron emission process is highly efficient. The O LVV Auger line shape of TiO_2 is accounted for in terms of the self-convolution of the density of states (DOS) while the number of detected O LVV Auger electrons enables an estimate of the probability that a positron will annihilate with an O 2s electron. The agreement between our experimental and theoretical work indicates that low-energy electron emission following the Auger decay of O 2s holes is nearly as efficient as electron emission following the Auger decay of O 1s holes in TiO_2.

This observation of a novel, highly efficient decay channel in metal oxide systems which leads to a multi-hole final state has important implications for

the understanding of ion desorption [31], Coulombic decay [32], photodynamic cancer therapies [33], and may yield important insights into the reactive sites for corrosion and catalysis [34, 35].

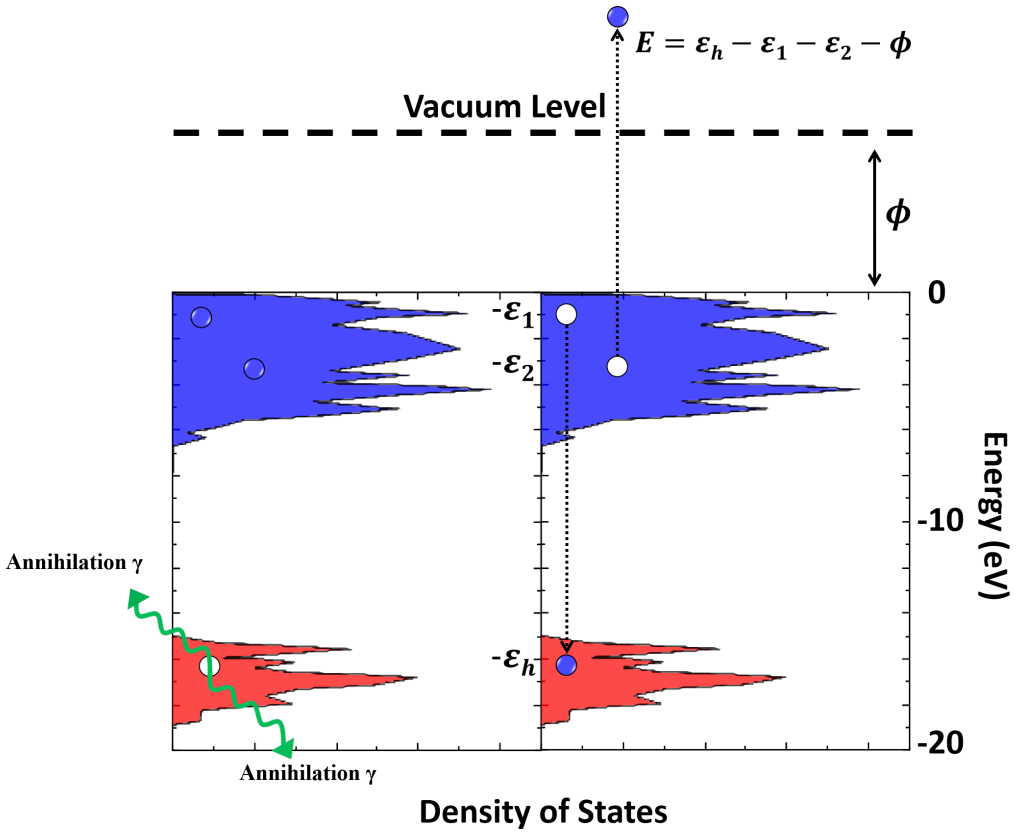

Figure 4.1: Schematic representation of an annihilation-induced O LVV Auger emission process. A surface trapped positron annihilates with an O 2s electron (red) with binding energy ε_h. An Auger transition occurs in which a valence band electron (blue), with binding energy ε_1, comes to occupy the energy level of the initial core hole. The energy associated with this transition is then coupled to another valence electron in the solid with binding energy ε_2, which is emitted into the vacuum with kinetic energy $E = \varepsilon_h - \varepsilon_1 - \varepsilon_2 - \phi$, where ϕ is the energy required to remove an electron from the solid. The density of states, $\rho(\varepsilon)$, shown is for a TiO_2(110) surface [30].

4.2 Experimental Details

The experiments presented in this chapter were performed using the University of Texas at Arlington's positron beam system described in chapter 2. The sample chamber is kept at a base pressure less than 10^{-8} Pa. The incident positron beam energy was measured to be less than 1.5 eV using a retarding field analyzer. The polycrystalline Cu and Si(100) samples were sputter cleaned every 24 hours before exposure to 1.8×10^3 and 2.7×10^5 Langmuir of O_2 respectively. A rutile TiO_2(110) sample, purchased from Sigma-Aldrich, was sputter cleaned then annealed at 875 Kelvin in an O_2 environment of 1×10^{-3} Pa for 30 minutes prior to measurements. Each spectrum has been divided by a number proportional to the number of positrons annihilating at the sample as determined using a NaI(Tl) detector mounted near the sample. The Cu and Si ToF's were measured using the BaF_2 detector while TiO_2 data used the NaI(Tl) detector. Therefore, the timing resolution is slightly worse for the TiO_2 spectra, although this effect was not important for the results in this chapter.

4.3 Experimental Results

The time-of-flight positron annihilation-induced Auger electron spectra (ToF-PAES) for Cu, Si, and TiO_2 are presented in Fig. 4.2. The initial measurements of the sputter cleaned Cu surface (top-left panel) exhibit peaks due to the Auger decay of annihilation-induced 3s holes in Cu (M_1VV) and 3p holes in Cu ($M_{2,3}VV$), labelled (a) and (b) in the panel respectively. The initial measurements of the sputter cleaned Si surface (top-right panel) exhibit peaks due to the Auger decay of annihilation-induced 2p holes in Si ($L_{2,3}VV$), labelled (c) in the panel. The TiO_2 spectrum (bottom panel) exhibits peaks due to the Auger decay of annihilation-induced 3p holes in Ti ($M_{2,3}VV$) and 1s holes in O (KVV). After exposing the Cu (top-left panel) and Si (top-right panel) surfaces to O_2 gas, an increase in the integrated PAES intensity below 10 eV is seen alongside the appearance of the O KVV Auger peak.

The increased low-energy intensity for oxygen on Cu and Si, and the broad, low-energy peak in TiO_2 are each associated with the presence of oxygen on the surface, as indicated by the emergence of the O KVV Auger peaks. The decreases in the Cu $M_{2,3}VV$ and Si $L_{2,3}VV$ Auger integrated intensities are consistent with previous measurements of O_2 exposed Cu and Si surfaces. These previous experimental and theoretical investigations successfully accounted for the decreased Cu $M_{2,3}VV$ and Si $L_{2,3}VV$ integrated intensities in terms of the oxygen-induced displacement of the positron wave function away from the Cu and Si atoms of the surface [36, 37, 38, 39, 40]. In the TiO_2, the small Ti $M_{2,3}VV$ Auger signal, relative to the two oxygen-derived Auger signals, is consistent with previous findings that the positron wave function overlap is primarily with the surface oxygen atoms [41, 42].

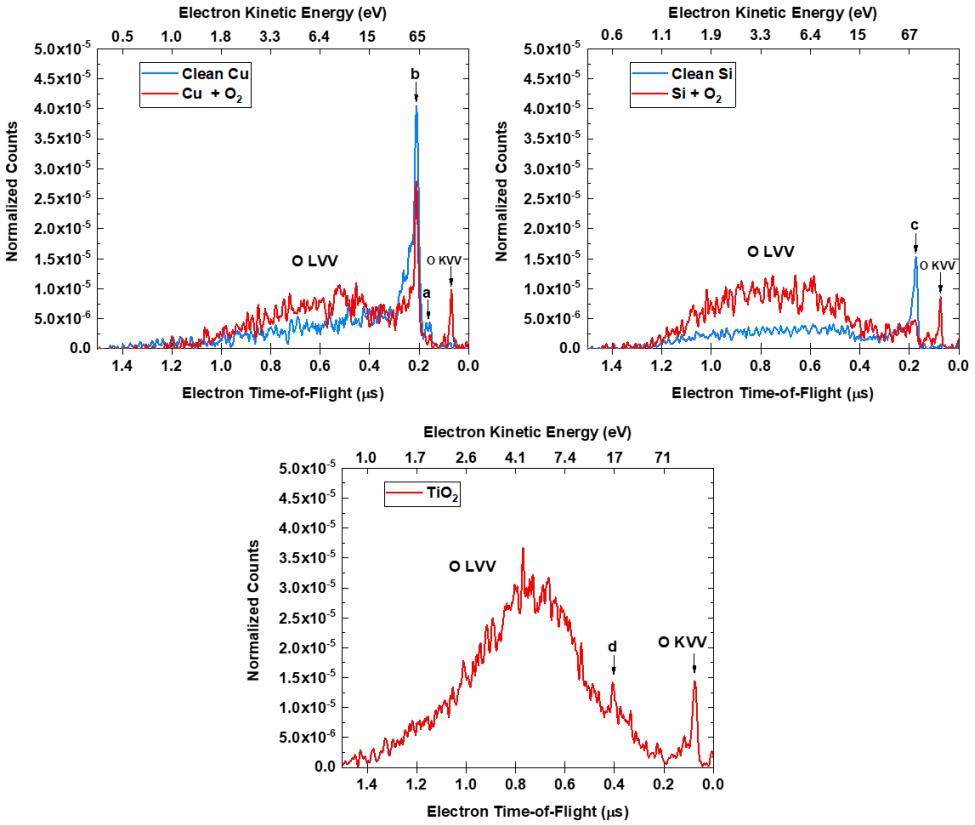

Figure 4.2: Measured ToF-PAES of Cu, Si, and TiO_2. ToF spectra of electrons emitted following the Auger decay of positron annihilation-induced holes. The bottom axis is the time the electrons take to travel 1 m. The top axis is the corresponding kinetic energy calculated from the ToFs. The top-left panel compares the clean Cu spectrum (blue) and the oxygen-exposed Cu spectrum (red). The top-right panel compares the clean Si spectrum (blue) and the oxygen-exposed Si spectrum (red). The bottom-panel is the ToF-PAES from TiO_2. The low-energy peaks labeled O LVV in each spectrum are primarily due to electron emission resulting from the Auger decay of O 2s levels with some contributions from Auger emission from the metal atoms.

An analysis of the integrated PAES intensities shows that the change in the low-energy intensity is 4 times the change in the Cu $M_{2,3}VV$ and 18 times the change in the Si $L_{2,3}VV$. This increased intensity cannot be explained by competing processes such as inelastic scattering of outgoing Auger electrons [43, 44], and is evidence for Auger electron emission following an LVV transition in oxygen adsorbed on Cu and Si surfaces. Additionally, since the incident positron beam energy has a maximum kinetic energy cutoff of 1.5 eV, the only electron emission mechanisms that are energetically possible are Auger emission processes. Secondary electron emission processes are energetically forbidden at these incident positron beam energies.

The ToF-PAES spectra presented in fig. 4.2 have been corrected for contributions to the low-energy intensity associated with the metal-derived Auger transitions (Cu $M_{2,3}VV$, Si $L_{2,3}VV$, and Ti $M_{2,3}VV$). These corrected spectra are presented in figs. 4.3 and 4.4. We have used the clean Cu and clean Si data to model the low-energy intensity associated with the Cu $M_{2,3}VV$ and Si $L_{2,3}VV$ Auger peaks in the O_2 exposed data. For the Cu spectra, we have normalized the integrated intensity of the Cu $M_{2,3}VV$ Auger peak of the oxygen-exposed spectrum to the integrated intensity of the clean Cu spectrum before subtracting the clean spectrum from the oxygen-exposed spectrum. The same procedure has been adopted in the case of the Si data with the Si $L_{2,3}VV$ peak. The two assumptions behind this procedure is that the low-energy intensity is proportional to the area of the metal-derived Auger peak intensities and that ratio of the low-energy intensity to the metal-derived Auger peaks does not change substantially.

For the TiO_2 data, where we do not have an associated clean metal

spectrum to use as a model, we have estimated the background due to inelastically scattered Ti $M_{2,3}$VV Auger electrons using the product of a Shirley background and the electron escape function, P_e(E). The electron escape function will be discussed in more detail in the following section. The estimated background is shown in fig. 4.5. The background, S(E), was calculated according to:

$$S(E) = P_e(E) \cdot \left(I_2 + (I_1 - I_2) \cdot \frac{A_2(E)}{A_1(E) + A_2(E)} \right) \tag{4.1}$$

where I_1 is the intensity at an energy suitably below the Auger peak, I_2 is the intensity at an energy suitably above the Auger peak, $A_1(E)$ is the area between I_1 and E, and A_2(E) is the area between E and I_2. The values chosen for this work were $I_1 = 13$ and $I_2 = 30$ which is consistent with previous measurements of the width of the Ti $M_{2,3}$VV peak measured by Auger-photoelectron coincidence spectroscopy (APECS) [45].

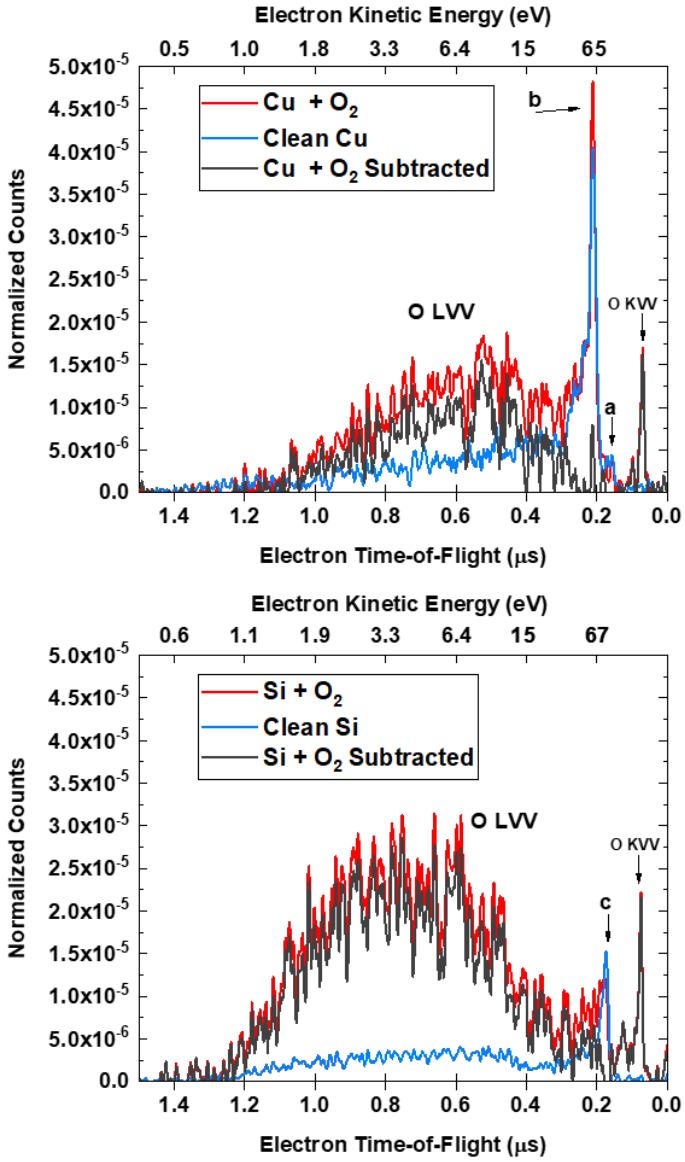

Figure 4.3: ToF-PAES measurements of O_2 exposed Cu and Si surfaces before and after background subtraction. Substantial low-energy intensity remains after subtracting contributions from the metal-derived Auger transitions.

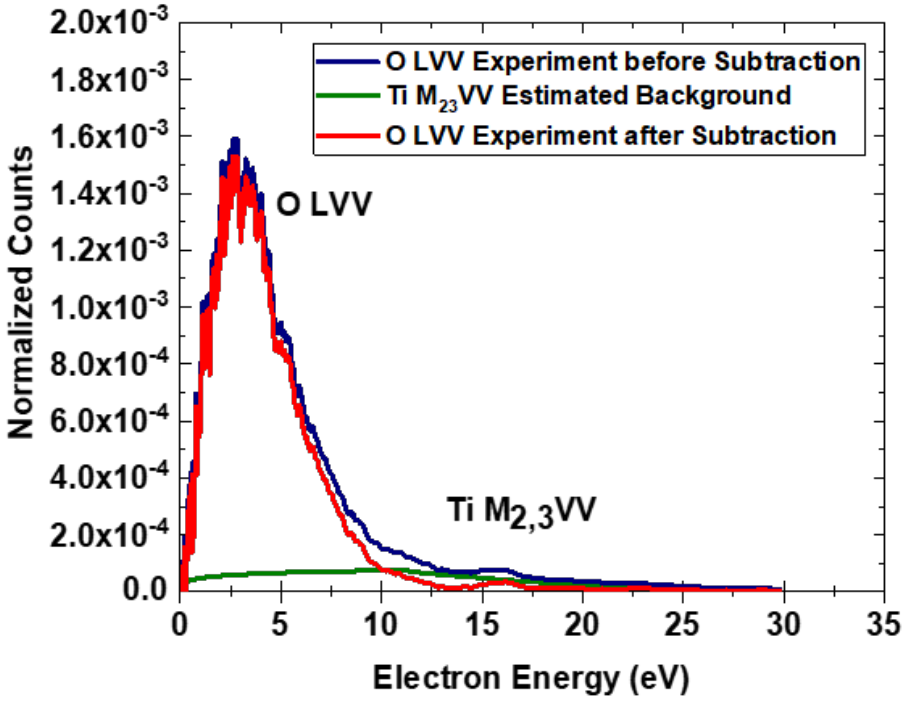

Figure 4.4: ToF-PAES measurements of TiO_2 before and after subtraction of the estimated inelastic tail of the Ti $M_{2,3}VV$ Auger peak shown in fig. 4.5. Substantial low-energy intensity remains after subtraction.

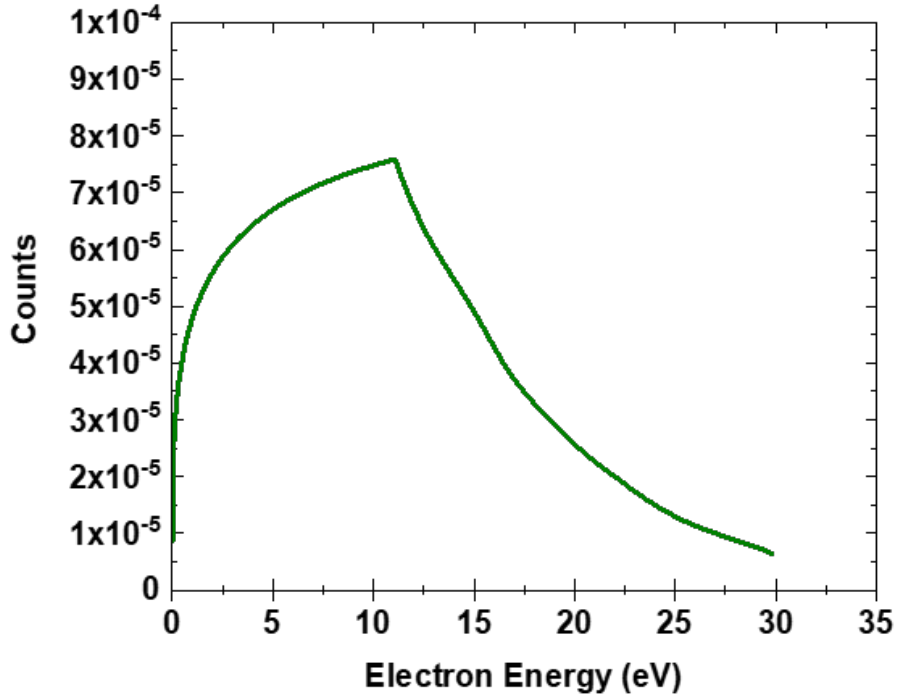

Figure 4.5: Calculated background due to inelastically scattered Ti $M_{2,3}VV$ Auger electrons using equation 4.1

4.4 Empirical O LVV Line Shape Model

We have constructed an empirical O LVV line shape model which consists of the convolution of the O KVV Auger peak line shape and the O 2s photoemission line. The principal difference between the O KVV and O LVV Auger processes is the initial energy that the system must dissipate —the difference in the oxygen 1s and 2s core binding energies. Any final state effects associated with the double ionized oxygen atom is present in both Auger processes and therefore the O LVV Auger line shape can be approximated by taking the measured O KVV line shape and shifting it to lower kinetic energies by the difference in the O 1s and O 2s binding energies.

Fig. 4.6 shows the O KVV Auger line shapes and O 2s photoemission lines for CuO [46, 47], SiO_2 [48, 49], and TiO_2 [50, 51] used in our empirical modelling. The XPS measured O 1s binding energies are very sharp, typical FWHMs are on the order of 1 eV, and so each O 1s binding energy was taken to be the peak of the O 1s photoemission line. The O 1s binding energies used were 529.4 eV, 532.8 eV, and 530.5 eV for CuO, SiO_2, and TiO_2 respectively. However, the O 2s photoemission lines are quite broad, see fig. 4.6, and it would not be appropriate to represent the O 2s photoemission line as simply the peak of the distribution. Therefore, we have taken the O KVV Auger line shapes, subtracted the O 1s binding energies, then convoluted them with the O 2s photoemission lines to account for the width and shape of the O 2s photoemission line on the Auger spectrum. Finally, an empirical function which models the probability that an electron has sufficient momentum parallel to the surface to overcome the surface dipole barrier was applied. This electron escape function ensures that the shifted O KVV line shape

has a more realistic low-energy edge reflecting the decreased probability that low-energy electrons have of overcoming the surface dipole barrier.

We calculate the electron escape function, $P_e(E)$ following the formalism of Hagstrum [52, 53] in which the escaping electron is treated as a classical particle that is diffracted at the surface. Hagstrum uses the bottom of the conduction band for metals as a reference energy for measuring the escaping electron's kinetic energy. Instead, we use the average potential in the bulk of the sample [54]. The energy inside the solid is given by $\varepsilon_{vac}-\varepsilon_{ref}$. The electron loses kinetic energy equal to the difference in energy between the reference energy and the vacuum level. Therefore, the critical angle of incidence, measured from the surface's normal, for which the particle retains a positive kinetic energy in the vacuum is:

$$\theta_c = \arccos\left(\sqrt{\frac{\varepsilon_{vac}-\varepsilon_{ref}}{\varepsilon_{vac}+E-\varepsilon_{ref}}}\right) \tag{4.2}$$

The electron escape function is then calculated from:

$$P_e(E) = \int_0^{2\pi} \mathrm{d}\phi \int_0^{\theta_c} P_\Omega(\theta,\phi,\varepsilon_{vac}+E)\ \mathrm{d}\theta \tag{4.3}$$

where $\mathrm{P}_\Omega(\theta,\phi,\varepsilon_{vac}+E)$ is the probability that the wave vector of the electron is in the direction (θ,ϕ) and is assumed to be isotropic i.e. $P_\Omega(\theta,\phi,\varepsilon_{vac}+E) = \frac{1}{4}\pi$. We take the z-axis to be along the surface normal and the resulting integration yields:

$$P_e(E) = \frac{1}{2}\left[1-\left(\frac{\varepsilon_{vac}-\varepsilon_{ref}}{\varepsilon_{vac}+E-\varepsilon_{ref}}\right)^{\beta}\right]^{\alpha} \tag{4.4}$$

where α and β are parameters introduced by Hagstrum to model the non-isotropy of the matrix elements. $\alpha = 0.25$ and $\beta = 0.5$ are used for all calculated electron escape functions presented in this thesis. For the materials considered in this thesis, the variations in the electron escape function due to the material dependent values of ε_{vac} and ε_{ref} are unimportant. This is to be expected since they only serve as reference values for the escaping electron's kinetic energy. For the electron escape function used in this chapter, we have used the values for the Cu sample, $\varepsilon_{vac} = 7.33$ and $\varepsilon_{ref} = -5.13$. The escape function generated using these parameters is shown in fig. 4.7.

The comparison between the background subtracted PAES spectra and the empirical, O KVV-derived O LVV model line shapes are shown in fig. 4.8. The left panels are comparisons in ToF while the right panels are comparisons in energy. To obtain a best fit with experiment, an additional rigid shift of -2.2 eV was applied to the CuO model, an additional rigid shift of -1.0 eV was applied to the TiO_2 model, and an additional rigid shift of -7.5 eV was applied to the SiO_2 model before application of the escape function. A different overall scale factor for each spectrum was chosen to bring the peak intensities into agreement. We note that a possibly reason for this additional rigid shift can be the incomplete parallelization of the outgoing electron momentum. This can cause the peak energies measured using the ToF technique to be shifted to lower energies, see chap. 3 and ref. [21]. It can also be due in part to differences in the total required energy to remove an electron from the solid, such as differences in the work functions or hole-hole correlations, between our experiment and the XPS measurements. Lastly, it could simply be that the O 2s photoemission data used is unrealistically wide due to improper

handling of the background subtractions.

Finally, we offer a few comments on the comparisons between the modelled and experimental line shapes. The best overall agreement is for the Si data with the Cu data suffering the worst agreement. The XPS data for CuO was taken on a well characterized oxide surfaces. Our experiment is not for a well characterized oxide surface but one that likely has many different oxygen species which are not uniformly covering the surface given the relatively small number of Langmuirs the clean Cu surface was exposed to. The disagreements in the widths of the SiO_2 and TiO_2 data can be due to initial and final state effects not considered. For example, greater relaxation or shielding of the initial O 2s core hole which would make the measured O LVV line shape narrower compared to the O KVV line shape. Additionally, there are known final state shake-up/off processes which have been observed to contribute intensity to the high-energy shoulder of the O KVV spectrum which should be absent from the O LVV line shape [48, 55, 56]. The extra intensity at higher energies in the Cu data could be due to Auger transitions final states in which the two holes are in separate oxygen atoms. It could also be that there are interatomic Auger transitions occurring between the Cu and O atoms. For example, a Cu 3p hole with binding energy $\sim$70 eV that is filled by O 2s electrons with binding energies $\sim$25 eV could easily give you electrons with kinetic energies extending up to 20 eV. One definite conclusion we can draw is that a significant number of O LVV Auger transitions result in electrons with sufficient kinetic energy to overcome the surface dipole barrier and escape into the vacuum. This coupled with the fact that the low-energy spectral weight is associated with the presence of oxygen at the surface, provides compelling

evidence that we are observing O LVV Auger electron emission.

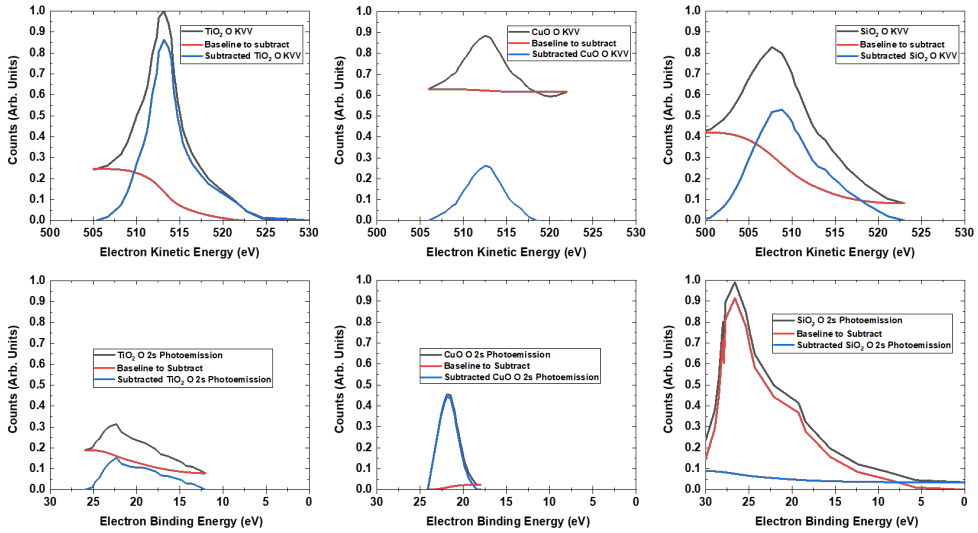

Figure 4.6: O KVV Auger and O 2s Photoemission spectra of TiO_2, CuO, and SiO_2 measured using XPS. The top panels are the digitized O KVV line shapes. The bottom panels are the digitized O 2s photoemission lines. The O KVV and O 2s line shapes are shown in black. The background subtracted line shapes are shown in blue. The baselines subtracted are shown in red. The red baselines are a Shirley background calculated using the algorithm implemented within OriginPro [1]. The CuO O KVV and O 2s line shapes were taken from [46] and [47]. The SiO_2 O KVV and O 2s line shapes were taken from [48] and [49]. The TiO_2 O KVV and O 2s line shapes were taken from [50] and [51].

[1] https://www.originlab.com/doc/Origin-Help/PA-Algorithm#XPS

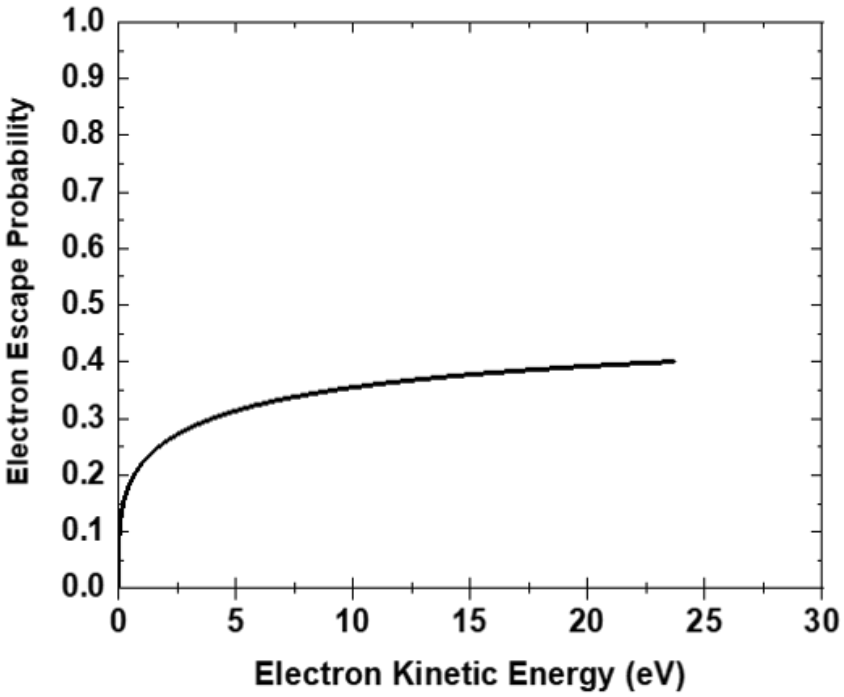

Figure 4.7: The empirically-derived electron escape function. The parameters used are $\alpha = 0.25$, $\beta = 0.5$, $\varepsilon_{vac} = 7.33$, and $\varepsilon_{ref} = -5.13$. All escape functions used in this thesis use these same values for α and β. The height and overall shape of the electron escape probability does not change with appropriate choices of the reference values for the escaping electron's kinetic energy, ε_{vac} and ε_{ref}.

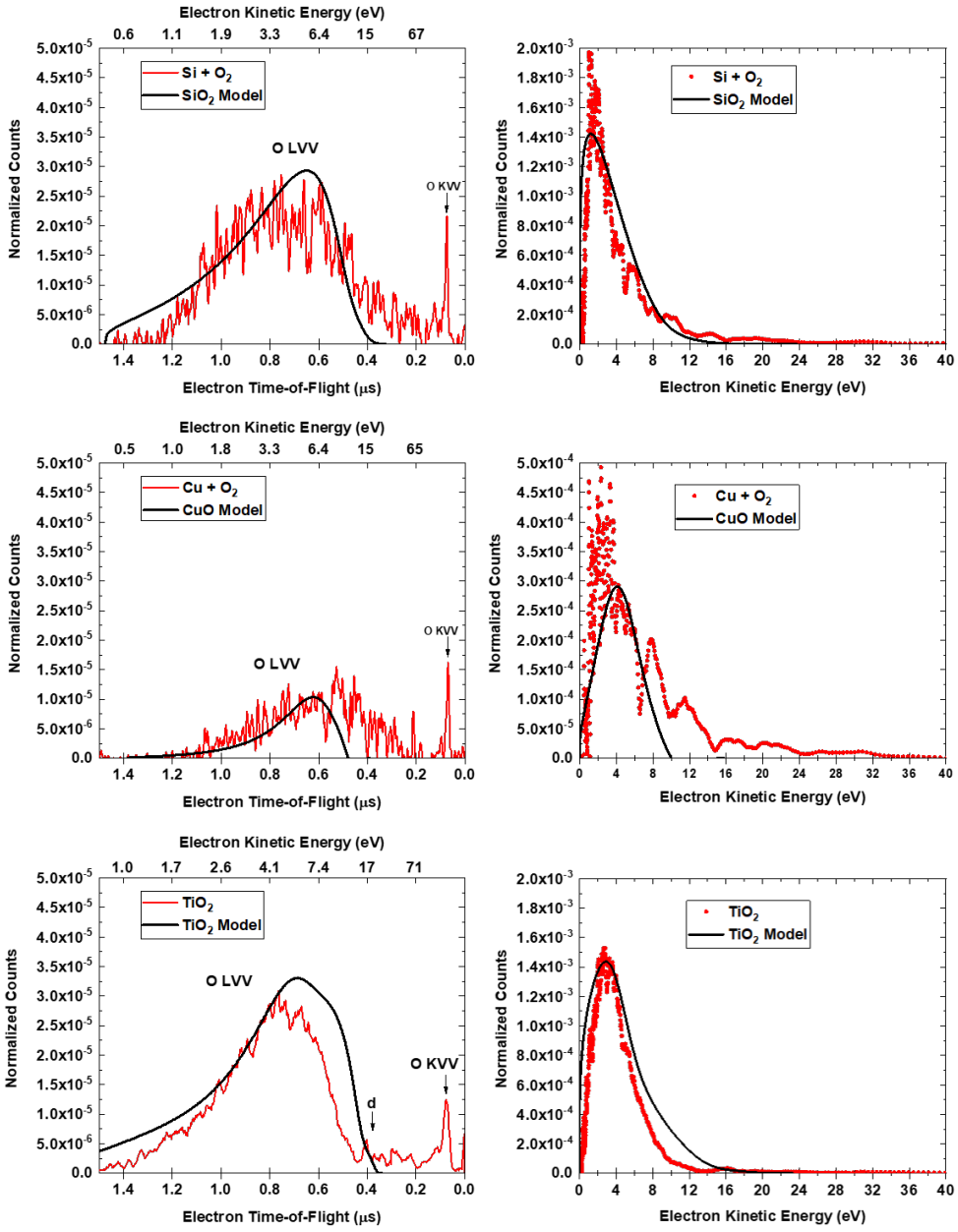

Figure 4.8: Comparison between the measured and empirically modelled O LVV line shapes for Si, Cu, and TiO_2 surfaces.

4.5 Theoretical O LVV Line Shape for TiO_2

In this section, we present a quantitative analysis of the O LVV line shape for TiO_2 which incorporates the self-convolution of the valence band density of states, the distribution of annihilation-induced O 2s holes, and an estimate of the electron escape probability. Given the preceding discussion about the complications arising in the empirical, O KVV-derived modelling of the O LVV line shape, we have chosen to calculate directly the O LVV line shape using the theoretically generated density of states for $TiO2_2$, [30]. Fig. 4.9 is a comparison between the ToF-PAES spectrum for TiO_2, alongside an instrumentally-broadened theoretical calculation of the O LVV Auger electron energy distribution for TiO_2. The O LVV line shape, $A_{O\ LVV}(E)$, was calculated using the typical self-convolution of the one-particle density of states used to describe band-like CVV Auger transitions [5, 57, 58]:

$$A_{\ O\ LVV}(E) = P_e(E) \iiint \rho_h(\varepsilon_h)\,\rho(\varepsilon_1)\,\rho(\varepsilon_2)\,\delta(\varepsilon_h - \varepsilon_1 - \varepsilon_2 - \phi - E)\,d\varepsilon_h\,d\varepsilon_1\,\mathrm{d}\varepsilon_2 \tag{4.5}$$

where E is the kinetic energy of the emitted Auger electron, ε_h, ε_1, and ε_2 are the binding energies of the participating electrons and ϕ is the energy required to remove an electron from the solid, see figure 4.1. P_e(E) is the electron escape probability detailed in the preceding section. $\rho_h(\varepsilon_h)$ is the state-dependent density of annihilation-induced holes and $\rho(\varepsilon)$ is the calculated density of states shown in blue in figure 4.1. δ is the energy conserving delta function. The density of annihilation-induced holes was approximated using the calculated density of O 2s states, shown in red in

figure 4.1, which corresponds to the assumption of a relatively constant partial annihilation rate. The calculated spectrum was shifted to lower kinetic energies by 8.2 eV to account for the combined effects of the electron work function and final state hole-hole correlation effects. The calculated O LVV Auger spectrum was used as an input to a SIMION®8.1 simulation of our ToF-PAES spectrometer to account for the effects of instrumental broadening on the outgoing electron energy distribution. Additional details of the simulated ToF-PAES spectrometer and its effects on the calculated Auger spectra can be found in references [13, 20]. Finally, an overall scale factor was applied to bring the experimental and calculated peaks into agreement.

The excellent agreement between the measured and calculated line shapes provides strong evidence that the observed low-energy peak is a result of O LVV Auger decay processes. We note that the disagreement between 7 and 12 eV between the experiment and the calculation is likely due to final states in which the two holes are in separate oxygen atoms, which is not included in our calculation of the line shape. These final states have reduced hole-hole repulsion and hence can result in the emission of electrons with higher kinetic energy. This has been identified in other metal oxide systems previously [59] and has been reported in the Auger-like decay of inner-valence holes, which are of predominantly O 2s character, in hydrogen-bonded water clusters [60]. Our modelling of the O LVV line shape shows that the maximum kinetic energy available to the outgoing O LVV Auger electrons is $\sim$9.5 eV, when the two final holes are localized at a single atomic site. This provides a direct measure of the maximum energy available for other processes such as Auger-stimulated desorption following the filling of an O 2s hole [61].

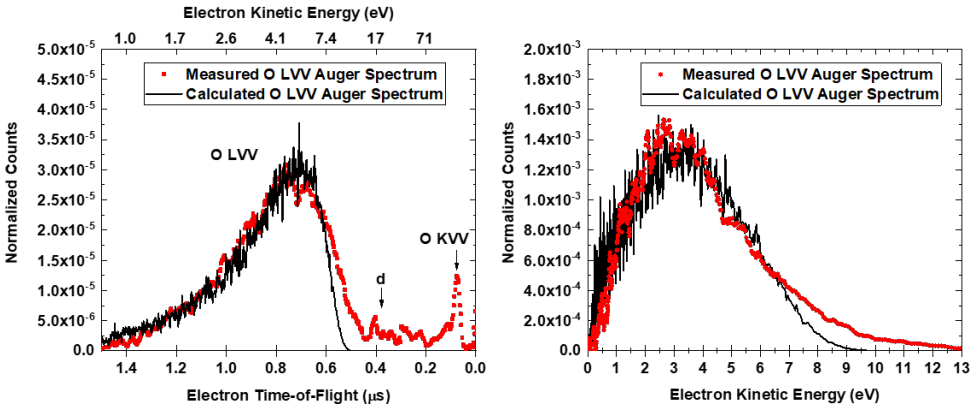

Figure 4.9: Measured and calculated O LVV Auger electron spectrum for TiO_2. Comparison between the ToF-PAES spectrum from TiO_2 (red) and a calculation of the O LVV Auger spectrum from TiO_2 (black) using equation 4.5. An estimate of the low-energy tail due to inelastically scatted Ti $M_{2,3}VV$ Auger electrons has been subtracted from the measured O LVV Auger peak that amounts to ∼9% of the total intensity. The calculated spectrum has been broadened using a charged particle trajectory simulation of our ToF-PAES spectrometer.

4.6 Annihilation Probability with O 2s Electrons

In this section, we calculate the annihilation probability for a positron with an O 2s electron of TiO_2 using the calculated O LVV line shape, the measured PAES intensities, and estimates of the various loss processes that occur during the Auger electron emission and transport to the detector.

The number of core-valence-valence (CVV) Auger electrons, N_{CVV}, detected in our experiment is given by:

$$N_{CVV}(E) = N_{ss}\,\lambda_{n,l}\,A_{CVV}\,f_{CVV}(E)\,P_e(E)\,T(E)\,\eta(E)\,\varepsilon_{BaF_2}\,\varepsilon_{MCP} \qquad (4.6)$$

where N_{ss} is the number of surface state annihilations, $\lambda_{n,l}$ is the annihilation probability for electrons with principal quantum number n and angular momentum quantum number l, A_{CVV} is the probability that a core hole C will decay via a CVV Auger transition, $f_{CVV}(E)$ is the probability that a CVV Auger transitions will result in an electron emitted with energy E, $P_e(E)$ is the electron escape function, T(E) is the transmission factor —which takes into account the inelastic mean free path of electrons generated from an escape depth z below the surface and models the probability that an electron generated within the material escapes with energy E without scattering [62], η(E) is the simulated transport efficiency of our ToF-PAES spectrometer and gives the probability that an electron travelling with kinetic energy E will reach the MCP detector, ε_{BaF_2} is the BaF_2 detector efficiency, and ε_{MCP} is the MCP detector efficiency.

The integrated intensity of the CVV Auger peak is then found by inte-

grating N_{CVV} over the appropriate energy range:

$$I_{CVV}(E) = N_{ss}\,\lambda_{n,l}\,A_{CVV}\,\varepsilon_{BaF_2}\,\varepsilon_{MCP}\int_{E_1}^{E_2} P_e(E)\,f_{CVV}(E)\,T(E)\,\eta(E)\;\mathrm{d}E \tag{4.7}$$

The number of surface state annihilations (N_{ss}) is a fairly straight forward quantity to measure using either a scintillation or semiconductor detector. The Auger efficiency (A_{CVV}) in principle can be measured but often is assumed to be unity for sufficiently deep core levels [63, 64]. The electron escape function, P_e(E) has been discussed in the preceding section and η(E) is detailed in chap. 3. The annihilation probability ($\lambda_{n,l}$) and the fraction of Auger transitions which result in Auger electrons with energies above the vacuum level ($f_{CVV}(E)$) will be discussed later in this section.

The transmission factor, T, can be calculated following the formalism of Seah [62]. Assuming a condensate of n uniform layers, the Auger current emitted from the substrate at an angle θ from the surface normal is given by:

$$I_n(\theta)\,\mathrm{d}\Omega = I_0\,\frac{A_s}{S}\int_0^{\infty}\exp(-\frac{z}{l_s^S\,\cdot S\cdot\cos(\theta)})\,\exp(-\frac{n}{l_c^S\,\cdot\cos(\theta)})\;\mathrm{d}z\,\mathrm{d}\Omega \tag{4.8}$$

where I_0 is the primary electron beam current, A_s is the Auger emission current per unit solid angle per incident electron for the substrate atoms, S is the thickness of each substrate atom layer, z is the depth below the substrate-condensate interface, l_s^S and l_c^S are the inelastic mean free paths (IMFPs) of the substrate Auger electrons in the substrate and condensate respectively. The Auger electron current is assumed to be produced uniformly as a function of z and emitted isotropically into the vacuum. Since in electron-stimulated Auger electron spectroscopy the depth at which Auger electrons can be created

is determined by the penetration depth of the incident electrons, which is much greater than the IMFP of the escaping electrons, the integration limit is set to infinity.

We are interested in the transmission factor for an adsorbate free TiO_2 surface and so we take n = 0. Additionally, in PAES since the Auger electron emission is from the top-most atomic layer we take S = 1, remove the integration over z, and take z to be the half-thickness of the first atomic layer of TiO_2. Thus, we arrive at an expression for the Auger electron emission in PAES given by:

$$I(\theta)\,\mathrm{d}\Omega = I_0\,A_s \iint_0^{\frac{\pi}{2}} \exp(-\frac{z}{l_s\,\cdot\cos(\theta)})\,\sin(\theta)\;\mathrm{d}\theta\,\mathrm{d}\phi \qquad (4.9)$$

where I_0 is now the number of positrons annihilating in the surface state and z = 1.95 Å for TiO_2 [65].

The transmission factor, T, then is defined as:

$$T = \frac{I(\theta)\,\mathrm{d}\Omega}{I_0\,A_s\,\iint_0^{\frac{\pi}{2}}\mathrm{d}\Omega} = \frac{\int_0^{\frac{\pi}{2}}\exp\left(-\frac{z}{l_s\cdot\cos(\theta)}\right)\sin(\theta)\;\mathrm{d}\theta}{\int_0^{\frac{\pi}{2}}\sin(\theta)\;\mathrm{d}\theta} \qquad (4.10)$$

Lastly, the transmission factor, T(E), is energy dependent because electrons with different kinetic energies have different IMFPs. In this dissertation, we use Seah's parameterization for the universal curve of the electron IMFP [66]:

$$l(E) = \frac{143}{E^2} + 0.054\,\cdot\sqrt{E} \qquad (4.11)$$

The resulting l(E) is given in nm provided E is given in eV.

We estimate the probability that a positron annihilates with an O 2s electron at the surface of TiO_2 using the ratio of measured O LVV to O KVV integrated PAES intensities so that the detector efficiencies and the number of surface state annihilations are eliminated. Equation 4.7 then reads:

$$\frac{I_{\mathrm{O\ LVV}}(E)}{I_{\mathrm{O\ KVV}}(E')} = \frac{\lambda_{\mathrm{O\ 2s}}\, A_{\mathrm{O\ LVV}} \int_{E_1}^{E_2} P_e(E)\, f_{\mathrm{O\ LVV}}(E)\, T(E)\, \eta(E)\ \mathrm{d}E}{\lambda_{\mathrm{O\ 1s}}\, A_{\mathrm{O\ KVV}} \int_{E_3}^{E_4} P_e(E')\, f_{\mathrm{O\ KVV}}(E')\, T(E')\, \eta(E')\ \mathrm{d}E'} \quad (4.12)$$

where $\lambda_{\mathrm{O\ 2s}}$ and $\lambda_{\mathrm{O\ 1s}}$ are the 2s and 1s annihilation probabilities respectively. $\mathrm{I_{O\ LVV}}$ and $\mathrm{I_{O\ KVV}}$ are the measured integrated PAES intensities and $\mathrm{A_{O\ LVV}}$ and $\mathrm{A_{O\ KVV}}$ are the Auger efficiencies. The calculated O LVV line shape, normalized to unity, is taken to represent the probability that an Auger electron is emitted through an O LVV process with energy E. The XPS measurement of the O KVV line shape in fig. 4.6, normalized to unity, is taken to represent the probability that an Auger electron is emitted through an O KVV process with energy E'.

Equation 4.12 can be rearranged to give the ratio of O 2s to O 1s annihilation probabilities in terms of the measured ratio of O LVV to O KVV integrated intensities, the ratio of O KVV to O LVV Auger efficiencies, and the ratio of the calculated loss processes:

$$\frac{\lambda_{\mathrm{O\ 2s}}}{\lambda_{\mathrm{O\ 1s}}} = \frac{I_{\mathrm{O\ LVV}}(E)}{I_{\mathrm{O\ KVV}}(E')} \frac{A_{\mathrm{O\ KVV}}}{A_{\mathrm{O\ LVV}}} \frac{\int_{E_3}^{E_4} P_e(E')\, f_{\mathrm{O\ KVV}}(E')\, T(E')\, \eta(E')\ \mathrm{d}E'}{\int_{E_1}^{E_2} P_e(E)\, f_{\mathrm{O\ LVV}}(E)\, T(E)\, \eta(E)\ \mathrm{d}E} \quad (4.13)$$

The estimate of the O 2s annihilation probability resulting from this analysis, along with the relevant quantities used in the calculation, are listed in table 4.1.

$I_{\text{O LVV}}$	$I_{\text{O KVV}}$	$\frac{I_{\text{O LVV}}}{I_{\text{O KVV}}}$	$\frac{A_{\text{O KVV}}}{A_{\text{O LVV}}}$	$\frac{\lambda_{\text{O 2s}}}{\lambda_{\text{O 1s}}}$	$\lambda_{\text{O 1s}}$	$\lambda_{\text{O 2s}}$
6.95×10^{-3}	1.62×10^{-4}	43 ± 3	1	52 ± 3	0.1 [67]	5.2 ± 0.3

Table 4.1: Table of quantities used in equation 4.13 to estimate $\lambda_{\text{O 2s}}$. The error bars reflect the statistical uncertainty in the measurements.

We have also calculated the ratio of the O 2s to the O 1s positron annihilation probabilities theoretically. The positron annihilation rate, λ, with a given electronic level i is given by:

$$\lambda_i = \frac{\pi\, r_0^2\, c}{e^2} \int n^+(\mathbf{r})\, n_i^-(\mathbf{r})\, \gamma(n_i(\mathbf{r}))\ \mathrm{d}^3\mathbf{r} \tag{4.14}$$

where r_0 is the classical electron radius, n^- is the electron charge density, n^+ is the positron charge density, and γ is the enhancement factor. The enhancement factor takes into account the fact that electrons are attracted to the positively charged positron which increases the positron-electron overlap and hence the positron annihilation rate. A standard self-consistent-field atomic program, which has been utilized previously in simulating the two-detector Doppler-broadening spectra [68], was used to calculate the oxygen electron orbitals. The positron wave function was determined from the positron Schrödinger equation using the the calculated electron charge densities with the positron-electron correlation parameterization of Sterne and Kaiser [69]:

$$V_{e^-e^+}(r_s) = -1.56\ \arctan(r_s)^{-\frac{1}{2}} + 0.1324\ \exp\left(-\frac{(r_s - 4.092)^2}{51.96}\right) + 0.7207 \tag{4.15}$$

where r_s is the size of a sphere containing 1 electron given the calculated electron charge density, n_i^-, i.e. $\frac{4\pi}{3} r_s^3 \, n_i^- = 1$. Finally, we have used the parameterization of the enhancement factor of Barbiellini et al. [70]:

$$\gamma(r_s) = 1 + 1.23\, r_s - 0.0742\, r_s^2 + \frac{1}{6}\, r_s^3. \tag{4.16}$$

The resulting calculation gives $\frac{\lambda_{\text{O 2s}}}{\lambda_{\text{O 1s}}} = 48$. The reason that the positron is nearly 50 times as likely to annihilate with an O 2s electron as an O 1s electron is because of the much larger positron wave function overlap with the O 2s electron charge density, see fig. 4.10. The theoretically calculated ratio of 48 compares favorably with the experimentally-derived ratio of 52 $\pm$ 3. We note that in our modelling we have assumed that the Auger decay probability for the L shell vacancy is equal to that of the the K shell vacancy. The agreement between our measured and theoretical ratio supports this assumption. It has previously been shown that the Auger decay probability for the oxygen K shell hole is close to 1 [63, 71]. Hence, we conclude that the Auger decay probability of O 2s holes is also close to unity.

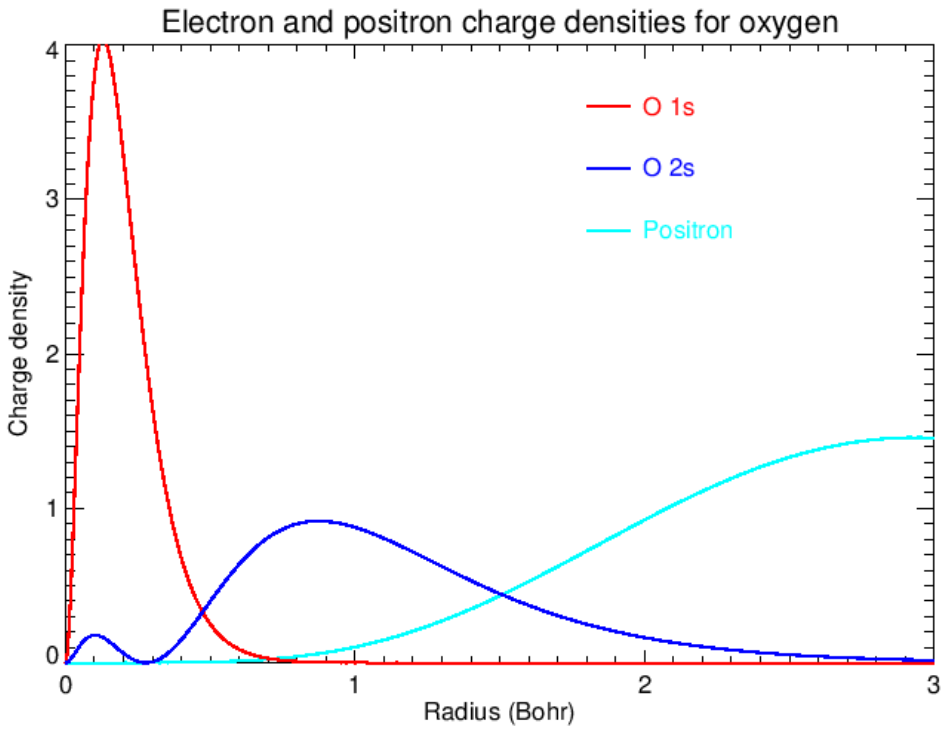

Figure 4.10: Calculated electron and positron charge densities for oxygen[2]. The reason that the positron is nearly 50 times as likely to annihilate with an O 2s electron as an O 1s electron is because of the much larger positron wave function overlap with the O 2s electron charge density.

[2]Courtesy of Philip A. Sterne (sterne1@llnl.gov), Lawrence Livermore National Laboratory

4.7 Concluding Remarks

In this chapter, we have presented ToF-PAES measurements of the low-energy Auger electron spectra from oxygen adsorbed Cu and Si surfaces and a TiO_2 surface. These spectra contain large contributions from Auger processes consistent with LVV Auger transitions in oxygen. Low-energy Auger electron spectra are particularly difficult to observe and study using traditional electron or photon stimulated AES due to the obscuring, beam-induced secondary electron background. We have overcome this background limitation by using mater-antimatter annihilations to initiate the Auger process. We believe these results to be the first quantitative investigations of these O LVV Auger transitions in condensed matter systems.

The major findings of this chapter are as follows:

(1) The increased low-energy intensity for oxygen on Cu and Si, and the broad, low-energy peak in TiO_2 are each associated with the presence of oxygen on the surface, as indicated by the emergence of the O KVV Auger peaks. An analysis of the integrated PAES intensities shows that the change in the low-energy intensity is 4 times the change in the Cu $M_{2,3}VV$ and 18 times the change in the Si $L_{2,3}VV$. This increased intensity cannot be explained by competing processes such as inelastic scattering of outgoing Auger electrons or secondary electron emission mechanisms.

(2) We have constructed an empirical O LVV line shape model which consists of the convolution of the O KVV Auger peak line shape and the O 2s photoemission line. This empirical model provide compelling evidence that a significant number of O LVV Auger transitions result in electrons with sufficient kinetic energy to overcome the surface dipole barrier and escape

into the vacuum.

(3) We have calculated theoretically the O LVV electron energy distribution from TiO_2 using a first principals based model which incorporates the self-convolution of the density of states, an estimate of the distribution of annihilation-induced O 2s holes, and an estimate of the electron escape function. We found excellent agreement between the measured O LVV Auger spectrum from the TiO_2 surface and this calculation.

(4) We have estimated the positron annihilation probability with the oxygen 2s levels at the surface of TiO_2 using the measured O LVV and O KVV integrated PAES intensities. The experimental intensities have been corrected for (1) the probability that an O LVV Auger transition results in an electron with sufficient energy and momentum to escape the material, (2) the effects of the inelastic mean free path of the escaping electron, and (3) the transport efficiency through our spectrometer. After correcting the experimental PAES intensities, we find $\frac{\lambda_{O\ 2s}}{\lambda_{O\ 1s}}$ to be 52 ± 3 which compares favorably with the ratio 48 calculated theoretically. We find $\lambda_{O\ 2s}$ to be 5.2% $\pm$ 0.3% assuming $\lambda_{O\ 1s}$ to be 0.1% [67].

(5) The estimate of $\frac{\lambda_{O\ 2s}}{\lambda_{O\ 1s}}$ was made assuming that the Auger decay probability for the L shell vacancy is equal to that of the the K shell vacancy. The agreement between our measured and theoretical ratio supports this assumption. Since the Auger decay probability for the oxygen K shell hole is close to 1 [63, 71] we conclude that the Auger decay probability of O 2s holes is also close to unity.

Finally, the results presented in this chapter may be of significant importance in studies of Auger-stimulated ion desorption and photodynamic cancer therapies.

First, the experimental verification of the positron surface state on the TiO_2(110) surface, measurement of the relative annihilation probabilities for the oxygen and titanium core levels, and the direct measurement of the maximum energy available following the filling of an O 2s hole are all important for the current understanding of positron-stimulated desorption of O^+ [41, 61].

Second, the unambiguous identification of this previously unexplored, Auger emission process has implications for photodynamic cancer therapies because O LVV Auger decay (1) is an efficient mechanism for the emission of low-energy, genotoxic electrons and (2) leads to the creation of chemically active, multi-hole final states in one or more oxygen atoms. Since TiO_2 is widely used in biomedical applications, and low-energy electrons play a crucial role in the nascent stages of DNA radiolysis through dissociative electron attachment (DEA) [72], it is essential that the various mechanisms that can produce low-energy electrons in TiO_2 be identified and thoroughly understood. In particular, TiO_2 nanoparticles have recently been used in photo-assisted cancer therapies which utilize the emission of low-energy electrons from TiO_2 to produce reactive oxygen species [33, 73]. Finally, energetic hole states, like those found in the final state of the O LVV Auger processes, have been found to contribute directly to the TiO_2-assisted production of cytotoxic singlet oxygen [74] and have been shown to trigger the Coulomb explosion of water molecules producing reactive oxygen species [75, 76].

Chapter 5

5.1 Introduction

In this chapter, we present observations and analysis of valence-valence-valence (VVV) Auger transitions which result in the emission of electrons from single-layer graphene (SLG) on polycrystalline Cu. These measurements were made possible by the unique capabilities of UTA's positron beam system to transport extremely low-energy positrons (< 1 eV) while simultaneously transporting electrons with energies from 0 eV to 500 eV. Using this unique capacity, we have measured the spectra of electrons emitted solely as a result of Auger transitions down to 0 eV. The direct observation of this low-energy electron emission process was only possible because of the elimination of the beam-induced secondary electron background which overwhelms the signal. Previous measurements have only been capable of indirect investigations due to this background [77, 78]. Comparison of the ratio of positron annihilation-induced Auger electron spectroscopy (PAES) integrated intensities of the C VVV Auger peak to the C KVV Auger peak indicates that the VVV Auger process is likely the predominant decay mode of deep valence holes in

graphene.

The VVV Auger emission process is initiated when a surface trapped positron annihilates with a valence electron at the surface. The resulting annihilation-induced hole is subsequently filled by a second valence electron which transfers its energy to a third electron in the valence band. This VVV Auger electron may be emitted into the vacuum provided it has gained sufficient energy from the VVV Auger transition to overcome the surface dipole barrier. This process is schematically represented in Fig. 5.1 for the calculated SLG density of states [13].

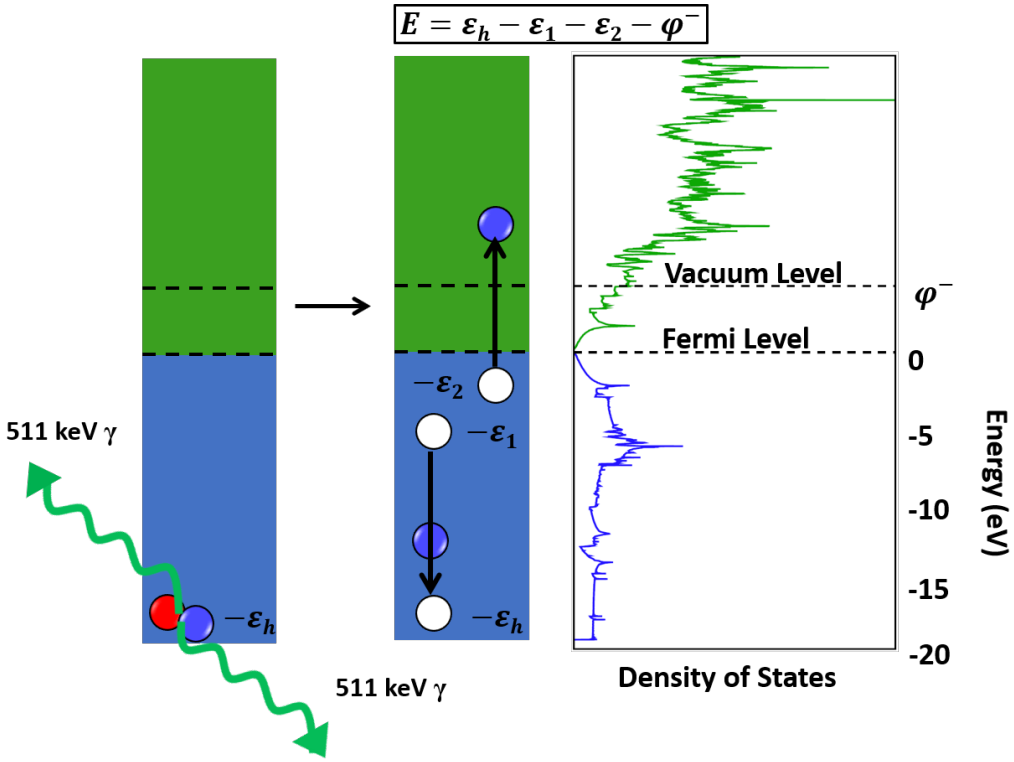

Figure 5.1: Schematic representation of a VVV Auger emission process. The process is initiated by the creation a valence band hole, with binding energy ε_h, via annihilation of the incident positron with a surface-bound valence electron accompanied by the emission of two 511 keV annihilation gamma photons (left-most box). Then, a less tightly bound electron, with binding energy ε_1, fills this vacant electronic state and the energy associated with this transition is coupled to a third electron in the valence band, with binding energy ε_3, which may escape the material, with kinetic energy E, provided is has acquired sufficient energy to overcome the electron work function, ϕ^- (middle box). The far-right box contains a calculation of the DOS of free-standing graphene [13].

5.2 Experimental Details

The experiments presented in this chapter were performed using the University of Texas at Arlington's positron beam system described in chapter 2. The sample chamber is kept at a base pressure less than 10^{-8} Pa. The incident positron beam energy was measured to be less than 1.5 eV using a retarding field analyzer. The polycrystalline Cu sample was sputter cleaned every 24 hours to remove any residual gasses from the surfaces. The SLG was CVD grown on a polycrystalline Cu substrate and was purchased from ACS materials. The SLG sample was installed into UHV as-received. No additional surface modifications were made prior to measurements. The presence of SLG on Cu was confirmed using Raman spectroscopy on a small section cut from the same SLG on Cu sheet, see fig. 5.2. To obtain the clean Cu PAES spectrum, the SLG on Cu sample was sputtered using Ar ions at a pressure of 5×10^{-6} Torr with a sputtering current of $< 1\ \mu A$. Each spectrum has been divided by a number proportional to the number of positrons annihilating at the sample as determined using a NaI(Tl) detector mounted near the sample.

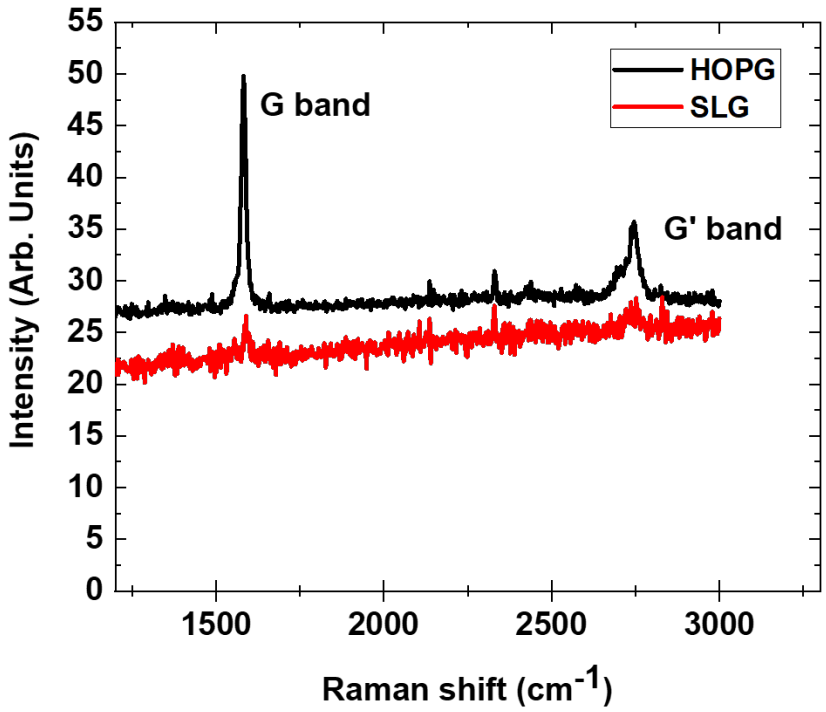

Figure 5.2: Measured Raman spectra for SLG and HOPG using 473 nm (2.62 eV) laser. The SLG data has been shifted down vertically by 10 for display purposes. The G band is located at ∼1582 cm^{-1} and the G' band at ∼2700 cm^{-1}. Both of these peaks are due to the excitation of in-plane phonon modes [79].

5.3 Experimental Results

The time-of-flight positron annihilation-induced Auger electron spectra (ToF-PAES) for SLG on polycrystalline Cu is presented in Fig. 5.3. The measured ToF-PAES spectrum obtained from the underlying Cu substrate, was obtained after removal of SLG by Ar sputtering. The SLG spectrum exhibits peaks to the Auger decay of annihilation-induced 1s holes in carbon (C KVV), 1s holes in oxygen (O KVV), 3p holes in Cu (Cu $M_{2,4}VV$) due to the underlying Cu substrate, and a broad, low-energy peak. The Cu spectrum exhibits peaks due to the annihilation-induced 3p holes in Cu (Cu $M_{2,4}VV$) and 3s holes in Cu (Cu M_1VV). The peak at $\sim$4 eV in SLG is absent in Cu and is ascribed to VVV Auger transitions. The Cu spectrum does not exhibit this peak due to the valence band width of Cu being too narrow to energetically permit VVV Auger electron emission. The low-energy SLG spectrum has been corrected for the low-energy tail (LET) associated with the Cu $M_{2,4}VV$ peak, see fig. 5.4. A fit to the energy-converted clean Cu spectrum was obtained using an exponential modified Gaussian. This fitting function was scaled by the differences in integrated Cu $M_{2,4}VV$ peak intensities before being subtracted from the experimental SLG spectrum.

The integrated intensity of the low-energy (0 eV to 30 eV) portion of the Cu spectrum is $\sim$1.7 times the integrated intensity of the Cu $M_{2,4}VV$ peak. The integrated intensity of the low-energy SLG spectrum from 0 eV to 11 eV is more than an order of magnitude larger than the integrated intensities of the higher energy Auger peaks. This is too large an intensity to be accounted for by inelastic scattering of outgoing Auger electrons, as evidence by the comparison to the clean Cu data.

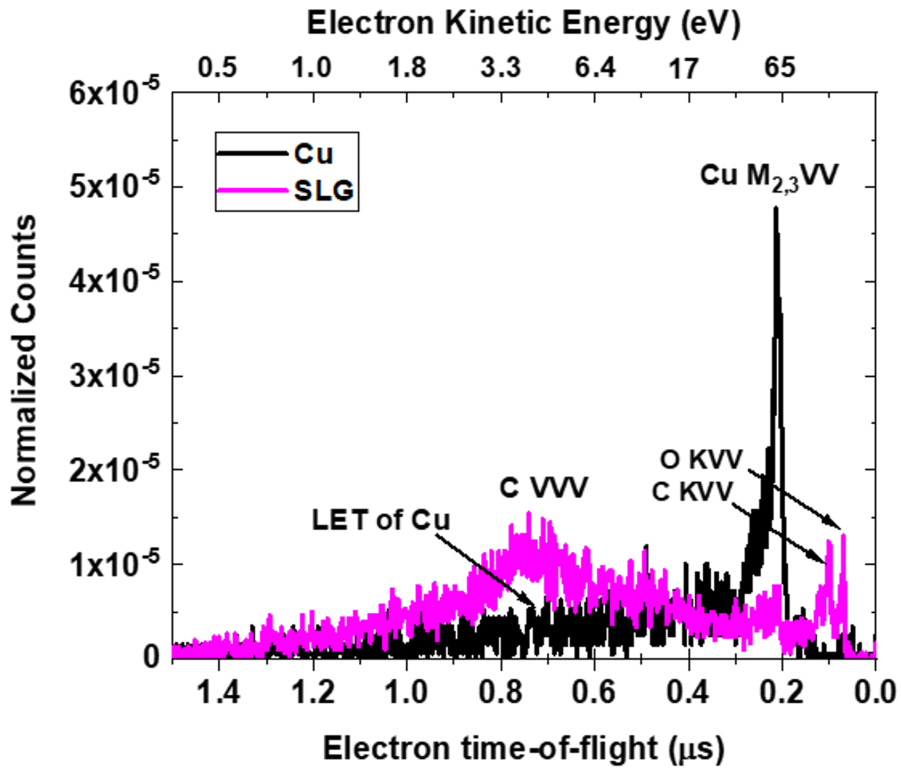

Figure 5.3: Measured ToF-PAES for Cu and SLG. ToF spectra of electrons emitted following the Auger decay of positron annihilation-induced holes. The bottom axis is the time the electrons take to travel 1 m. The top axis is the corresponding kinetic energy calculated from the ToFs. The peak at ∼4 eV in the SLG spectrum is the result of VVV Auger transitions. This peak is notably absent in the clean Cu spectrum since the valence band is not sufficiently deep to permit VVV Auger emission.

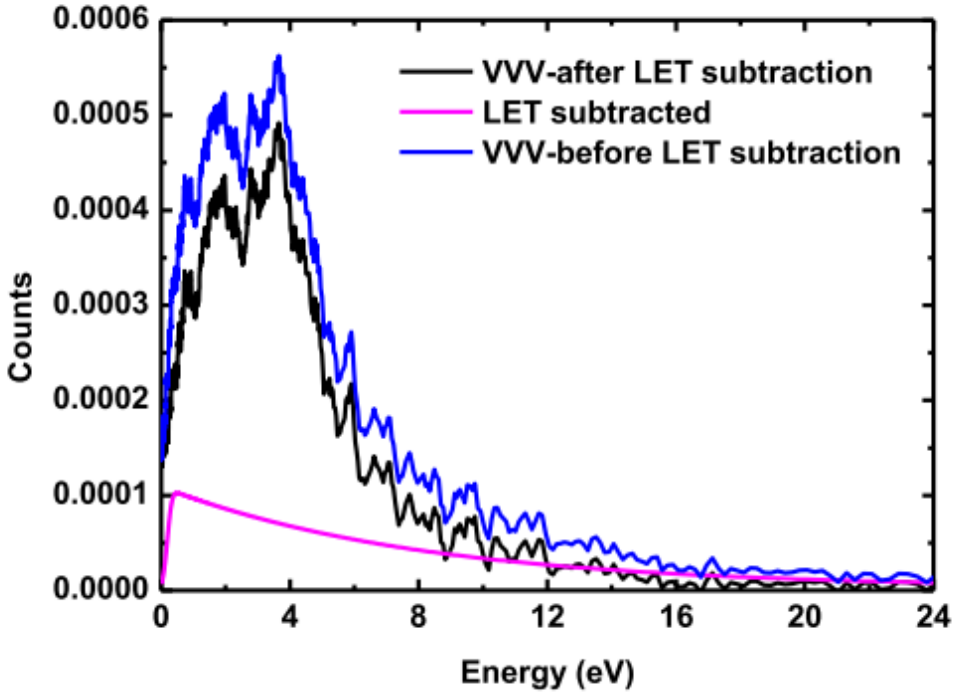

Figure 5.4: ToF-PAES measurements of SLG before and after subtraction of the low-energy tail associated with the Cu $M_{2,4}VV$ peak.

5.4 Theoretical VVV Line Shape

The energy-converted ToF-PAES spectrum for SLG, is shown alongside an instrumentally-broadened theoretical calculation of the VVV Auger electron energy distribution for SLG in fig. 5.5. The details of the electronic structure and positron calculations can be found in references [13, 54]. The VVV Auger electron energy distribution, $A_{VVV}(E)$, was calculated according to:

$$A_{VVV}(E) = P_e(E)\,\rho_c(E) \int \frac{\lambda_h(\varepsilon_h)\,T(\varepsilon_h, E)}{N(\varepsilon_h)}\,\mathrm{d}\varepsilon_h \tag{5.1}$$

where E is the kinetic energy of the emitted Auger electron, ε_h is the binding energy of the annihilation-induced hole, P_e(E) is the electron escape probability, $\lambda_h(\varepsilon_h)$ is the state-dependent density of annihilation-induced holes, $\rho_c(E)$ is the calculated density of conduction states shown in green in figure 5.1 and $T(\varepsilon_h, E)$ is the Auger transform.

The Auger transform is the typical self-convolution of the valence band density of states given by:

$$T(\varepsilon_h, E) = \iint \rho_v(\varepsilon_1)\,\rho_v(\varepsilon_2)\,\delta(\varepsilon_h - \varepsilon_1 - \varepsilon_2 - \phi - E)\,\Theta(\varepsilon_1 > \varepsilon_h)\,\mathrm{d}\varepsilon_1\,\mathrm{d}\varepsilon_2 \tag{5.2}$$

where ε_1 and ε_2 are the binding energies of the participating electrons, ρ_v is the calculated density of valence states shown in blue in fig. 5.1, ϕ is the energy required to remove an electron from the solid, δ is the energy conserving delta function, and Θ is the Heaviside step function which ensures that the hole in the valence band is filled by an electron from a higher energy state.

$N(\varepsilon_h)$ is a normalization factor counting all possible VVV transitions i.e.

$$N(\varepsilon_h) = \iiint \rho_c(\varepsilon_f)\rho_v(\varepsilon_1)\rho_v(\varepsilon_2)\delta(\varepsilon_h - \varepsilon_1 - \varepsilon_2 - \phi_s^- - \varepsilon_f)\Theta(\varepsilon_1 > \varepsilon_h) d\varepsilon_1\, d\varepsilon_2\, d\varepsilon_f \tag{5.3}$$

where ε_f is the final state binding energy.

The state-dependent density of annihilation-induced holes was obtained by an integral over the Brillouin zone:

$$\lambda(\varepsilon_h) = \frac{1}{\Omega} \sum_i \int_\Omega \lambda_i(\mathbf{k})\, f(\varepsilon_i(\mathbf{k}))\, \delta(\varepsilon_h - \varepsilon_i(\mathbf{k}))\, \mathrm{d}\mathbf{k} \tag{5.4}$$

where the sum is over all electronic states, i denotes a set of band and spin indices, and f gives the occupation numbers. Ω is the volume of the Brillouin zone. The partial annihilation rates are then obtained from:

$$\lambda_i(\mathbf{k}) = \pi r_e^2 c \int |\psi_{i,\mathbf{k}}^-(\mathbf{r})|^2\, |\psi^+(\mathbf{r})|^2\, \gamma(n_c^e(\mathbf{r}) + n^*(\mathbf{r}))\, \mathrm{d}\mathbf{r} \tag{5.5}$$

where r_e is the classical electron radius, ψ^- and ψ^+ are the electron and positron wave functions respectively, and γ is the enhancement factor written in terms of the charge densities. The calculated partial annihilation rates are relatively constant and follow the calculated density of states shown in fig. 5.1.

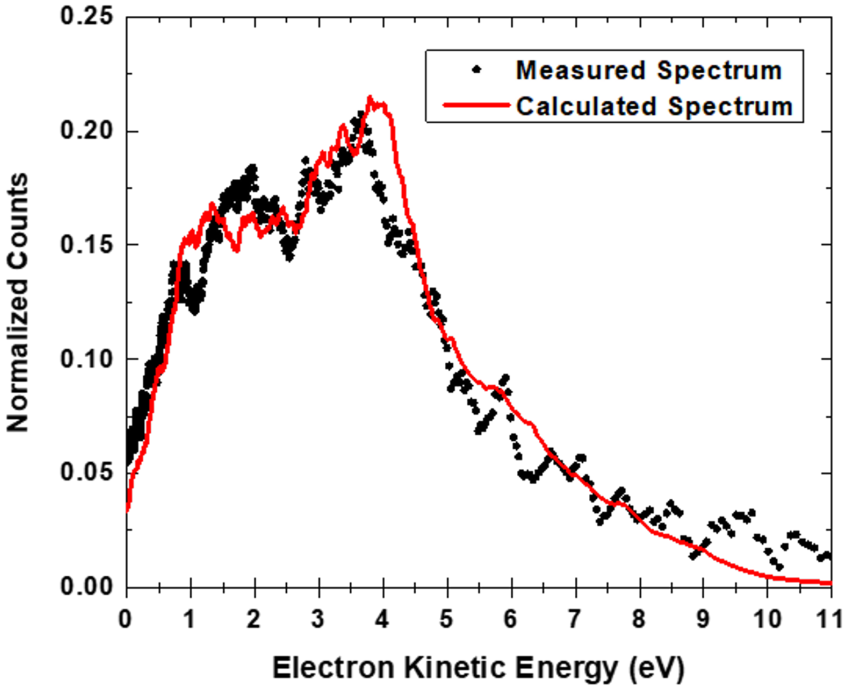

Figure 5.5: Measured and calculated VVV Auger electron energy spectrum from SLG. Comparison between the energy converted ToF-PAES spectrum from SLG (black) and a calculation of the C VVV Auger spectrum from SLG (red) using equation 5.1. The calculated spectrum has been broadened using a charge particle trajectory simulation of our ToF-PAES spectrometer.

5.5 VVV Auger Efficiency

In order to determine the efficiency of the VVV Auger process in SLG, we have compared the experimental and theoretical integrated intensity ratio for the C VVV to the C KVV peaks. By taking this ratio, detector related parameters which are not dependent on the energy of the measured Auger electrons are eliminated. The resulting ratio can be written, see chap. 4, as

$$\frac{I_{\mathrm{C\ VVV}}(E)}{I_{\mathrm{C\ KVV}}(E')} = \frac{\lambda_{\mathrm{C\ V}}\, A_{\mathrm{C\ VVV}} \int_{E_1}^{E_2} P_e(E)\, f_{\mathrm{C\ VVV}}(E)\, T(E)\, \eta(E)\ \mathrm{d}E}{\lambda_{\mathrm{C\ 1s}}\, A_{\mathrm{C\ KVV}} \int_{E_3}^{E_4} P_e(E')\, f_{\mathrm{C\ KVV}}(E')\, T(E')\, \eta(E')\ \mathrm{d}E'} \tag{5.6}$$

where $\lambda_{\mathrm{C\ V}}$ and $\lambda_{\mathrm{C\ 1s}}$ are the SLG valence and 1s annihilation probabilities respectively. $\mathrm{I_{C\ VVV}}$ and $\mathrm{I_{C\ KVV}}$ are the measured integrated PAES intensities and $\mathrm{A_{C\ LVV}}$ and $\mathrm{A_{C\ KVV}}$ are the Auger efficiencies. P_e is the electron escape probability, T(E) is the transmission factor, η is the transport efficiency and f are the fractions of Auger transitions which result in Auger electrons with sufficient energy to escape the solid. Thus, by comparing the experimentally calculated intensity ratio to the theoretically calculated intensities we can estimate the efficiency of the VVV Auger process assuming that the efficiency of the C KVV Auger process is known.

We find that the measured ratio of the integrated intensities of the C VVV Auger peak and the integrated intensity of the C KVV Auger peak is 21 $\pm$ 4, where the error bar represents the statistical uncertainty in the measurement. The calculation of the C KVV Auger peak intensity was done by assuming that all annihilation-induced C 1s holes result in the emission of an Auger electron which is consistent with previous findings regarding the efficiency of K-shell Auger transitions [63]. The theoretical ratio is 20.7 which

compares quite favorably with the experimental ratio was calculated assuming a 100% efficiency for the VVV Auger transition in SLG. The calculated ratio is comparable to the experimental ratio, within experimental error, provided that the the branching ratio for the Auger decay of deep valence band holes is between 0.8 and 1.

5.6 Concluding Remarks

In conclusion, our work represents the first direct observation and investigation of the emission of low-energy electrons as a result of VVV Auger transitions. These investigations were made possible by eliminating the large, primary beam-induced secondary electron background by using matter-antimatter annihilation to initiate the Auger process. We have successfully reproduced both the experimental lineshape and the ratio of C VVV to C KVV intensities which indicates that the C VVV Auger electron emission process is highly ($>$ 80%) efficient.

Chapter 6

Auger-Mediated Positron Sticking

6.1 Introduction

In this chapter, we present and analyze measurements of positron-induced electron emission for different incident positron beam energies obtained from: highly oriented pyrolytic graphite (HOPG) and silicon. By incremental increase of the incident positron beam energy, it is possible to record spectra which are principally composed of positron annihilation-induced Auger electron emission (PAES), Auger-mediated positron sticking (AMPS), or secondary electron emission (SEE) [28, 7]. The analysis presented in this chapter has allowed the decoupling, and analysis of each component individually.

In PAES, a surface trapped positron annihilates with a surface bound electron resulting in the emission of an electron via an Auger process. This Auger process occurs when a less tightly bound electron comes to occupy

the energy level of the hole, coupling the energy associated with this filling of the hole to a third electron, which escapes into the vacuum, see chapter. These Auger processes can be initiated both by core level and valence level annihilations [13]. Importantly, the PAES intensity is determined in part by the number of surface state annihilations and does not directly depend on the incident positron beam energy, see chapter 4. The AMPS process is initiated when a positron transitions from a (positive energy) scattering state to an image-potential-induced (negative energy) surface bound state. The energy associated with this transition is coupled to a valence electron via a virtual photon providing sufficient energy to escape the material. This process is represented schematically in Fig. 6.1 for the calculated HOPG density of states. Finally, the SEE process is initiated when a positron transitions from a scattering state to a bulk state inside the material, transferring the energy associated with this transition to an electron in the solid.

The maximum kinetic energy, E_{max}^{AMPS}, of an electron emitted as a result of AMPS is given by:

$$E_{max}^{AMPS} = E_K + \varepsilon_{ss} - \phi_s^- \tag{6.1}$$

where E_K is the incident positron energy including any sample bias, ε_{ss} is the positron surface state binding energy, and ϕ_s^- is the electron work function. Therefore, a minimum incident positron energy of $\phi_s^- - \varepsilon_{ss}$ is required for the AMPS process to eject an electron. AMPS can be distinguished from a SEE process in which the final state of the positron is a bulk state instead of a surface state. The maximum kinetic energy, E_{max}^{SE}, for this secondary electron

emission process is given by:

$$E_{max}^{SE} = E_K + \phi^+ + -\phi_s^- \tag{6.2}$$

where ϕ^+ is the positron work function. Therefore, the minimum incident positron energy required for secondary electron emission is $\phi_s^- - \phi^+$.

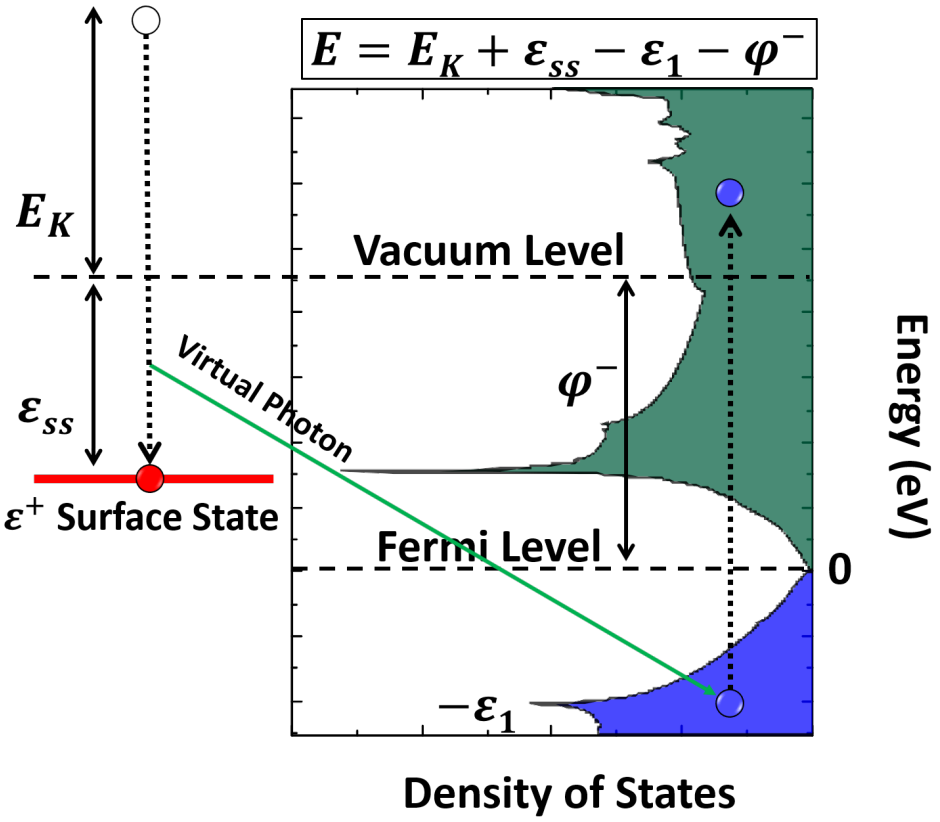

Figure 6.1: Schematic representation of the AMPS process. A positron incident with kinetic energy E_K makes a transition from a scattering state to a bound surface state with binding energy ε_{ss}. The energy associated with this transition is coupled to an electron in the valence band (blue) with energy ε_1 via a virtual photon, exciting the electron into an unoccupied state (light green). If this unoccupied state is above the vacuum level, the electron may be emitted with energy E. The calculated density of states shown is for a HOPG surface courtesy of Vincent Callewaert.

6.2 Experimental Details

The experiments presented in this chapter were performed using the University of Texas at Arlington's positron beam system described in chapter 2. The sample chamber is kept at a base pressure less than 10^{-8} Pa. The incident positron beam energy was measured to be less than 1 eV using a retarding field analyzer. The maximum energy of the incident positrons is referred to as the beam energy. The positron beam energy was varied by applying a negative bias to the sample, increasing the incident kinetic energy. The p-type Si(100) samples were sputter cleaned every 24 hours prior to measurements. The highly oriented pyrolytic graphite (HOPG) was cleaved in air before insertion into the chamber. No additional surface modifications of the HOPG sample were made after installation.

For each time-of-flight (ToF) spectra presented in this chapter were each been divided by a number proportional to the number of positrons annihilating at the sample as determined using a NaI(Tl) detector mounted near the sample. The bottom axis of each ToF spectra is the time the electrons take to travel 1m and has been reversed so that the scale goes from higher ToF (lower energy) to lower ToF (higher energy). The top axis in each ToF spectra is the corresponding kinetic energy calculated from the ToFs.

6.3 Experimental Results

Figures 6.2 and 6.3 show the measured ToF and energy spectra of positron-induced electrons emitted from HOPG and Si taken at incident positron beam energies of 1.25 eV, 1.5 eV, and 2.0 eV. Panels (a)-(c) are the ToF measurements and panels (d)-(f) are the energy-converted ToF measurements of panels (a)-(c). In each figure, the measured spectra at the indicated incident positron beam energy as displayed in black. The red spectra are constructed by shifting the 1.25 eV energy spectra of panels (d) to higher energies —to compensate for the kinetic energy electrons gain from the negative sample bias —as detailed in chapter 2. The area of the principal Auger peak (either C KVV or Si $L_{2,3}VV$) of the shifted 1.25 eV spectra was area normalized that that of the experimental spectra in black. This normalization ensures that the number of surface state annihilations is approximately the same between the compared spectra [80]. Before we discuss each individual spectra, we would like to highlight some features that all three samples share in common. As the negative sample bias is increased the low energy (high ToF) edge of the spectra is shifted by amount equal to the sample bias —which can be completely accounted for in terms of the shifted 1.25 eV spectra. When the spectra are viewed sequentially with increasing incident positron beam energy, they show the emergence and growth of the AMPS peak as more energy becomes available to probe deeper into the density of states. From a comparison between the experimentally measured spectra (black) and the shifted 1.25 eV spectra (red) it is possible to observe the onset and energy threshold of the AMPS process. However, the energy which with this onset occurs is different for each sample, and is consistent with the differences in

surface state binding energies between the three samples.

In the HOPG spectra, fig. 6.2, the peaks labelled A and B are due to the Auger decay of annihilation-induced 1s holes in carbon (C KVV) and oxygen (O KVV) respectively. The broad low-energy peak labelled C VVV is due to the Auger decay of annihilation-induced holes in the valence band of HOPG. Panel (a) was taken at an incident positron beam energy of 1.25 eV and is the composed entirely of electrons emitted as a result of these three Auger processes. Panel (f) shows that the AMPS electron emission process is underway by an incident positron beam energy of 2.0 eV. The Si spectra, fig. 6.3, exhibits peaks due to the Auger decay of annihilation-induced holes in both the 2p levels of Si (Si $L_{2,3}VV$) and the valence band (Si VVV). Here, the onset of the AMPS process is at a higher incident positron beam energy indicating a lower value for ε_{ss} for Si than HOPG.

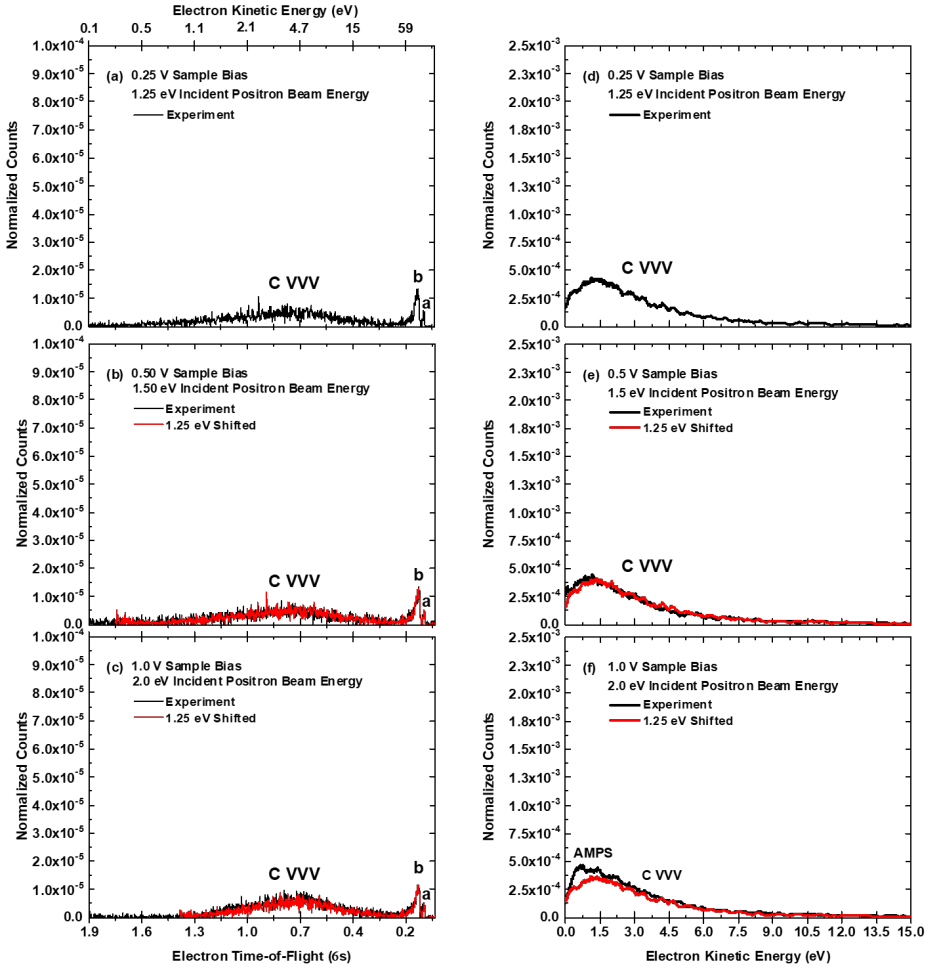

Figure 6.2: Positron-induced electron spectra obtained from HOPG for 1.25 eV, 1.5 eV, and 2.0 eV incident positron beam energies. Left panels are the ToF spectra of electrons emitted following either the Auger decay of positron annihilation-induced holes or positron sticking. The peaks labeled A and B correspond to O KVV and C KVV Auger processes respectively. Right panels are the energy-converted ToF spectra.

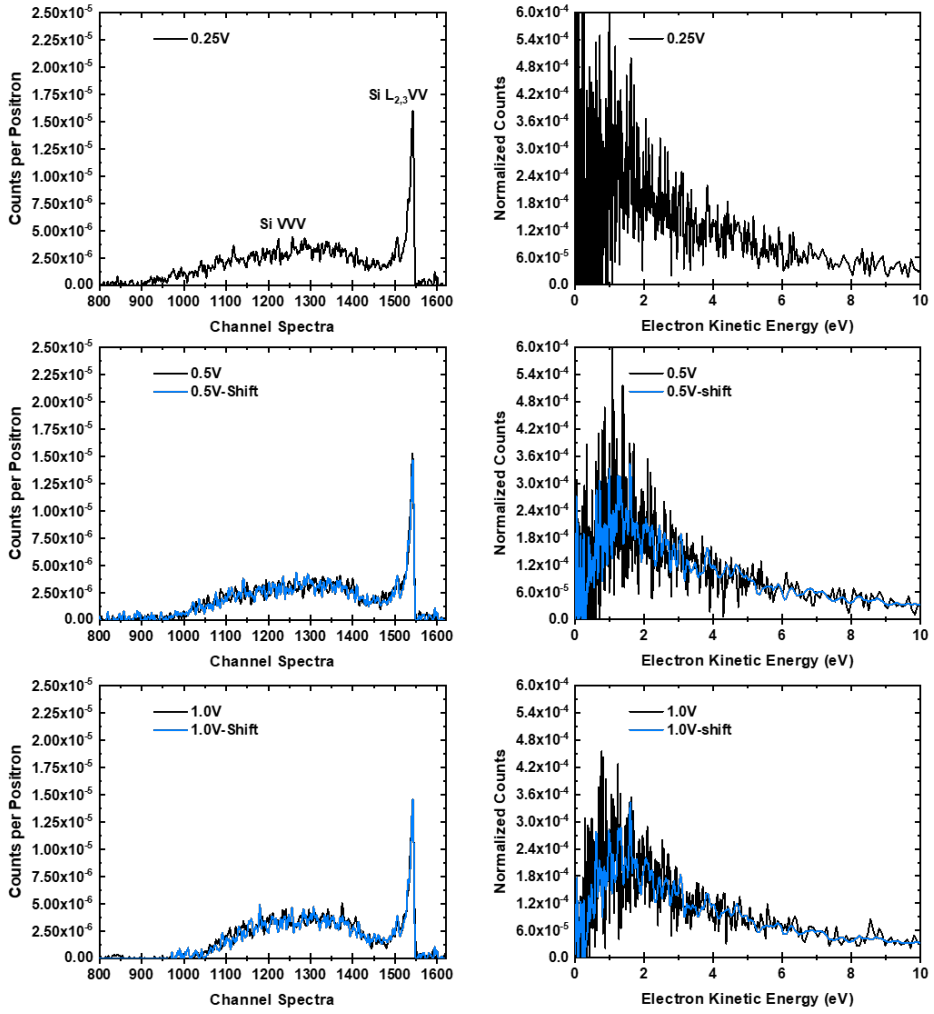

Figure 6.3: Positron-induced electron spectra obtained from Si for 1.25 eV, 1.5 eV, and 2.0 eV incident positron beam energies. Panels (a)-(c) are the ToF spectra of electrons emitted following the Auger decay of positron annihilation-induced holes. Panels (d)-(f) are the energy-converted ToF spectra of panels (a)-(c).

6.4 Theoretical AMPS Line Shape

The AMPS electron energy distribution, $A_{AMPS}(E)$, was calculated according to:

$$A_{AMPS}(E) = P_e(E)\ \rho_c(E)\ \iint \frac{\rho_v(\varepsilon_1) f(\varepsilon_p) \delta(\varepsilon_p - \varepsilon_1 - \phi_s^- - E)}{N(\varepsilon_p)}\ d\varepsilon_p\ d\varepsilon_1 \tag{6.3}$$

where E is the kinetic energy of the emitted AMPS electron, ε_1 is the binding energy of the participating electron, $\varepsilon_p = E_k + \varepsilon_{ss}$ is the positron energy in the surface state, $f(\varepsilon_p)$ is the positron beam energy distribution normalized to 1, ϕ is the energy required to remove an electron from the solid, P_e(E) is the electron escape probability detailed in chap. 4, $\rho_v(\varepsilon_1)$ is the calculated density of valence states, and $\rho_c(\varepsilon_E)$ is the calculated density of conduction states, see figure 6.1. δ is the energy conserving delta function. $N(\varepsilon_p)$ is a normalization factor counting all possible AMPS transitions i.e.

$$N(\varepsilon_p) = \iint \rho_v(\varepsilon_1)\rho_c(\varepsilon_f)\delta(\varepsilon_p - \varepsilon_1 - \phi_s^- - \varepsilon_f) d\varepsilon_1\ d\varepsilon_f \tag{6.4}$$

where ε_f is the final state binding energy. The surface state binding energies used in the calculations of the AMPS line shapes are 2.4 eV for HOPG and 2.2 eV for Si. The calculated density of states for HOPG and Si are shown in figs. 6.4 and 6.5 respectively. The resulting calculated spectra have been used as inputs to our simulated spectrometer in order to account for the instrument response function, see chap. 3.

Figure 6.6 shows the measured and modelled ToF spectra of positron-induced electrons emitted from HOPG taken at incident positron beam

energies of 2.5 eV, 3.0 eV, and 3.5 eV. The black spectra are the experimentally measured spectra. The red spectra is the estimated annihilation-induced Auger spectra (the shifted 1.25 eV spectra) while the blue peak is the modelled AMPS peak calculated using equation 6.3 with a surface state binding energy of 2.4 eV. Figure 6.7 shows the measured and modelled energy-converted spectra of positron-induced electrons from figure 6.6.

Figure 6.3 shows the measured and modelled ToF spectra of positron-induced electrons emitted from Si taken at incident positron beam energies of 2.5 eV, 3.0 eV, and 3.5 eV. The black spectra are the experimentally measured spectra. The blue spectra is the estimated annihilation-induced Auger spectra (the shifted 1.25 eV spectra) while the red peak is the modelled AMPS peak calculated using equation 6.3 and a surface state binding energy of 2.2 eV. Figure 6.8 shows the measured and modelled energy-converted spectra of positron-induced electrons from figure 6.9.

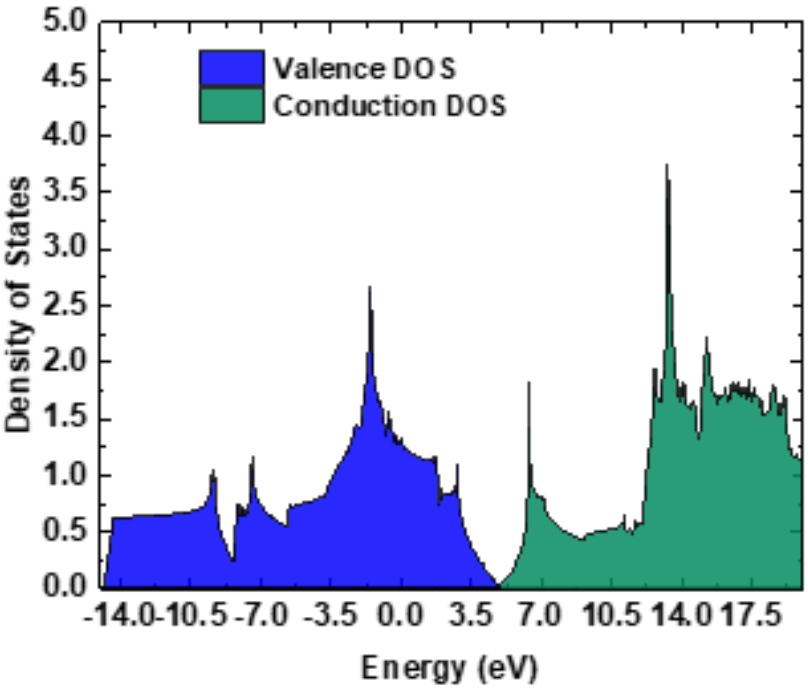

Figure 6.4: Calculated HOPG density of states.

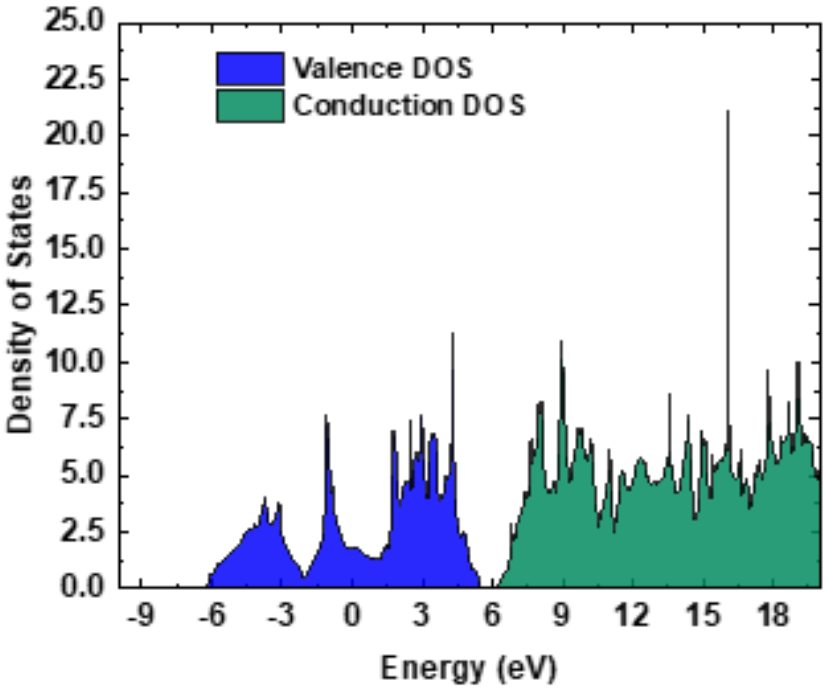

Figure 6.5: Calculated Si density of states.

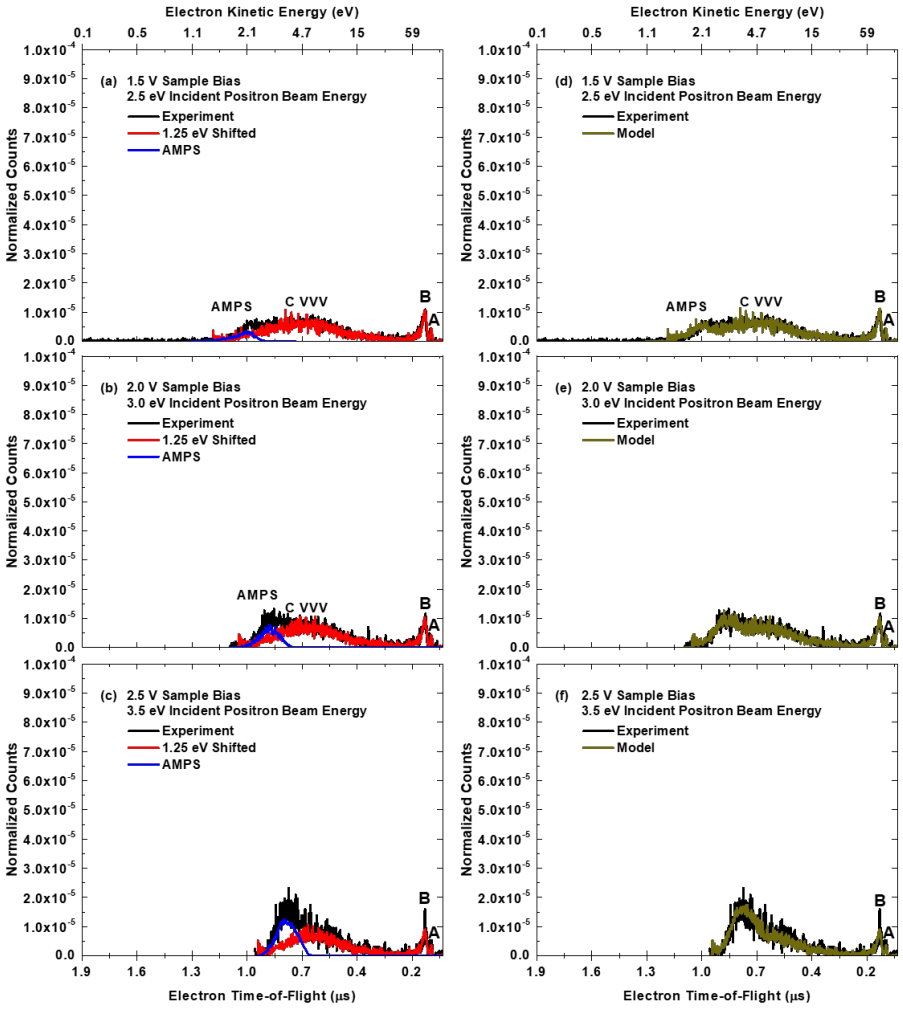

Figure 6.6: Measured and modelled positron-induced electron ToF spectra from HOPG for 2.5 eV, 3.0 eV, and 3.5 eV incident positron beam energies. Panels (a)-(c) are the ToF spectra of electrons emitted following either the Auger decay of positron annihilation-induced holes or positron sticking. The peaks labeled A and B correspond to O KVV and C KVV Auger processes respectively. Panels (d)-(f) are the summed ToF spectra of the red and blue in panels (a)-(c).

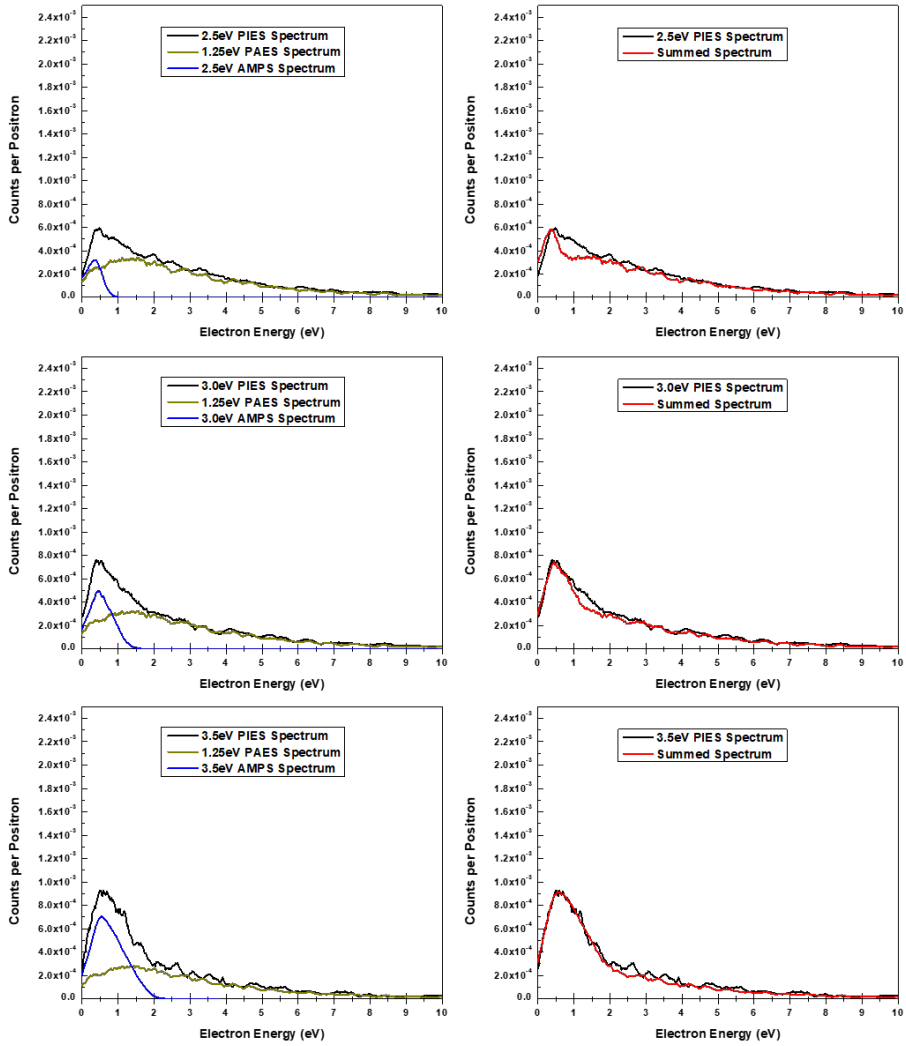

Figure 6.7: Measured and modelled positron-induced electron energy spectra from HOPG for 2.5 eV, 3.0 eV, and 3.5 eV incident positron beam energies. The left panels are the energy spectra of electrons emitted following either the Auger decay of positron annihilation-induced holes or positron sticking. The right panels are the summed ToF spectra.

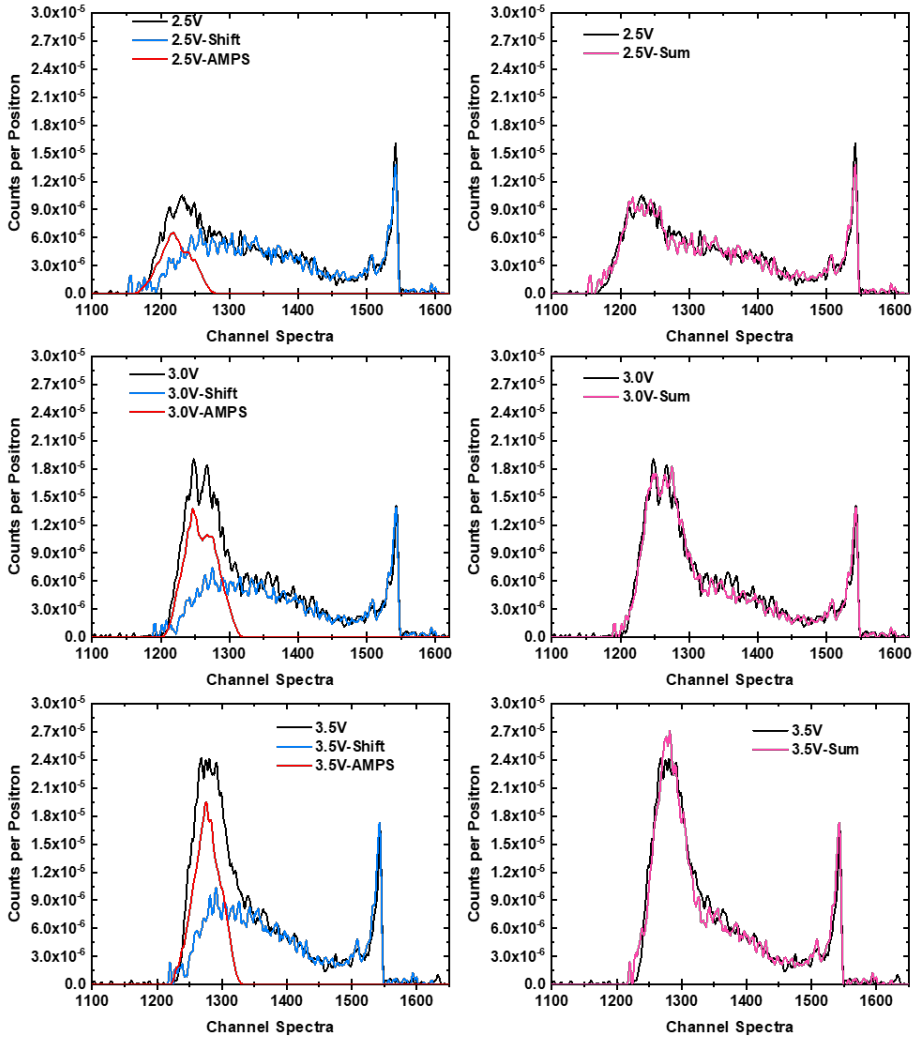

Figure 6.8: Measured and modelled positron-induced electron ToF spectra from Si for 2.5 eV, 3.0 eV, and 3.5 eV incident positron beam energies. The left panels are the ToF spectra of electrons emitted following either the Auger decay of positron annihilation-induced holes or positron sticking. The right panels are the summed ToF spectra.

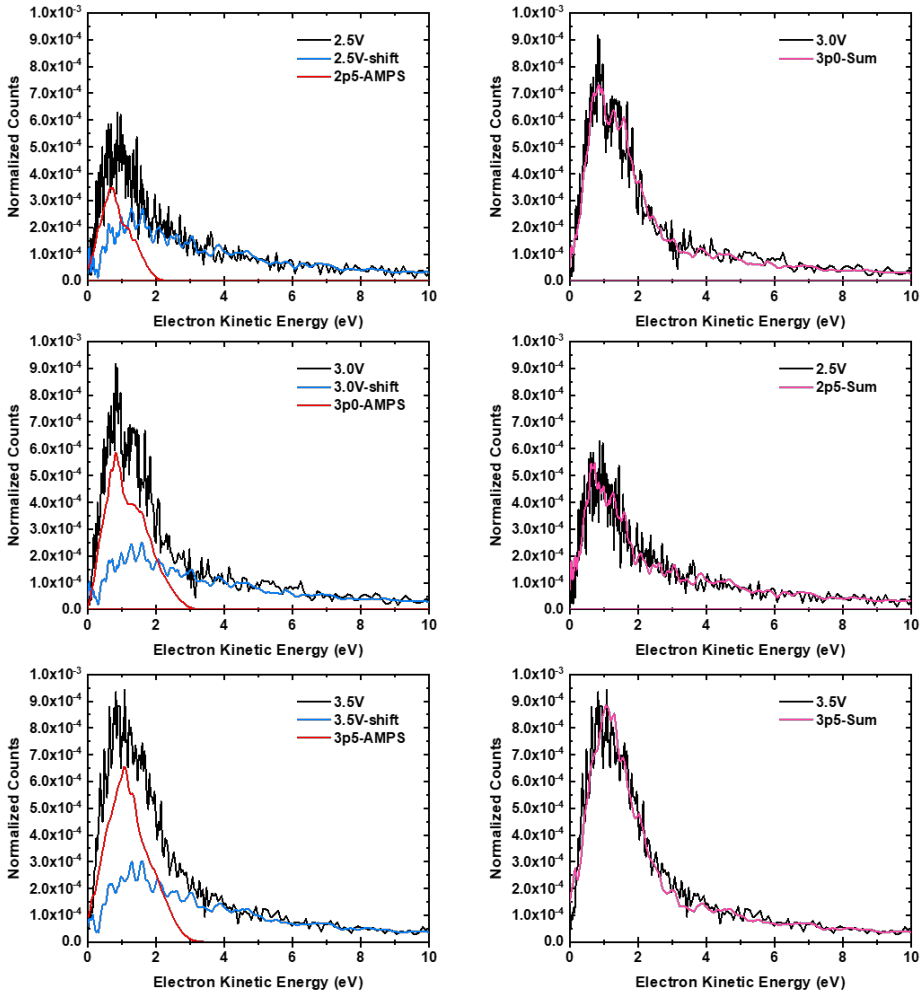

Figure 6.9: Measured and modelled positron-induced electron energy spectra from Si for 2.5 eV, 3.0 eV, and 3.5 eV incident positron beam energies. The left panels are the energy spectra of electrons emitted following either the Auger decay of positron annihilation-induced holes or positron sticking. The right panels are the summed ToF spectra.

6.5 Concluding Remarks

The time-of-flight positron-induced electron spectra presented in this chapter contain Auger peaks initiated by valence band and core level annihilations as well as peaks due to Auger mediated positron sticking (AMPS). An analysis of the spectra taken at several different positron beam energies suggests that by controlling the energy of the incident positron beam the relative contributions from Auger processes, AMPS, and secondary electron emission can be studied separately using one experimental setup. The experimental spectra were decomposed into two modelled spectra, one containing electrons emitted as a result of positron annihilation-induced Auger processes and one containing electrons emitted as a result of AMPS. The agreement between the experimental spectra and the modelled spectra provides strong confirmation that for incident positron beam energies 3.5 eV and below, the only two mechanisms for electron emission are PAES and AMPS. And, for an incident positron beam energy of 1.25 eV only Auger related processes are possible. The experimental line shapes have been understood in terms of the density of states. The modelled line shapes have allowed estimates of the positron surface state binding energy.

Chapter 7

Conclusions

In this chapter, we will summarize the results of this dissertation.

The results of measurements of the kinetic energy distributions of low-energy, positron-induced electrons emitted from single-layer of graphene (SLG), highly oriented pyrolytic graphite (HOPG), Si, Cu and TiO_2 surfaces have been presented in this dissertation.

In chapter 3 we presented numerical simulations of UTA's time-of-flight positron annihilation-induced Auger electron spectrometer (ToF-PAES). This enabled the characterization of the system's transport efficiency, timing and energy resolution, and instrument response function for the set of low-energy transport settings used in this dissertation. The simulations of the electron transport through the ToF-PAES spectrometer indicate a nearly 100% transport efficiency to the electron detector for electron energies 1 to 200 eV. The simulated relative energy resolution is less than 25% for electron energies from 1 to 1000 eV. The timing resolution was found to be 2.35 ns. The instrumental contributions to the measured electron energy spectra

predicted by these numerical simulations have made possible the detailed comparison of experimentally measured and theoretically generated spectra.

In chapter 4 we presented direct evidence of a hitherto unexplored O LVV Auger transition occurring at oxygen-exposed Cu and Si surfaces and a TiO_2 surface. We constructed an empirical O LVV line shape model which consisted of the convolution of the O KVV Auger peak line shape and the O 2s photoemission line and which provided compelling evidence that a significant number of O LVV Auger transitions result in electrons with sufficient kinetic energy to overcome the surface dipole barrier and escape into the vacuum. We calculated theoretically the O LVV electron energy distribution from TiO_2 using a first principals based model which incorporates the self-convolution of the density of states, an estimate of the distribution of annihilation-induced O 2s holes, and an estimate of the electron escape function. We found excellent agreement between the measured O LVV Auger spectrum from the TiO_2 surface and this calculation. We estimated the positron annihilation probability with the oxygen 2s levels at the surface of TiO_2 using the measured O LVV and O KVV integrated PAES intensities and calculated them theoretically. The agreement between our measured and theoretical ratio supports the idea that O LVV Auger processes are highly efficient.

In chapter 5 we presented the first direct observation and investigations of Auger processes occurring entirely within the valence band of single-layer graphene (SLG). We calculated theoretically the C VVV electron energy distribution from SLG using a first principals based model which incorporates the self-convolution of the density of states, the distribution of annihilation-

induced O 2s holes, and an estimate of the electron escape function. We found excellent agreement between the measured C VVV Auger spectrum and this calculation. We estimated the efficiency of the C VVV Auger process to be between 0.8 and 1 by comparing a theoretical calculation of the ratio of the C VVV to C KVV integrated intensities to the measured ratio.

Finally, in chapter 6 presented measurements and modelling of the Auger-mediated positron sticking (AMPS) line shapes from HOPG and Si. The experimental spectra were decomposed into two modelled spectra, one containing electrons emitted as a result of positron annihilation-induced Auger processes and one containing electrons emitted as a result of AMPS processes. The AMPS line shapes have been understood in terms of the density of states, the positron beam kinetic energy distribution, and the electron escape function. The modelled AMPS line shapes have provided estimates of the positron surface state binding energies and suggests that a more detailed analysis may provide the basis for a novel, top-layer selective positron-induced electron spectroscopy.

Appendix

A. Simulation Scripts

A.I. SIMION Gem Script

Below is the SIMION script used to generate the geometries used in the simulations of the ToF-PAES apparatus in this dissertation. Please note that lines starting with ";" are comments.

```
;This geometry file contains a basic SH beamline from
   the MCP to the sample.


pa_define(200,200,1415,planar,non-mirrored,e)
;defines the potential array size and type
locate(99,99,20)
;defines the sample assembly
{
e(1)
{       fill{within{cylinder(,,31,9,9,2)}}
;sample mount
```

```
fill{within{cylinder(,,34,5,5,2)}}
;sample
}
}

locate(99,99)
;defines tof tube
{
e(2)
{fill
{       within{cylinder(,,730,19,19,597)}
        notin{cylinder(,,730,16,16,597)}
}
}
}

e(0)
;defines the vacuum chamber
{
fill
{
within{cylinder(99,99,727,25,25,727)}
;defines the 2inch pipe housing the tof tube and sample
notin{cylinder(99,99,730,22,22,727)}
within{cylinder(99,99,1414,76,76,686)}
```

```
;defines the 6inch pipe housing the MCP and ExB plates
notin{cylinder(99,99,1411,73,73,680)}
}
}

locate(86,54,10)
;defines the ExB plates D
{
e(3){fill{within{corner_box3d(,,745,1,89,267)}}}
          ;defines west plate (positive)
e(4){fill{within{corner_box3d(25,,745,1,89,267)}}}
         ;defines east plate (negative)
}

locate(99,116,1046)      ;defines the MCP assembly with
   bottom of active MCP plate to be at (99,94,1044)
{
e(0)
;defines the MCP box
{
fill
{
within{corner_box3d(-35,-39,,70,79,1)}
;defines MCP box front plate with center @ (99,99) w/
   dimensions (70,79,1)mm
```

```
notin{corner_box3d(-10,-22,,20,43,1)}
;defines the thru slot in the MCP box front plate @
   (99,99) w/dimensions (20,43,1)mm
within{corner_box3d(-35,-39,20,70,79,3)}
;defines MCP box back plate with center @ (99,99) w/
   dimensions (70,79,3)mm. 19mm away from the front
   plate
within{corner_box3d(-35,39,2,70,1,17)}
;defines the top plate with dimensions (70,1,17)mm.
within{corner_box3d(-35,-39,2,70,1,17)}
;defines the bottom plate with dimensions (70,1,17)mm.
within{corner_box3d(-36,-39,,1,79,23)}
;defines west side plate
within{corner_box3d(36,-39,,1,79,23)}
;defines east side plate
}
}
e(5)
;defines the MCP active plate
{
fill{within{cylinder(,-1,8,32,32,2)}
;defines the MCP plate nonactive portion as circle
   radius (32,32)mm and length 2mm
notin{cylinder(,-1,6,21,21,1)}
```

```
;defines the MCP active portion as circle with radius
   (21,21)mm and length 1mm
}}
e(6){fill{within{cylinder(,-1,10,32,32,1)}}}
;defines the middle plate as circle with radius (32,32)
   mm and length 1mm
e(7){fill{within{cylinder(,-1,13,22,22,1)}}}
;defines the anode back plate as circle with radius
   (22,22)mm and length 1mm
}

locate(86,54,10)
;defines the ExB plates C
{
e(8){fill{within{corner_box3d(,,1083,1,89,267)}}}
;defines west plate (negative)
e(9){fill{within{corner_box3d(25,,1083,1,89,267)}}}
;defines east plate (positive)
}
```

A.II. SIMION Lua Script

Below is the Lua script used to generate the magic field gradients used in the simulations of the ToF-PAES apparatus in this dissertation. Please note that lines starting with "—" (double hyphen) are comments.

```
-- The workbench must contain an empty magnetic PA
   instance in which to apply this magnetic field. The
   size should be 200x200y1600z.
-- The magnetic field direction is along the beam axis(
   z) from source to sample.

simion.workbench_program()
--local TP = simion.import 'testplanelib.lua'
--local test1 = TP(20,0,0, 1,0,0)
--local test2 = TP(40,0,0, 1,-1,0)
--local test3 = TP(80,0,0, 1,1,0)

local MField = require "simionx.MField"
--These values below produce an ~45 constant Gauss B
   field along the ToF tube (99,99,133) to (99,99,730)
   which varies only by about 2 gauss from max to min
   values
local i1 = 18
local n1 = 285
local r1 = 100
local start1 = 1599
local stop1 = 0
--These values below produce a ~2196 Gauss B field at
   (99,99,38)-sample magnet in the presence of the
   above values and ~467 Gauss B field at (99,99,54) at
```

```
    the sample surface (12.5 amps i2 for 450 and 50 for
    1800)
local i2 = 12.5
local n2 = 400
local r2 = 13
local start2 = 38
local stop2 = 32

--transver(y) pushes positrons toward bottom of chamber
local i3 = .5
local n3 = 100
local r3 = 800
local start3 = 199
local stop3 = 0

--transverse(x) pushes positrons toward west for
   experiment in SH ( or into the screen looking at z-y
    plane)
local i4 = .5
local n4 = 100
local r4 = 800
local start4 = 199
local stop4 = 0
```

```
-- Defined solenoid magnetic field.
local field = MField.combined_field
{
--axial fields
        MField.solenoid_hoops
        {
        current = i1,
        first   = MField.vector(99,99,start1),
        last    = MField.vector(99,99,stop1),
        radius  = r1,
        nturns  = n1
        },
--transverse fields (y)
        --MField.solenoid_hoops
        --{
        --current = i3,
        --first   = MField.vector(99,start3,800),
        --last    = MField.vector(99,stop3,800),
        --radius  = r3,
        --nturns  = n3
        --},
        --transverse fields (x)
        --MField.solenoid_hoops
        --{
        --current = i4,
```

```
        --first    = MField.vector(start4,99,800),
        --last     = MField.vector(stop4,99,800),
        --radius   = r4,
        --nturns   = n4
        --},
--magnet at sample
        MField.solenoid_hoops
        {
        current = i2,
        first    = MField.vector(99,99,start2),
        last     = MField.vector(99,99,stop2),
        radius   = r2,
        nturns   = n2
        }
}


--prints to the output file the solenoid parameters and
    electrode voltages
print("Axial Field(z): I = " .. i1 .. " AMPS, starts at
    z = " .. start1 .. ", stops at x = " .. stop1 .. "
   with radius " .. r1 .. " mm and has " .. n1 .. "
   turns.")
print("Sample Magnet: I = " .. i2 .. " AMPS, starts at
   z = " .. start2 .. ", stops at x = " .. stop2 .. "
```

```
    with radius " .. r2 .. " mm and has " .. n2 .. "
    turns.")
--print("Transverse(y) Field: I = " .. i3 .. " AMPS,
    starts at z = " .. start3 .. ", stops at x = " ..
    stop3 .. " with radius " .. r3 .. " mm and has " ..
    n3 .. " turns.")
--print("Transverse(x) Field: I = " .. i4 .. " AMPS,
    starts at z = " .. start4 .. ", stops at x = " ..
    stop4 .. " with radius " .. r4 .. " mm and has " ..
    n4 .. " turns.")
function segment.init_p_values()
for i=1, 9 do print("Electrode " .. i .. " is at: " ..
    adj_elect[i] .. "V")
end
end

-- Override magnetic field in magnetic PA instances
    with that in the field object.
function segment.mfield_adjust()
ion_bfieldx_gu, ion_bfieldy_gu, ion_bfieldz_gu = field(
    ion_px_mm, ion_py_mm, ion_pz_mm)
end
```

A.III. Perl SIMION File Analysis Script

Below is the Perl script used to analyze the output files of the SIMION simulations. Please note that lines starting with "#" are comments.

```
#SIMION.pl -
#       Extracts data from SIMION data files.
#       Gives the channelspectra of the initial
   distribution flown in SIMION.
#       Gives the per energy, per channel number
   frequency counts.
#       Gives transport efficiency per initial energy.
#       Gives all initial data for splats at detector
use strict;
use warnings;
use List::Util qw( min max );



#User inputs - File information
my $fileextension = ".dat";
my $directory = "SIMION Files/Si IRF/500/";
#Folder containing the files to analyze
#my $directory = "SIMION-Varghese/";
#Folder containing the files to analyze
my $particlesperbin = 500;
#Number of particles flown per energy bin
```

```
#User inputs - SIMION file specifics
my $TAC = 4;
#TAC setting in microseconds
my $channels = 2048;
#MCA number of channels.
my $linestart = 25;
#First non-header line in SIMION datafile
my $ToFcolumn = 2;
#Column in SIMION datafile for ToF data
my $splatcoordinatecolumn = 5;
#Column in SIMION datafile for splat coordinate (X, Y,
    or Z)
my $KEcolumn = 25;
#Column in SIMION datafile for KE data
my $splatlocation = 1053;
#Value for MCP splat location#User inputs - SIMION file
     specifics

#User inputs - Varghese
# my $TAC = 5.25;
#TAC setting in microseconds
# my $channels = 1000;
#MCA number of channels.
# my $splatlocation = 3624;
```

```
#Value for MCP splat location
# my $linestart = 13;
#First non-header line in SIMION datafile
# my $ToFcolumn = 1;
#Column in SIMION datafile for ToF data
# my $splatcoordinatecolumn = 6;
#Column in SIMION datafile for splat coordinate (X, Y,
    or Z)
# my $KEcolumn = 26;
#Column in SIMION datafile for KE data



#Grab filenames
opendir my $dir, $directory or die "Cannot open
    $directory: $!";
my @read = readdir($dir);
my @filenames = grep {/$fileextension$/i} @read;
closedir $dir;

#Prompt user for files to analyze
print "Type the numbers of the files to analyze comma
    delimited.","\n";
```

```
for(my $i = 0; $i < scalar(@filenames); $i++){print
    join("\t",($i) . ".",$filenames[$i],"\n");}
chomp(my $usrinputs = <STDIN>);
my @usrinputs = split(/\s*,\s*/, $usrinputs);
for(my $i = 0; $i < scalar(@usrinputs); $i++){  print "
    you selected " . $filenames[$usrinputs[$i]],"\n";
            }
print "Is this correct? Type y for yes.","\n";
chomp(my $pause = <STDIN>);


if($pause eq "y"){
####Begin SIMIONExtraction code####
for(my $m = 0; $m < scalar(@usrinputs); $m++){

#Extract SIMION particle number, ToF, splat location,
    initial KE, and initial KE error
#Find and associate splats initial kinetic energy
my (@splats,@temp,@fulldata,@headers,@splatloss);
my $j = 0;
my $i = 0;
my $datafile = $filenames[$usrinputs[$m]];
$datafile =~ s/$fileextension//g;
my $file = $directory . $datafile . "$fileextension";
open(DATA, '<', $file) or die "Can't open $file: $!";
```

```
while(my $line = <DATA>){
        if($. == $linestart - 2){
                chomp $line;
                @headers = split(/       /,$line);
        }
        next if $. < $linestart;
        chomp $line;
        my @rows = split(/       /,$line);
        for(my $n = 0; $n < scalar(@rows); $n++){
                  $temp[$j][$n] = $rows[$n];
                   }
        if($j != 0 && $temp[$j-1][0] =~ m/$temp[$j][0]/
            && $rows[$splatcoordinatecolumn] =~ m/^
            $splatlocation$/ && $rows[$ToFcolumn] <=
           $TAC){
                $splats[$i][0] = $temp[$j-1][0];
                $splats[$i][1] = int(($TAC-$rows[
                   $ToFcolumn])/($TAC/$channels));
                $splats[$i][2] = $temp[$j-1][$KEcolumn
                   ];
                for(my $n = 0; $n < scalar(@rows); $n
                   ++){
                        if($n == $ToFcolumn){
                           $fulldata[$i][$n] = $rows[
                           $ToFcolumn];   }
```

```
                        if($n != $ToFcolumn){
                            $fulldata[$i][$n] = $temp[$j
                            -1][$n];     }
                    }
                    $i++;
            }
            $j++;
}
close DATA;

#Box channel spectra
my %BOXchannelspectra;
my @chans = map $_ -> [1], @splats;
for (@chans) {  $BOXchannelspectra{$_}++;        }
my $BoxchannelMin = min keys %BOXchannelspectra;
my $BoxchannelMax = max keys %BOXchannelspectra;
for(my $k = $BoxchannelMin; $k <= $BoxchannelMax; $k++)
   {
        if(     !exists($BOXchannelspectra{$k}) ){
                $BOXchannelspectra{$k} = 0;      }
}
#Prints %BOXchannelspectra
my $BOXchannelspectraprint = $directory . $datafile .
   "_BOXchannelspectra.txt";
```

```
open (BOXchannelspectra, ">>", $BOXchannelspectraprint)
    or die "Can't open $BOXchannelspectraprint: $!";
for my $ee (sort{$a <=> $b} keys %BOXchannelspectra){
   print BOXchannelspectra join("\t", $ee,
   $BOXchannelspectra{$ee},"\n");}
close BOXchannelspectra;


#Builds hash %SORTEDchannelspectra: per energy, per
   channel number frequency counts.
#Computes Transport Efficiency for each initial energy
   Bin
my @initialKE = map $_ -> [2], @splats;
@initialKE = get_unique(@initialKE);
@initialKE = sort {$a <=> $b } @initialKE;
my (%SORTEDchannelspectra,@transport);
for(my $y = 0; $y < scalar(@initialKE); $y++){
my $KE = $initialKE[$y];
my $transportcount = 0;

for(my $z = 0; $z < scalar(@splats); $z++){
        if($splats[$z][2] =~ m/^$KE$/){
                $SORTEDchannelspectra{$KE}{$splats[$z
                   ][1]}++;
                $transportcount++;
```

```
        }
}

my $SORTEDchannelMin = min keys %{$SORTEDchannelspectra
    {$KE}};
my $SORTEDchannelMax = max keys %{$SORTEDchannelspectra
    {$KE}};
for(my $k = $SORTEDchannelMin; $k <= $SORTEDchannelMax;
     $k++){
        if(      !exists($SORTEDchannelspectra{$KE}{$k})
            ){      $SORTEDchannelspectra{$KE}{$k} = 0;
                }
}
$transport[$y][0] = $KE;
$transport[$y][1] = ($transportcount/$particlesperbin)
    *100;
}




#Prints %SORTEDchannelspectra
my $SORTEDchannelspectraprint = $directory . $datafile
    . "_SORTEDchannelspectra.txt";
```

```
open (SORTEDchannelspectra, ">>",
   $SORTEDchannelspectraprint) or die "Can't open
   $SORTEDchannelspectraprint: $!";
for my $KEkeys (sort {$a <=> $b} keys %
   SORTEDchannelspectra) {
for my $chanKEYS (sort {$a <=> $b} keys %{
   $SORTEDchannelspectra{$KEkeys}})
{       print SORTEDchannelspectra join("\t", $KEkeys,
   $chanKEYS, $SORTEDchannelspectra{$KEkeys}{$chanKEYS
   },"\n");       }
}
close SORTEDchannelspectra;
#prints @transport
my $transportprint = $directory . $datafile . "
   _transportefficiency.txt";
open (TRANSPORT, ">>", $transportprint) or die "Can't
   open $transportprint: $!";
for(@transport){        print TRANSPORT join("\t",@$_
   ,"\n");     }
close TRANSPORT;
#prints @fulldata
my $fulldataprint = $directory . $datafile . "
   _fullsplatdata.txt";
open (FULLDATA, ">>", $fulldataprint) or die "Can't
   open $fulldataprint: $!";
```

```
for(@headers){  print FULLDATA $_,"\t"; }
print FULLDATA "\n";
for(@fulldata){ print FULLDATA join("\t",@$_,"\n");
        }
close FULLDATA;
        }
}
else{exit;}


#Prints runtime to command line
my $runtime = time() - $^T;
print "It took " . $runtime/60 . " minutes.", "\n";



####subroutines####
sub get_unique {
        #deletes duplicate entries in array
    my %seen;
    grep !$seen{$_}++, @_;
}
```

A.IV. Perl IRF Script

Below is the Perl script used to apply the instrument response function to a theoretical positron-induced electron kinetic energy distribution. Please note that lines starting with "#" are comments.

```
#IRF.pl -
#       Interpolates/Bins input function to SIMION file
#       Weights SIMION file by input function
#       Convolves with timing gaussian
#       Energy converts/smoothens
use strict;
use warnings;
use Math::Gauss ':all';
use List::Util qw(sum);
use Math::Round;
use Math::Expression::Evaluator;
use Math::Derivative qw(Derivative1 Derivative2);



my $inputfxnfile = "TiO2_DOS-auger";
#my $inputfxnfile = "3p5_Cu_AMPSTHY_Flat";
my $inputfxnfilelinestart = 1; #4 AMPS; 1 Varghese VVV
my $inputfxncolm = 3; #1 AMPS; 3 Varghese VVV;
#my $inputfxnfile = "SLG-auger";
#my $inputfxnfile = "Auger_Cu111_Graphene_int";
my $outputfile = $inputfxnfile . "_IRF.txt";
```

```
#my $SIMdatafile = "SIMION Files/Cu IRF/500/0
    p5_VVVuniform_SORTEDchannelspectra.txt";
#output of SIMIONExtraction.pl
my $SIMdatafile = "SIMION Files/Si IRF/500/0
    p5_VVVuniform_SORTEDchannelspectra.txt";
#output of SIMIONExtraction.pl
#my $SIMdatafile = "SIMION Files/Cu IRF/500/3
    p5_uniform_SORTEDchannelspectra.txt";
#output of SIMIONExtraction.pl
my $samplebias = 0;
my $channelshift = 0; #Amount of channels to add before
     energy conversion
my $SIMparts = 500; #NB(e1)

#Gaussian timing parameters for SH
my $TAC = 4;
#TAC setting in microseconds
my $MCA = 2048;
#MCA number of channels.
my $sigma = 1*($MCA/($TAC*1000));
#Sigma value for timing resolution gaussian convolution
     (in Channels)
my $expectedvalue = 0;
#Expected value for timing resolution gaussian
    convolution
```

```
my $gaussstart = -3;
#X value to start Gaussian
my $gaussstop = 3;
#X value to end Gaussianmy

#Gaussian timing parameters for CPB
#my $TAC = 5.25;
#TAC setting in microseconds
#my $MCA = 1000;
#MCA number of channels.
#my $sigma = 9.34*($MCA/($TAC*1000));
#Sigma value for timing resolution gaussian convolution
    (in Channels)
#my $expectedvalue = 0;
#Expected value for timing resolution gaussian
   convolution
#my $gaussstart = -3;
#X value to start Gaussian
#my $gaussstop = 3;
#X value to end Gaussian



###Energy Calibrations###
```

```
my $m = Math::Expression::Evaluator->new;
#Si Settings 0 eV centers
$m->parse("(2.9991583152336307-0.0017764754531381633*x
    +2.0687344012601424*10^-7*x
    ^2-1.2270619870079605*10^-10*x
    ^3+8.032219239070823*10^-14*x
    ^4-1.6326534943973247*10^-17*x^5) ");

#Cu Experimental
#$m->parse("(60.863434308164-0.214658324681717*x
    +0.00031119480889550 8*x^2-2.27676724707788*10^-7*x
    ^3+8.33930743703305*10^-11*x
    ^4-1.22122881618327*10^-14*x^5) ");
#my $infinity = 1579;
#Simulated Energy Calibration for Cu simion settings
    used in Nature Comm paper
#$m->parse("(6.29994-0.0112773*x+8.22468*10^-6*x
    ^2-1.79226*10^-9*x^3-5.52773*10^-13*x
    ^4+2.06028*10^-16*x^5)");
#Simulated Energy Calibration for Cu SIMION settings
    from lowest channel 0 eV electrons
#$m->parse("(13.684092767091446-0.03986006101638812*x
    +0.000050190030304759 47*x^2-3.142553490610388*10^-8*
    x^3+9.598777552744021*10^-12*x
    ^4-1.1514291709602613*10^-15*x^5)");
```

```
#Simulated Energy Calibration for Cu simion settings
    from HOPG edge fits
#$m->parse("(-54.245905030714624+0.16418305261245694*x
    -0.0001925075303103033*x^2+1.1168519985286492*10^-7*
    x^3-3.228348369725917*10^-11*x
    ^4+3.7192876864812474*10^-15*x^5)");
#$m->parse("(2.042806400658199-0.0007870087978207716*x
    -1.0402983828121191*10^-7*x^2)");
#Varghese CPB-center 0eV
#$m->parse("(3.12625*10^-5+0.00476*x-1.41212*10^-5*x
    ^2+1.76784*10^-8*x^3-1.11221*10^-11*x
    ^4+2.80377*10^-15*x^5)");



###Code Begins###
#Import sorted simion channel spectra: SB_e1(#1)
my (%SIM,%SIMWeighted,@SIMEnergies,$SIMstepsize,
    $SIMLastEnergy,$SIMIndex);
open(SIM, '<', $SIMdatafile) or die "Can't open
    $SIMdatafile: $!";
while(my $line = <SIM>)
{
```

```
chomp $line;
my @rows = split(/       /,$line);
$SIM{$rows[0]}{$rows[1]} = $rows[2];
}
close SIM;
for my $keys (sort { $a <=> $b } keys %SIM){      push(
   @SIMEnergies,$keys);       }
$SIMstepsize = $SIMEnergies[1]/2;
$SIMLastEnergy = $SIMEnergies[-1];
$SIMIndex = $SIMLastEnergy / (2*$SIMstepsize);

#Import inputfxn
my (%INPUT,@INPUTEnergies,@INPUTCounts,%INPUTBinned);
      #INPUTBinned NT(e1)
my $inputfxnfile2 = $inputfxnfile . ".txt";
open(IN, "<", $inputfxnfile2) or die "Can't open
   $inputfxnfile2: $!";
while(my $line =<IN>){
next if $. < $inputfxnfilelinestart;
chomp $line;
my @rows = split(/       /,$line);
$INPUT{$rows[0]} = $rows[$inputfxncolm];
}
close IN;
```

```
#Interpolate to SIM bin edges and integrate for SIM bin
    centers
my $k = 0;
my $j = $SIMLastEnergy + 2*$SIMstepsize;
while($k < $j){
$k += $SIMstepsize;
if(!defined $INPUT{$k}){          $INPUT{$k} = 0; }
}
for my $keys (sort { $a <=> $b } keys %INPUT){
push(@INPUTEnergies,$keys);
push(@INPUTCounts,$INPUT{$keys});
}
for(my $i = 1; $i < scalar(@INPUTEnergies)-1; $i++){
if($INPUTCounts[$i] == 0){
        $INPUTCounts[$i] = $INPUTCounts[$i-1]+(
            $INPUTEnergies[$i]-$INPUTEnergies[$i-1])*(
            $INPUTCounts[$i+1]-$INPUTCounts[$i-1])/(
            $INPUTEnergies[$i+1]-$INPUTEnergies[$i-1]);
}
}

my $temp = 0;
my $tempint = 0;
for(my $i = 0; $i <= $SIMIndex; $i++){
```

```
my $binedge = $i*2*$SIMstepsize+$SIMstepsize;
my $bincenter = $i*2*$SIMstepsize;
while($INPUTEnergies[$i+$temp] < $binedge){
        $tempint += .5*($INPUTEnergies[$i+1+$temp]-
           $INPUTEnergies[$i+$temp])*($INPUTCounts[$i+
           $temp]+$INPUTCounts[$i+1+$temp]);
        $temp++;
}
$temp = $temp-1;
$INPUTBinned{$bincenter} = $tempint;
$tempint = 0;
}


#Multiplication ST_e1(#1) = SB_e1(#1)*(NT(e1)/NB(e1))
   and Sum to create Weighted Channel Spectra
for my $KEkeys (sort{$a <=> $b} keys %SIM)
{
for my $CHANkeys (sort{$a <=> $b} keys %{ $SIM{$KEkeys}
    })
{$SIMWeighted{$CHANkeys} += $SIM{$KEkeys}{$CHANkeys}*
   $INPUTBinned{$KEkeys}/$SIMparts;}
}
```

```
##Timing Convolution##
#Generate Gauss timing function
my @gaussfxn;
my $gaussindex = 0;
for(my $x = $gaussstart; $x <= $gaussstop; $x++){
$gaussfxn[$gaussindex][0]  = $x;
$gaussfxn[$gaussindex][1]  = pdf($x,$expectedvalue,
   $sigma);
$gaussindex++;
}

#list convolve with Gaussian, recover x values and
   normalize to input %SIMWeighted
my (@Chans, @Vals);
for my $CHANkeys (sort{$a <=> $b} keys %SIMWeighted){
push(@Chans,$CHANkeys);
push(@Vals,$SIMWeighted{$CHANkeys});
}
my @list1 = map $_ -> [1], @gaussfxn;
my @list2 = @Vals;
my @reverselist2 = reverse @list2;
my (@ChannelConvolutionXvalues,
   @ChannelConvolutionYvalues);
```

```
my $count = 0;
for(my $i = 0; $i < (scalar(@list2)+scalar(@list1)-1);
    $i++){
if($i >= scalar(@list1)){$count++;}
push(@ChannelConvolutionYvalues,ListConvolve($i-$count,
    $i+1));
}

sub ListConvolve {
my $index1 = shift;
my $index2 = shift;
if($index1 < 0 or ($index1-$index2 < -scalar(@list2))){
    return 0;}
else{return $list1[$index1]*$reverselist2[$index1-
    $index2]+ListConvolve($index1-1,$index2)}
}
my $Convolutiontotal = sum @ChannelConvolutionYvalues;
my $Weightedchannelspectratotal = sum @list2;
for(@ChannelConvolutionYvalues){$_ = $_*(
    $Weightedchannelspectratotal/$Convolutiontotal);}
push(@ChannelConvolutionXvalues,$Chans[-1]);
for(my $i = 1; $i <= scalar(@ChannelConvolutionYvalues)
    -4; $i++){        unshift(@ChannelConvolutionXvalues,
    $Chans[-1]-$i);        }
```

```
for(my $i = 1; $i < 4; $i++){    push(
    @ChannelConvolutionXvalues,$Chans[-1]+$i); }

#Energy conversion and Smoothening
my $deltaE = 0.25;
my @ChannelConvolutionXvaluesSHIFTED;
for(my $i = 0; $i < scalar(@ChannelConvolutionXvalues);
    $i++){$ChannelConvolutionXvaluesSHIFTED[$i] =
    $ChannelConvolutionXvalues[$i] + $channelshift}
my ($energyoutref, $energycountsoutref) = EnergyConv(\
    @ChannelConvolutionXvaluesSHIFTED,\
    @ChannelConvolutionYvalues,$samplebias);
#my ($energyoutref, $energycountsoutref) = EnergyConv(\
    @ChannelConvolutionXvalues,\
    @ChannelConvolutionYvalues,$samplebias);
#my $Smoothenoutref = Smoothen(\@$energyoutref,\
    @$energycountsoutref);



#Print output file
open(OUT, ">>", $outputfile) or die "Can't open:
    $outputfile $!";
# for my $chanKEYS (sort {$a <=> $b} keys %INPUTBinned)
# {      print OUT join("\t", $chanKEYS, $INPUTBinned{
    $chanKEYS},"\n");  }
```

```
print OUT join("\t","Channel:  " . $channelshift, "
    Counts", "Energy (eV): " . $samplebias . " eV","
    Counts","\n");
for(my $i = 0 ;$i < scalar(@$energyoutref); $i++){
print OUT join("\t", $ChannelConvolutionXvaluesSHIFTED[
    $i],$ChannelConvolutionYvalues[$i],@$energyoutref[$i
    ],@$energycountsoutref[$i],"\n");
}
close OUT;


#Prints runtime to command line
my $runtime = time() - $^T;
print "It took " . $runtime . " Seconds.", "\n";


sub EnergyConv {
##ToF-Energy conversion
#Requires Math::Expression::Evaluator;
my $channelsref = shift;
my $channelcountsref = shift;
my $samplebias = shift;
my @channels = @$channelsref;
my @channelcounts = @$channelcountsref;
my (@y,@energy,@ecounts);
```

```
for(my $i = 0; $i < scalar(@channels); $i++)
{
my $chan = $channels[$i];
$y[$i] = $m -> val({x => $chan});
}
my @dydx = Derivative1(\@channels,\@y);
for(my $i = 0; $i < scalar(@channels); $i++)
{
$energy[$i] = (1/($y[$i]**2))-$samplebias;
$ecounts[$i] = $channelcounts[$i]*(-1/2)*($y[$i]**3)
   *(1/$dydx[$i]);
}
return(\@energy,\@ecounts);
}

sub Smoothen {
##Moving average energy smoothening
my $energiesref = shift;
my $ecountsref = shift;
my @energies = @$energiesref;
my @ecounts = @$ecountsref;
my $p = 0;
my $q = 0;
my @smoothened;
```

```
if(!defined $deltaE ){my $deltaE = 0.25;}

#while($energies[$p] < 5000)
while($p < scalar(@energies)-2)
{
$q = $p;
my $totalNE = 0;
my $averageNE = 0;
my $number = 0;
while($energies[$q] < $energies[$p]+$deltaE)
{       #last if $q == 1367;
        $totalNE += $ecounts[$q];
        $q++;
        $number++;
        #print join("\t",$q,$energies[$q],"\n");

}

#if($number != 0){
#print join("\t", $totalNE, $number,"\n");
$averageNE = $totalNE/$number;
$smoothened[$p] = $averageNE;
#}
$p++;
#print $p,"\n";
```

```
#last if $q == 1367;
}
return (\@smoothened);
}
```

B. Data Analysis Scripts

B.I. Matlab NaI Gamma Analysis Scripts

Below are the MATLAB scripts used to analyze the NaI Gamma data. Please note that lines starting with "%" are comments.

```
%Bgnd file analysis
clear all
nb=input ('Enter here the number of bgnd files : ');
for i=1:1:nb
[filename1] = uigetfile(...
{'*.txt';'*.*'},'Select the 511 spectrum taken on the
   same day as bgnd');
clc;
fid=fopen(filename1,'r');
livetime=fscanf(fid,'%f',1);
realtime=fscanf(fid,'%f',1);
data=fscanf(fid,'%f',3765);
fclose(fid);
```

```
chn1=input ('Enter here the first channel which
   contains 511 peak : ');
chn2=input('Enter here the last channel which contains
   511 peak : ');
x1=chn1:1:chn2;
x1=x1';
y1=data((chn1+1):(chn2+1));
peakfit1=fit(x1,y1,'gauss1');
peak1=round(peakfit1.b1);
x=peak1-100:1:peak1+100+20;
x=x';
y=data((peak1-100+1):(peak1+100+20+1));
peakfit=fit(x,y,'gauss1');
gausspeak=double(peakfit.b1);
slope=double(511.0/gausspeak);
[filename1] = uigetfile(...
{'*.txt';'*.*'},'Select the corresponding bgnd spectrum
   ');
fid=fopen(filename1,'r');
livetime=fscanf(fid,'%f',1);
realtime=fscanf(fid,'%f',1);
data=fscanf(fid,'%f',3765);
fclose(fid);
data=double(data/livetime);
```

```
c70=fix((70/511.0)*gausspeak);
%energies selected from Mills paper
c448=fix((448.0/511.0)*gausspeak);
c588=fix((588.0/511.0)*gausspeak);
totint=0;
peakint=0;
for j=c70+1:c588+1
    totint=double(totint+data(j));
end
for j=c448+1:c588+1
    peakint=double(peakint+data(j));
end
bgndcalc(i,1)=double(totint);
bgndcalc(i,2)=double(peakint);
bgndcalc(i,3)=double(sqrt((totint/livetime)));
bgndcalc(i,4)=double(sqrt((peakint/livetime)));
clc;
end
avtot=0;
avtoterr=0;
avpeak=0;
avpeakerr=0;
for i=1:nb
avtot=double(bgndcalc(i,1)+avtot);
avpeak=double(bgndcalc(i,2)+avpeak);
```

```
avtoterr=double(bgndcalc(i,3)+avtoterr);
avpeakerr=double(bgndcalc(i,4)+avpeakerr);
end
avtot=double(avtot/nb);
avpeak=double(avpeak/nb);
avtoterr=double(avtoterr/nb);
avpeakerr=double(avpeakerr/nb);
[filename1, pathname]=uiputfile(...
{'*.txt';'*.*'},'Save calculated bagnd as');
fid=fopen(filename1,'w');
fprintf(fid,'%6.8f \t %6.8f \t %6.8f \t %6.8f \t %6.8f
   \t %6.8f \n', avtot, avtoterr, avpeak, avpeakerr,
   slope, (slope/511.0));
fclose(fid);

%NaI Data Analysis Code
clear all
bias=1;
[filename2] = uigetfile(...
{'*.txt';'*.*'},'Select the bgnd calc text file ');
dat=importdata(filename2, '\t', 0);
[filename1, pathname]=uiputfile(...
{'*.txt';'*.*'},'Save calculated values as');
fidwrite=fopen(filename1,'a');
c=1;
```

```
channel=0:1:3764;
channel=channel';
energy=channel*dat(:,5);
while (c ==1)
sample(bias)=input ('Enter here the sample bias ');
nfiles=input('Enter the number of files per bias ');
time1=0;
data1=zeros(3765,1);
for i=1:nfiles
    [filename3] = uigetfile(...
{'*.txt';'*.*'},'Select the corresponding 511 spectrum/
   s ');
clc;
fid=fopen(filename3,'r');
livetime=fscanf(fid,'%f',1);
realtime=fscanf(fid,'%f',1);
data=fscanf(fid,'%f',3765);
fclose(fid);
chn1=input ('Enter here the first channel which
   contains 511 peak : ');
chn2=input('Enter here the last channel which contains
   511 peak : ');
time1=time1+livetime;
x1=chn1:1:chn2;
x1=x1';
```

```
y1=data((chn1+1):(chn2+1));
peakfit1=fit(x1,y1,'gauss1');
peak1=round(peakfit1.b1);
x=peak1-100:1:peak1+100+20;
x=x';
y=data((peak1-100+1):(peak1+100+20+1));
peakfit=fit(x,y,'gauss1');
gausspeak=double(peakfit.b1);
slope=double(511.0/gausspeak);
energy_change=channel*slope;
intdata1=interp1(energy_change,data,energy);
data1=data1+intdata1;
pos=regexp(filename3,'T');
name=filename3(1:pos(:,1)-2);
savefile=strcat(name,'-interp','.txt');
fidsave2=fopen(savefile,'w');
    for j=1:1:3765
        fprintf(fidsave2,'%4.8f \t %4.8f \t %4.8f \t
           %4.8f \t %4.8f \t %4.8f \n',energy_change(j
           ,1),data(j,1),(data(j,1)/livetime),energy(j
           ,1),intdata1(j,1), (intdata1(j,1)/livetime))
           ;
    end
fclose(fidsave2);
end
```

```
data=data1;
data=double(data/time1);
gausspeak=511.0/dat(:,5);
c70=fix((70/dat(:,5)));
%energies selected from Mills paper
c448=fix((448.0/dat(:,5)));
c588=fix((588.0/dat(:,5)));
totint(bias)=0;
peakint(bias)=0;
for j=c70+1:c588+1
totint=double(totint+data(j));
end
for j=c448+1:c588+1
peakint=double(peakint+data(j));
end
totintbgndsub(bias)=double(totint(bias)-dat(:,1));
peakintbgndsub(bias)=double(peakint(bias)-dat(:,3));
errortotint(bias)=double(sqrt(totint(bias)/time1));
errorpeakint(bias)=double(sqrt(peakint(bias)/time1));
errortotintbgndsub(bias)=double(sqrt(errortotint(bias)
    ^2+dat(:,2)^2));
errorpeakintbgndsub(bias)=double(sqrt(errorpeakint(bias
    )^2+dat(:,4)^2));
R1(bias)=double((totintbgndsub(bias)-peakintbgndsub(
    bias))/totintbgndsub(bias));
```

```
R2(bias)=double((totintbgndsub(bias)-peakintbgndsub(
    bias))/peakintbgndsub(bias));
errorR1(bias)=double(R1(bias)*sqrt(((errortotintbgndsub
    (bias)+errorpeakintbgndsub(bias))/(totintbgndsub(
    bias)-peakintbgndsub(bias)))^2+(errortotintbgndsub(
    bias)/totintbgndsub(bias))^2));
errorR2(bias)=double(R2(bias)*sqrt(((errortotintbgndsub
    (bias)+errorpeakintbgndsub(bias))/(totintbgndsub(
    bias)-peakintbgndsub(bias)))^2+(errorpeakintbgndsub(
    bias)/peakintbgndsub(bias))^2));
clc;
fprintf(fidwrite,'%3.9f \t %3.9f \t %3.9f \t %3.9f \t
    %3.9f \t %3.9f \t %3.9f \t %3.9f \t %3.9f \t %3.9f \
    t %3.9f \t %3.9f \t %3.9f \t %3.9f \t %3.9f \t %3.9f
     \t %d \t %d \t %d\r\n', time1, gausspeak, dat(:,5),
     sample(bias), totint(bias),errortotint(bias),
    peakint(bias), errorpeakint(bias), totintbgndsub(
    bias), errortotintbgndsub(bias), peakintbgndsub(bias
    ), errorpeakintbgndsub(bias), R1(bias), errorR1(bias
    ), R2(bias), errorR2(bias), c70, c448, c588);
name=filename3(1:pos(:,1)-6);
savefile=strcat(name,'-added','.txt');
fidsave2=fopen(savefile,'w');
for j=1:1:3765
```

```
 fprintf(fidsave2,'%4.8f \t %4.8f \n',energy(j,1),data(
    j,1));
end
fclose(fidsave2);
bias=bias+1;
c=input('Do you wish to continue? (1=yes/any other=no)
    ');
previous_bias=sample(bias-1)
end
fclose(fidwrite);

%fclose(fidwrite);
```

B.II. Perl PAES Data Analysis Script

Below is the PERL script used to analyze the ToF-PAES data. Please note that lines starting with "#" are comments.

```
#PAES.pl - Perl script to analyze singles and added .
   SPE files:
#       User selects Gamma and PAES data files based on
    directory and fileextensions, time normalizes,
   background subtracts, and time normalizes the
   background subtracted data, normalizes to positrons,
    energy converts with sample bias subtraction and
   finally moving average smoothens then integrates
```

```
    over the energy windows and computes the statistical
     error bars.
#        Requires the output of Varghese matlab code for
     normalizing to positrons bgnd2_mod.m and
    nofpositrons_mod.m.
#        Subroutines used are listed at the end. They
    requires the Perl modules listed below.

use strict;
use warnings;
use Math::Expression::Evaluator;
use Math::Derivative qw(Derivative1 Derivative2);



####User Inputs####
my $PAESdirectory = "PAES DATA/SLG Data/Energy
    Calibration/";
#my $PAESdirectory = "PAES DATA/TiO2 Data/High Energy
    Settings/";
#my $PAESdirectory = "PAES DATA/TiO2 Data/Energy
    Calibration/";
my $NaIdirectory = "PAES DATA/SLG Data/Energy
    Calibration/NaI Data/";
#my $NaIdirectory = "PAES DATA/TiO2 Data/High Energy
    Settings/NaI Data/";
```

```
#my $NaIdirectory = "PAES DATA/TiO2 Data/Energy
    Calibration/NaI Data/";
my $PAESfileextension = ".SPE";
my $NaIfileextension = "mod.txt";
my $backgroundstart = 1750;
#Channel number to start calculating Dark Count BGND
my $backgroundend = 2000;
#Channel number to end calculating Dark Count BGND
#my @augerstart = (0,50,150,350,150);
#Si100 Auger 50; #Cu Auger 45(30); #C Auger 150; #O
    Auger 350
#my @augerend = (15,104,350,650,650);
#Si100 Auger 104; #Cu Auger 80(78); #C Auger 350; #O
    Auger 650
my $deltaE = 0.25;
#my $samplebias = 503;



####ToF-to-Energy conversion fucntions####
my $m = Math::Expression::Evaluator->new;
#Cu-ConstantEnergyShift
#$m->parse("(-1.6535930880008851+0.012477132380539296*x
    -0.00002664303200450523 2*x
    ^2+2.6791564457414093*10^-8*x
    ^3-1.2920428829657235*10^-11*x
```

```
    ^4+2.366019298513519*10^-15*x^5) ");
#my $infinity = 1577;
#TiO2
#$m->parse("(27.47770688899343-0.08958368463055119*x
    +0.00012149396938675213*x^2-8.274613129012091*10^-8*
    x^3+2.7896837118119555*10^-11*x
    ^4-3.7208162896304844*10^-15*x^5)");
#my $infinity = 1643;
#TiO2-HighEnergySettings
#$m->parse("(3.6253359078192644-0.011674661691127484*x
    +0.00001480829826984900 5*x
    ^2-8.893494401165527*10^-9*x
    ^3+2.469406401155257*10^-12*x
    ^4-2.4753477027811955*10^-16*x^5)");
#my $infinity = 1662;
#HOPG
#$m->parse("(34.8699-0.131095*x+0.0002061*x
    ^2-1.63837*10^-7*x^3+6.50396*10^-11*x
    ^4-1.0294*10^-14*x^5) ");
#my $infinity = 1573;
#High Res HOPG
#$m->parse("(0.668887-0.00180636*x+1.95031*10^-6*x
    ^2-8.53825*10^-10*x^3+1.11471*10^-13*x^4) ");
#my $infinity = 1615;
#Si100
```

```
#$m->parse("(27.266527286310513-0.08467307953238618*x
    +0.00011210328716733407*x^2-7.6169140426005*10^-8*x
    ^3+2.6039274925836055*10^-11*x
    ^4-3.566851650126058*10^-15*x^5) ");
#my $infinity = 1630;
#Cu
$m->parse("(60.863434308164-0.214658324681717*x
    +0.00031119480889550 8*x^2-2.27676724707788*10^-7*x
    ^3+8.33930743703305*10^-11*x
    ^4-1.22122881618327*10^-14*x^5) ");
my $infinity = 1579;
#Simulated Cu Settings
#$m->parse("(6.29994-0.0112773*x+8.22468*10^-6*x
    ^2-1.79226*10^-9*x^3-5.52773*10^-13*x
    ^4+2.06028*10^-16*x^5)");
#Cu Fit2-p3 shift
#$m->parse("(3.53274272478618+0.00493724169253676*x
    -2.59260977686436*10^-5*x^2+3.10952271139375*10^-8*x
    ^3-1.57795386522919*10^-11*x
    ^4+2.95342253827259*10^-15*x^5) ");



####SPE and Gamma file information####
my($sample) = $PAESdirectory =~ /(\/\S*)/;
```

```
$sample =~ s/\///;
my $cpscol = 8;
#Location of the Gamma CPS column
my $cpserrorcol = 9;
#Location of the Gamma CPS error column
my $numofMCAchannels = 2048;
#Number of MCA channels in the .SPE files
my $TAC = 4;
#TAC setting in microseconds
my $linestart = 13;
#First non-header line of .SPE files
my $lineend = 2061;
#Last non-header line of .SPE files
my $timeline = 10;
#Line where time is of .SPE files



####BEGIN CODE####
#Grab filenames from directories
opendir my $dir, $PAESdirectory or die "Cannot open
    $PAESdirectory: $!";
my @read = readdir($dir);
my @filenames = grep {/$PAESfileextension/i} @read;
closedir $dir;
```

```
opendir my $dir2, $NaIdirectory or die "Cannot open
    $NaIdirectory: $!";
my @read2 = readdir($dir2);
my @filenames2 = grep {/$NaIfileextension/i} @read2;
closedir $dir2;

#Prompt user for files to analyze and get samplebias
print "Type the numbers of the PAES files to analyze
    comma delimited.","\n";
for(my $i = 0; $i < scalar(@filenames); $i++){print
    join("\t",($i) . ".",$filenames[$i],"\n");}
chomp(my $usrinputs = <STDIN>);
my @usrinputs = split(/\s*,\s*/, $usrinputs);
for(my $i = 0; $i < scalar(@usrinputs); $i++){  print "
    you selected " . $filenames[$usrinputs[$i]],"\n";
            }
print "Is this correct? Type y for yes.","\n";
chomp(my $pause = <STDIN>);

my @tempsb = split("-",$filenames[$usrinputs[0]]);
my $matches = () = $tempsb[0] =~ /p/gi;
if($matches > 1){$tempsb[0] =~ s/p//;}
$tempsb[0] =~ s/p/./;
my($samplebias) = $tempsb[0];
my $tempsb2 = $samplebias;
```

```
$tempsb2 =~ s/\./p/;

print "Type the numbers of the NaI files to analyze
   comma delimited.","\n";
for(my $i = 0; $i < scalar(@filenames2); $i++){print
   join("\t",($i) . ".",$filenames2[$i],"\n");}
chomp(my $usrinputs2 = <STDIN>);
my @usrinputs2 = split(/\s*,\s*/, $usrinputs2);
for(my $i = 0; $i < scalar(@usrinputs2); $i++){ print "
   you selected " . $filenames2[$usrinputs2[$i]],"\n";
         }
print "Is this correct? Type y for yes.","\n";
chomp(my $pause2 = <STDIN>);



####BEGIN PAES ANALYSIS####
if($pause eq "y" && $pause2 eq "y"){

#IMPORT SINGLES GAMMA DATA
my (@posSINGLESCPS,@posSINGLESerror);
my $gammaSINGLESfile = $NaIdirectory . $filenames2[
   $usrinputs2[-1]];    #-1 element because added comes
    before singles in sorted array
my $singlesINDEX = 0;
```

```
open(posDATA, '<', $gammaSINGLESfile) or die "Can't
    open $gammaSINGLESfile: $!";
while(my $line = <posDATA>){
        chomp $line;
        my @rows = split(/       /,$line);
        $posSINGLESCPS[$singlesINDEX] = $rows[$cpscol];
        $posSINGLESerror[$singlesINDEX] = $rows[
            $cpserrorcol];
        $singlesINDEX++;
}
close posDATA;

#IMPORT SINGLES PAES DATA
my (@SINGLEStime,@SINGLESdata,@addedDATA,
    @SINGLESintensities);
for(my $i = 0; $i < $numofMCAchannels; $i++){
        $SINGLESdata[$i][0] = $addedDATA[$i][0]  = $i;
        $SINGLESdata[$i][1] = $addedDATA[$i][1] = ($TAC
            -($TAC*$i)/$numofMCAchannels)-($TAC-($TAC*
            $infinity)/$numofMCAchannels);
}
for(my $m = 0; $m < scalar(@usrinputs); $m++){
my $paesSINGLESfile = $PAESdirectory . $filenames[
    $usrinputs[$m]];
my $SINGLESindex = 0;
```

```
open(SINGLES, '<', $paesSINGLESfile) or die "Can't open
    $paesSINGLESfile: $!";
while(my $line = <SINGLES>){
        last if $. == $lineend;
        if($. == $timeline){
                my @rows = split(/ /,$line);
                $SINGLEStime[$m] = $rows[0];
        }
        next if $. < $linestart;
        chomp $line;
        $line =~ s/^\s+|\s+$//g; #Removes leading
           spaces and replaces with nothing
        $SINGLESdata[$SINGLESindex][2] = $line;
        $addedDATA[$SINGLESindex][2] += $line;
        $SINGLESindex++;
}
close SINGLES;

#Time Norm, BGND sub Time Norm, and Gamma Norm
my @chans = map $_ -> [0], @SINGLESdata;
my @ccounts = map $_ -> [2], @SINGLESdata;
my ($totalBGNDcountsref,$BGNDsuboutref) = BGNDAverage(
    $backgroundstart,$backgroundend,\@chans,\@ccounts);
   #@$ is the deference to a referenced array \@.
for (my $i = 0; $i < $numofMCAchannels; $i++)
```

```
{       $SINGLESdata[$i][3] = $SINGLESdata[$i][2] /
    $SINGLEStime[$m];
        $SINGLESdata[$i][4] = @$BGNDsuboutref[$i] /
            $SINGLEStime[$m];
        $SINGLESdata[$i][5] = $SINGLESdata[$i][4] /
            $posSINGLESCPS[$m];
}

#Energy conversion, smoothening and Auger intensity
    integration
my @positronnormccounts = map $_->[5], @SINGLESdata;
my ($energyoutref, $energycountsoutref) = EnergyConv(\
    @chans,\@positronnormccounts,$samplebias);
my $Smoothenoutref = Smoothen(\@$energyoutref,\
    @$energycountsoutref);
for(my $i = 0; $i < scalar(@$energyoutref); $i++)
{       $SINGLESdata[$i][6] = @$energyoutref[$i];
        $SINGLESdata[$i][7] = @$energycountsoutref[$i];
        if(defined @$Smoothenoutref[$i]) {$SINGLESdata[
            $i][8] = @$Smoothenoutref[$i];}
}
#my ($intensityref,$errorref) = AIntegrate(\@augerstart
    ,\@augerend,\@ccounts,\@$energyoutref,\
    @$Smoothenoutref,$SINGLEStime[$m],$posSINGLESerror[
    $m],$posSINGLESCPS[$m]);
```

```
#Print analyzed SINGLES PAES files
my $outputfilepath = $PAESdirectory . $tempsb2 . "_" .
    $sample . "_singles.txt";
open(OUT, '>>', $outputfilepath) or die "Can't open
    $outputfilepath: $!";
print OUT join("\t","Channel Number", "ToF (us)","
    Channel Counts - " . $filenames[$usrinputs[$m]],"
    Time Norm - " . $SINGLEStime[$m] . "(s)","BGND Sub
    Time Norm - " . $totalBGNDcountsref,"e+ Norm - " .
    $posSINGLESCPS[$m] . "(cps)","Energy (eV)","Energy
    Counts","Smoothened Counts - " . $deltaE . "eV","\n
    ");
for(@SINGLESdata){print OUT join("\t", @$_,"\n");} #The
     $_ is the current scalar reference to each element
    (row) of the array. @$_ gives the value associated
    with that scalar reference instead of the reference
    itself.
close OUT;
#Print intensity file
# my $intensitiesfilepath = $PAESdirectory . $tempsb2 .
     "_" . $sample . "_singles_Intensities.txt";
# open(OUT, '>>', $intensitiesfilepath) or die "Can't
    open $intensitiesfilepath: $!";
```

```
# print OUT join("\t","File","Start (eV)", "Stop (eV)
    ","Intensity","Error","\n");
# for(my $i = 0; $i < scalar(@$intensityref); $i++)
# {       print OUT join("\t", $filenames[$usrinputs[$m
    ]],$augerstart[$i],$augerend[$i],@$intensityref[$i],
    @$errorref[$i],"\n");   }
# close OUT;
}


#Begin added PAES analysis
if(scalar(@usrinputs) > 1){
#IMPORT ADDED GAMMA DATA
my ($posADDEDCPS,$posADDEDerror,$ADDEDtime);
my $gammaADDEDfile = $NaIdirectory . $filenames2[
    $usrinputs2[0]];        #0 element because added
    comes before singles in sorted array
my $addedINDEX = 0;
open(posDATA, '<', $gammaADDEDfile) or die "Can't open
    $gammaADDEDfile: $!";
while(my $line = <posDATA>){
        chomp $line;
        my @rows = split(/       /,$line);
        $posADDEDCPS = $rows[$cpscol];
        $posADDEDerror = $rows[$cpserrorcol];
```

```
        $addedINDEX++;
}
close posDATA;

#Time Norm, BGND sub Time Norm, and Gamma Norm
for(my $i = 0; $i < scalar(@SINGLEStime);$i++){
   $ADDEDtime += $SINGLEStime[$i];}
my @chans = map $_ -> [0], @addedDATA;
my @ccounts = map $_ -> [2], @addedDATA;
my ($totalBGNDcountsref,$BGNDsuboutref) = BGNDAverage(
   $backgroundstart,$backgroundend,\@chans,\@ccounts);
   #@$ is the deference to a scalar reference \@
for (my $i = 0; $i < $numofMCAchannels; $i++)
{       $addedDATA[$i][3] = $addedDATA[$i][2] /
   $ADDEDtime;
        $addedDATA[$i][4] = @$BGNDsuboutref[$i] /
            $ADDEDtime;
        $addedDATA[$i][5] = $addedDATA[$i][4] /
            $posADDEDCPS;
}

#Energy conversion, smoothening and Auger intensity
   integration
my @positronnormccounts = map $_ -> [5], @addedDATA;
```

```
my ($energyoutref, $energycountsoutref) = EnergyConv(\
    @chans,\@positronnormccounts,$samplebias);
my $Smoothenoutref = Smoothen(\@$energyoutref,\
    @$energycountsoutref);
for(my $i = 0;$i < scalar(@$energyoutref); $i++)
{       $addedDATA[$i][6] = @$energyoutref[$i];
        $addedDATA[$i][7] = @$energycountsoutref[$i];
        if(defined @$Smoothenoutref[$i]) {$addedDATA[$i
            ][8] = @$Smoothenoutref[$i];}
}
#my ($intensityref,$errorref) = AIntegrate(\@augerstart
    ,\@augerend,\@ccounts,\@$energyoutref,\
    @$Smoothenoutref,$ADDEDtime,$posADDEDerror,
    $posADDEDCPS);

#Print analyzed PAES files
my $outputfilepath = $PAESdirectory . $tempsb2 . "_" .
    $sample . "_added.txt";
open(OUT, '>>', $outputfilepath) or die "Can't open
    $outputfilepath: $!";
print OUT join("\t","Channel Number", "ToF (us)", "
    Channel Counts - added","Time Norm - " . $ADDEDtime
    . "(s)","BGND Sub Time Norm - " .
    $totalBGNDcountsref,"e+ Norm - " . $posADDEDCPS . "(
    cps)","Energy (eV)","Energy Counts","Smoothened
```

```
    Counts - " . $deltaE . "eV","\n");
for(@addedDATA){print OUT join("\t", @$_,"\n");}
close OUT;
#Print intensity file
# my $intensitiesfilepath = $PAESdirectory . $tempsb2 .
    "_" . $sample . "_added_Intensities.txt";
# open(OUT, '>>', $intensitiesfilepath) or die "Can't
    open $intensitiesfilepath: $!";
# print OUT join("\t","File", "Start (eV)", "Stop (eV)
    ","Intensity","Error","\n");
# for(my $i = 0 ;$i < scalar(@$intensityref); $i++)
# {      print OUT join("\t", $samplebias . "-added",
    $augerstart[$i],$augerend[$i],@$intensityref[$i],
    @$errorref[$i],"\n");      }
# close OUT;
        }
}
else{exit;}



#Prints runtime to command line
my $runtime = time() - $^T;
print "It took " . $runtime . " seconds.", "\n";
```

```
####subroutines####
sub BGNDAverage {
        my $start = shift;
        my $stop = shift;
        my $chansref = shift;
        my @chans = @$chansref;
        my $dataref = shift;
        my @data = @$dataref;
        my $sum = 0;
        my $count = 0;
        my @out;

        for(my $i = 0; $i < scalar(@data); $i++)
        {       if($chans[$i] >= $start && $chans[$i]
          <= $stop)
                {       $sum += $data[$i];
                        $count++;
                }
        }
        my $total = $sum / $count;
        for(my $i = 0; $i < scalar(@data); $i++)
        {       $out[$i] = $data[$i] - $total;  }
        return ($total,\@out);
}
```

```
sub EnergyConv {
        ##ToF-Energy conversion
        #Requires Math::Expression::Evaluator;
        my $channelsref = shift;
        my $channelcountsref = shift;
        my $samplebias = shift;
        my @channels = @$channelsref;
        my @channelcounts = @$channelcountsref;
        my (@y,@energy,@ecounts);

        for(my $i = 0; $i < scalar(@channels); $i++)
        {       my $chan = $channels[$i];
                $y[$i] = $m -> val({x => $chan});
        }
        my @dydx = Derivative1(\@channels,\@y);
        for(my $i = 0; $i < scalar(@channels); $i++)
        {       $energy[$i] = (1/($y[$i]**2))-
           $samplebias;
                $ecounts[$i] = $channelcounts[$i
                   ]*(-1/2)*($y[$i]**3)*(1/$dydx[$i]);
        }
        return(\@energy,\@ecounts);
}

sub Smoothen {
```

```
##Moving average energy smoothening
#Requires $deltaE defined
my $energiesref = shift;
my $ecountsref = shift;
my @energies = @$energiesref;
my @ecounts = @$ecountsref;
my $p = 0;
my $q = 0;
my @smoothened;
if(!defined $deltaE ){my $deltaE = 0.25;}

while($energies[$p] < 5000)
{       $q=$p;
        my $totalNE = 0;
        my $averageNE = 0;
        my $number = 0 ;
        while($energies[$q] < $energies[$p]+
           $deltaE)
        {       $totalNE += $ecounts[$q];
                $q++;
                $number++;
        }
        if($number != 0)
        {       $averageNE = $totalNE/$number;
                $smoothened[$p] = $averageNE;
```

```
                }
                $p++;
        }
        return (\@smoothened);
}

sub AIntegrate {
        #Computes Auger intensity with statistical
           error
        my $startref = shift;
        my $stopref = shift;
        my $ccountsref = shift;
        my $energiesref = shift;
        my $ecountsref = shift;
        my $time = shift;
        my $poserror = shift;
        my $poscps = shift;
        my @start = @$startref;
        my @end = @$stopref;
        my @ccounts = @$ccountsref;
        my @energies = @$energiesref;
        my @ecounts = @$ecountsref;
        my (@channelsum, @intensity, @error);

        for(my $j = 0; $j < scalar(@start); $j++)
```

```
        {       for(my $i = 0; $i < scalar(@ecounts);
            $i++)
                {       if($energies[$i] >= $start[$j]
                    && $energies[$i] <= $end[$j])
                        {       $channelsum[$j] +=
                            $ccounts[$i];           }
                }
                for(my $i = 0 ; $i < scalar(@ecounts);
                    $i++)
                {       if($energies[$i] >= $start[$j]
                    && $energies[$i] < $end[$j])
                        {       $intensity[$j] += .5*(
                            $energies[$i+1]-$energies[$i
                            ])*($ecounts[$i]+$ecounts[$i
                            +1]);       }
                }
                my $cpserror = sqrt($channelsum[$j])/
                    $time;
                my $cps = $channelsum[$j]/$time;
                $error[$j] = $intensity[$j]*sqrt((
                    $cpserror/$cps)**2+($poserror/
                    $poscps)**2);
        }
        return(\@intensity,\@error);
}
```

B.III. Perl Energy-to-ToF Script

Below is the PERL script used to take energy-converted data back into ToF space after shifting by the sample bias. Please note that lines starting with "#" are comments.

```
#PAES_SB.pl - Sample bias shifts, averages, convert to
    ToF


use strict;
use warnings;


####User Inputs####
#my $directory = "PAES DATA/HOPG Data/Energy
    Calibration/";
#my $directory = "PAES DATA/Si Data/";
my $BGNDfile = "CuO-model1";
my $file = "CuO-model1";
my $samplebiasFILE = 0.5;
my $infinity = 1579;
#Si 1630; #TiO2 1643; #HOPG 1573; #Cu 1579
my $mathematicalocation = 'C:\Program Files\Wolfram
    Research\Mathematica\12.0\Math.exe';
#New PC
#my $mathematicalocation = 'C:\Program Files\Wolfram
    Research\Mathematica\9.0\Math.exe';
#Alienware
```

```
my $energyrow = 0;
#6 for PAES file
my $ecountsrow = 1;
#7 for PAES file
#my $outputfilename = $directory . $file . "_BGND.txt";
my $outputfilename = $file . "_ToF.txt";

#my $channelstart = 60;
#my $augerstart = 150;
#Si100 Auger 50; #Cu Auger 45; #HOPG CKVV 174; #O Auger
    350
#my $augerend = 650;
#Si100 Auger 104; #Cu Auger 80; #HOPG CKVV 298; #O
   Auger 650
#my ($intensityref,$errorref) = AIntegrate(\@augerstart
   ,\@augerend,\@ccounts,\@$energyoutref,\
   @$Smoothenoutref,$ADDEDtime,$posADDEDerror,
   $posADDEDCPS);
my $numofMCAchannels = 2048; #Number of MCA channels in
    the .SPE files
my $TAC = 4; #TAC setting in microseconds

#Scale and sample bias shift bgndfile
my @SBshift;
my $intensityratio = 1;
```

```
#my $intensityratio = $intensityFILE / $intensityBGND;
my $k = 0;
#my $BGNDfileopen = $directory . $BGNDfile . ".txt";
my $BGNDfileopen = $BGNDfile . ".txt";
open(BGNDfile,'<', $BGNDfileopen) or die "Can't open
   $BGNDfileopen: $!";
while(my $line =<BGNDfile>)
{next if $. == 1;
chomp $line;
my @rows=split(/         /,$line);
$SBshift[$k][0] = $rows[$energyrow] + $samplebiasFILE;
$SBshift[$k][1] = $rows[$ecountsrow]*$intensityratio;
$k++;
last if $k == $infinity;
}
close BGNDfile;

#delete energycounts from channels 0 to $channelstart
# for(my $i = 0; $i < scalar(@SBshift); $i++){
# if($i <= $channelstart){
#print join("\t",$SBshift[$i][0] - $samplebiasFILE,
   $SBshift[$i][1] / $intensityratio,"\n");
# $SBshift[$i][1] = 0;
# }
# }
```

```
#TiO2  f[t_]:=27.47770688899343-0.08958368463055119*t
    +0.00012149396938675213*t^2-8.274613129012091*10^-8*
    t^3+2.7896837118119555*10^-11*t
    ^4-3.7208162896304844*10^-15*t^5;
#HOPG  f[t_]:=34.8699-0.131095*t+0.0002061*t
    ^2-1.63837*10^-7*t^3+6.50396*10^-11*t
    ^4-1.0294*10^-14*t^5;
#Cu  f[t_]:=60.863434308164-0.214658324681717*t
    +0.000311194808895508*t^2-2.27676724707788*10^-7*t
    ^3+8.33930743703305*10^-11*t
    ^4-1.22122881618327*10^-14*t^5;
#Si  f[t_]:=27.266527286310513-0.08467307953238618*t
    +0.00011210328716733407*t^2-7.6169140426005*10^-8*t
    ^3+2.6039274925836055*10^-11*t
    ^4-3.566851650126058*10^-15*t^5;


#Calls mathematica
my $shifted = "shifted_temp.txt";
```

```
open(OUT, '>>', $shifted) or die "Can't open $shifted:
    $!";
for(@SBshift){print OUT join("\t", @$_,"\n");}
close OUT;
my $tempfilename = "temp.txt";
open(TEMP, ">>", $tempfilename) or die "Can't open
    $tempfilename: $!";
print TEMP "SetDirectory[Directory[]];
elementJoin[a_, b_] := Transpose[{a, b}, RotateRight\
    @Range\@ArrayDepth\@{a, b}];
filename = \"shifted_temp.txt\";
input=Import[filename,\"Table\"];
f[t_]:=60.863434308164-0.214658324681717*t
    +0.000311194808895508*t^2-2.27676724707788*10^-7*t
    ^3+8.33930743703305*10^-11*t
    ^4-1.22122881618327*10^-14*t^5;
end=IntegerPart[t/.Solve[f[t]==0,t,Reals][[1]]];
cvalues={};dfdt={};dfde={};jacobian={};ccounts={};
For[i=1,i<=end,i++,AppendTo[cvalues,x/.Solve[f[x]==
    input[[i]][[1]]^-.5,x,Reals][[1]]]]
For[i=1,i<=Length[cvalues],i++,AppendTo[dfdt,f'[cvalues
    [[i]]]]]
For[i=1,i<=end,i++,AppendTo[dfde,-0.5*input[[i
    ]][[1]]^(-(3/2))]]
```

```
For[i=1,i<=end,i++,AppendTo[jacobian,1/dfde[[i]]*dfdt[[
    i]]]]
For[i=1,i<=end,i++,AppendTo[ccounts,jacobian[[i]]*input
    [[i]][[2]]]]
chans=elementJoin[cvalues,ccounts];
Export[\"out_temp.txt\",chans,\"Table\"];
Exit[]";
close TEMP;
system($mathematicalocation, -noprompt, -run, '<<temp.
    txt');


my @temp;
my $j=0;
open(MATHOUT,'<',"out_temp.txt") or die "Can't open
    out_temp.txt: $!";
while(my $line = <MATHOUT>)
{       chomp $line;
        my @rows=split(/        /,$line);
        $temp[$j][0] = $rows[0];
        $temp[$j][1] = $rows[1];
        $j++;
}
close MATHOUT;
```

```
#Average
my (@dataOUT,@dataOUT2);
my $start = int $temp[0][0];
my $stop = int $temp[-1][0];
my $m = 0;
for(my $i = $start; $i <= $stop; $i++)
{       my $temp = 0;
my $counter = 0;
for(my $j = 0; $j < scalar(@temp); $j++)
{       my $temp2 = int $temp[$j][0];
if($temp2 == $i)
{       $temp += $temp[$j][1];
        $counter++;
}
}
if($counter != 0){
$dataOUT[$m][0] = $i;
$dataOUT[$m][1] = $temp/$counter;
$m++;
}
}

for(my $i = 0; $i < scalar(@dataOUT); $i++)
{
```

```
$dataOUT2[$i][0] = $dataOUT[$i][0];
$dataOUT2[$i][1] = ($TAC-($TAC*$dataOUT[$i][0])/
    $numofMCAchannels)-($TAC-($TAC*$infinity)/
    $numofMCAchannels);
$dataOUT2[$i][2] = $dataOUT[$i][1];

}

open(OUT, '>>', $outputfilename) or die "Can't open
    $outputfilename: $!";
for(@dataOUT2){print OUT join("\t", @$_,"\n");}
close OUT;

#Delete temp files
unlink "out_temp.txt";
unlink $shifted;
unlink $tempfilename;
#Prints runtime to command line
my $runtime = time() - $^T;
print "It took " . $runtime . " seconds.", "\n";



sub AIntegrate {
#Computes Auger intensity with statistical error
```

```
my $startref = shift;
my $stopref = shift;
my $ccountsref = shift;
my $energiesref = shift;
my $ecountsref = shift;
my $time = shift;
my $poserror = shift;
my $poscps = shift;
my @start = @$startref;
my @end = @$stopref;
my @ccounts = @$ccountsref;
my @energies = @$energiesref;
my @ecounts = @$ecountsref;
my (@channelsum, @intensity, @error);

for(my $j = 0; $j < scalar(@start); $j++)
{
for(my $i = 0; $i < scalar(@ecounts); $i++)
{if($energies[$i] >= $start[$j] && $energies[$i] <=
   $end[$j])
{$channelsum[$j] += $ccounts[$i];}
}
for(my $i = 0 ; $i < scalar(@ecounts); $i++)
{if($energies[$i] >= $start[$j] && $energies[$i] < $end
   [$j])
```

```
{$intensity[$j] += .5*($energies[$i+1]-$energies[$i])*(
    $ecounts[$i]+$ecounts[$i+1]);}
}
my $cpserror = sqrt($channelsum[$j])/$time;
my $cps = $channelsum[$j]/$time;
$error[$j] = $intensity[$j]*sqrt(($cpserror/$cps)**2+(
    $poserror/$poscps)**2);
}
return(\@intensity,\@error);
}
```

References

[1] M. J. Puska and R. M. Nieminen. "Theory of positrons in solids and on solid surfaces". In: *Reviews of Modern Physics* (1994). DOI: 10.1103/RevModPhys.66.841.

[2] Peter J. Schultz and K. G. Lynn. "Interaction of positron beams with surfaces, thin films, and interfaces". In: *Reviews of Modern Physics* (1988). DOI: 10.1103/RevModPhys.60.701.

[3] Christoph Hugenschmidt. "Positrons in surface physics". In: *Surface Science Reports* 71.4 (2016), pp. 547–594. DOI: 10.1016/j.surfrep.2016.09.002. arXiv: 1611.04430.

[4] J. A. Baker, M. Touat, and P. G. Coleman. "Branching ratios for electron-volt positrons at a cu(110) surface". In: *Journal of Physics C: Solid State Physics* 21.26 (1988), pp. 4713–4720. DOI: 10.1088/0022-3719/21/26/019.

[5] David E. Ramaker. "The past, present, and future of auger line shape analysis". In: *Critical Reviews in Solid State and Materials Sciences* 17.3 (1991), pp. 211–276. DOI: 10.1080/10408439108243752.

[6] S. Mukherjee et al. "Time of flight spectrometer for background-free positron annihilation induced Auger electron spectroscopy". In: *Review of Scientific Instruments* 87.3 (2016), p. 035114. DOI: 10.1063/1.4943858.

[7] S. F. Mukherjee, K. Shastry, and A. H. Weiss. "Predominance of multielectron processes contributing to the intrinsic spectra of low-energy Auger transitions in copper and gold". In: *Physical Review B - Condensed Matter and Materials Physics* 84.15 (2011), pp. 1–6. DOI: 10.1103/PhysRevB.84.155109.

[8] E. Jensen et al. "Origin of the low-energy tail in the Al L2,3VV Auger spectrum studied with Auger-photoelectron coincidence spectroscopy". In: *Phys. Rev. B* 45.23 (1992), pp. 13636–13641. DOI: 10.1103/PhysRevB.45.13636.

[9] S. Satyal et al. "Measurement of the background in Auger-photoemission coincidence spectra (APECS) associated with inelastic or multi-electron valence band photoemission processes". In: *J. Electron Spectros. Relat. Phenomena* 195 (2014), pp. 66–70. DOI: 10.1016/j.elspec.2014.05.010.

[10] G. Stefani et al. "Dynamic Screening Probed by Core-Resonant Double Photoemission from Surfaces". In: *Phys. Rev. Lett.* 113.26 (2014). DOI: 10.1103/physrevlett.113.267603.

[11] P.V. Joglekar et al. "Measurement of the full electron spectrum associated with the Ag N3VV Auger transitions: Evidence for the contribution

of multi-electron Auger processes". In: *J. Electron Spectros. Relat. Phenomena* (2019). DOI: 10.1016/j.elspec.2019.06.006.

[12] David Mehl et al. "Sensitivity of positron-annihilation-induced Auger-electron spectroscopy to the top surface layer". In: *Physical Review B* (1990). DOI: 10.1103/PhysRevB.41.799.

[13] V. A. Chirayath et al. "Auger electron emission initiated by the creation of valence-band holes in graphene by positron annihilation". In: *Nature Communications* 8.May (2017), pp. 1–7. DOI: 10.1038/ncomms16116.

[14] Alex H. Weiss et al. "Method for the measurement of positron affinities and positron work functions suitable for both positive and negative work function materials". In: *Applied Surface Science* 85 (1995), pp. 82–86. DOI: 10.1016/0169-4332(94)00313-0.

[15] Shuping Xie. "Positron annihilation induced Auger electron spectroscopy of inner shell transitions using the time-of-flight technique". PhD thesis. 2002.

[16] P. Kruit and F. H. Read. "Magnetic field paralleliser for 2?? electron-spectrometer and electron-image magnifier". In: *Journal of Physics E: Scientific Instruments* (1983). DOI: 10.1088/0022-3735/16/4/016.

[17] D. O. Van Ostenburg and D. J. Montgomery. "Charge Transfer Upon Contact Between Metals and Insulators". In: *Textile Research Journal* 28.1 (1958), pp. 22–31. DOI: 10.1177/004051755802800103.

[18] V A Chirayath et al. "A multi-stop time-of-flight spectrometer for the measurement of positron annihilation-induced electrons in coincidence

with the Doppler-shifted annihilation gamma photon". In: *Review of Scientific Instruments* 91.3 (2020), p. 033903. DOI: 10.1063/1.5140789.

[19] D. E. Ramaker, J. S. Murday, and N. H. Turner. "Extracting Auger lineshapes from experimental data". In: *Journal of Electron Spectroscopy and Related Phenomena* 17.1 (1979), pp. 45–65. DOI: 10.1016/0368-2048(79)85026-4.

[20] A. J. Fairchild et al. "Modelling the line shape of very low energy peaks of positron beam induced secondary electrons measured using a time of flight spectrometer". In: *Journal of Physics: Conference Series*. Vol. 791. 2017. DOI: 10.1088/1742-6596/791/1/012030.

[21] Chun Lei et al. "Apparatus for positron annihilation-induced Auger electron spectroscopy". In: *Review of Scientific Instruments* 60.12 (1989), pp. 3656–3660. DOI: 10.1063/1.1140471.

[22] S. Doukas et al. "Determination of the solid angle and response function of a hemispherical spectrograph with injection lens for Auger electrons emitted from long lived projectile states". In: *Rev. Sci. Instrum.* 86.4 (2015). DOI: 10.1063/1.4917274.

[23] Qi Zhang, Kun Zhao, and Zenghu Chang. "High resolution electron spectrometers for characterizing the contrast of isolated 25 as pulses". In: *J. Electron Spectros. Relat. Phenomena* 195 (2014), pp. 48–54. DOI: 10.1016/j.elspec.2014.05.008.

[24] Todd T. King et al. "Simulation of a miniature, low-power time-of-flight mass spectrometer for in situ analysis of planetary atmospheres". In: *Proc. SPIE 6959, Micro (MEMS) and Nanotechnologies for Space,*

Defense, and Security II, 69590E 6959 (2008). DOI: 10.1117/12.780113.

[25] Z.-X. Shen et al. "Electronic structure of NiO: Correlation and band effects". In: *Physical Review B* 44.8 (1991), pp. 3604–3626. DOI: 10.1103/PhysRevB.44.3604.

[26] Nobuyuki Ishida and Daisuke Fujita. "Chemical-state imaging of Li using scanning Auger electron microscopy". In: *Journal of Electron Spectroscopy and Related Phenomena* 186.1 (2013), pp. 39–43. DOI: 10.1016/j.elspec.2013.03.001.

[27] N. Nakajima et al. "Photoemission study of the modification of the electronic structure of transition-metal overlayers on TiO2 surfaces III. Ni on TiO2(001) and Cu on TiO2(110)". In: *Surface Science* 561.1 (2004), pp. 93–100. DOI: 10.1016/j.susc.2004.04.049.

[28] S. Mukherjee et al. "Auger-mediated sticking of positrons to surfaces: Evidence for a single-step transition from a scattering state to a surface image Potential bound State". In: *Physical Review Letters* 104.24 (2010), pp. 1–4. DOI: 10.1103/PhysRevLett.104.247403.

[29] T. Sekine et al. *Handbook of Auger Electron Spectroscopy*. Akishima Tokyo Japan: JEOL LTD., 1982.

[30] Zongxian Yang, Ruqian Wu, and D. W. Goodman. "Structural and electronic properties of Au on TiO2(110)". In: *Physical Review B* 61.20 (2002), pp. 14066–14071. DOI: 10.1103/physrevb.61.14066.

[31] M. L. Knotek and Peter J. Feibelman. "Ion Desorption by Core-Hole Auger Decay". In: *Physical Review Letters* 40.14 (1978), pp. 964–967. DOI: 10.1103/PhysRevLett.40.964.

[32] S. Barth et al. "The efficiency of Interatomic Coulombic Decay in Ne clusters". In: *Chemical Physics* 329.1-3 (2006), pp. 246–250. DOI: 10.1016/j.chemphys.2006.06.035.

[33] Petras Juzenas et al. "Quantum dots and nanoparticles for photodynamic and radiation therapies of cancer". In: *Advanced Drug Delivery Reviews* 60.15 (2008), pp. 1600–1614. DOI: 10.1016/j.addr.2008.08.004.

[34] Antonius de Rooij. "Corrosion in Space". In: *Encyclopedia of Aerospace Engineering*. American Cancer Society, 2010. ISBN: 9780470686652. DOI: 10.1002/9780470686652.eae242. eprint: https://onlinelibrary.wiley.com/doi/pdf/10.1002/9780470686652.eae242.

[35] George Adam Zacheis, Kimberly A. Gray, and Prashant V. Kamat. "Radiation-induced catalysis on oxide surfaces: Degradation of hexachlorobenzene on γ-irradiated alumina nanoparticles". In: *Journal of Physical Chemistry B* 103.12 (1999), pp. 2142–2150. DOI: 10.1021/jp990211u.

[36] N. G. Fazleev, J. L. Fry, and A. H. Weiss. "Positrons as probes of Si(100) surface with adsorbed hydrogen and oxygen". In: *Radiation Physics and Chemistry* 58.5-6 (2000), pp. 659–665. DOI: 10.1016/S0969-806X(00)00234-6.

[37] N. G. Fazleev et al. "Oxidation and thermal reduction of the Cu(1 0 0) surface as studied using positron annihilation induced Auger electron spectroscopy (PAES)". In: *Surface Science* 604.1 (2010), pp. 32–37. DOI: 10.1016/j.susc.2009.10.016.

[38] J. H. Kim, G. Yang, and A. H. Weiss. "Study of the adsorption of hydrogen and oxygen on Si(100) using positron-annihilation induced Auger electron spectroscopy (PAES)". In: *Surface Science* 396.1-3 (1998), pp. 388–393. DOI: 10.1016/S0039-6028(97)00692-4.

[39] M.P. Nadesalingam et al. "Study of cuprous oxide using time of flight positron annihilation induced Auger electron spectroscopy". In: *Physica Status Solidi (C) Current Topics in Solid State Physics* 4.10 (2007), pp. 3932–3934. DOI: 10.1002/pssc.200675859.

[40] M. P. Nadesalingam et al. "Effect of vacuum annealing on the surface chemistry of electrodeposited copper(I) oxide layers as probed by positron annihilation induced Auger electron spectroscopy". In: *Langmuir* 23.4 (2007), pp. 1830–1834. DOI: 10.1021/la062709a.

[41] Takayuki Tachibana et al. "Efficient and surface site-selective ion desorption by positron annihilation". In: *Scientific Reports* 8.1 (2018), pp. 1–3. DOI: 10.1038/s41598-018-25506-5.

[42] T Yamashita et al. "Experimental and computational studies of positron-stimulated ion desorption from TiO 2 (1 1 0) surface". In: *Materials Research Express* 4.11 (2017), p. 116303. DOI: 10.1088/2053-1591/aa9454.

[43] V. Baglin et al. "the Secondary Electron Yield of Technical Materials and Its Variation With Surface Treatments". In: *Epac 2000* September 2000 (2000), pp. 217–221.

[44] J.J. Fijol et al. "Secondary electron yield of SiO2 and Si3N4 thin films for continuous dynode electron multipliers". In: *Applied Surface Science* 48-49 (1991), pp. 464–471. DOI: https://doi.org/10.1016/0169-4332(91)90376-U.

[45] Masahide Ohno. "Many-body theory of the Auger Auger-electron coincidence spectroscopy (AAECS) spectra of solids". In: *Chemical Physics* 393.1 (2012), pp. 74–79. DOI: 10.1016/j.chemphys.2011.11.028.

[46] J. Ghijsen et al. "Electronic structure of Cu2O and CuO". In: *Physical Review B* 38.16 (1988), pp. 11322–11330. DOI: 10.1103/PhysRevB.38.11322.

[47] P. Steiner et al. "Photoemission valence band spectra and electronic density of states in copper oxides and copper based ceramic superconductors". In: *Zeitschrift für Physik B Condensed Matter* 74.2 (1989), pp. 173–182. DOI: 10.1007/BF01307383.

[48] G. A. van Riessen, S. M. Thurgate, and D. E. Ramaker. "Auger-photoelectron coincidence spectroscopy of SiO2". In: *Journal of Electron Spectroscopy and Related Phenomena* 161.1-3 SPEC. ISS. (2007), pp. 150–159. DOI: 10.1016/j.elspec.2007.02.028.

[49] Yu.A Teterin et al. "Auger and X-ray photoelectron spectroscopy study of the density of oxygen states in bismuth, aluminium, silicon and uranium oxides". In: *Journal of Electron Spectroscopy and Related Phenom-*

ena 101-103 (1999), pp. 401–405. DOI: 10.1016/S0368-2048(98)00405-8.

[50] R. Ruus et al. "Resonant Auger spectra of TiO2 at Ti 2p and O 1s absorption edges". In: *Journal of Electron Spectroscopy and Related Phenomena* 93.1-3 (1998), pp. 193–199. DOI: 10.1016/s0368-2048(98)00174-1.

[51] E. L. D. Hebenstreit et al. "Sulfur on TiO2(110) studied with resonant photoemission". In: *Physical Review B* 64.11 (2001), p. 115418. DOI: 10.1103/PhysRevB.64.115418.

[52] Homer D. Hagstrum. "Theory of auger ejection of electrons from metals by ions". In: *Physical Review* 96.2 (1954), pp. 336–365. DOI: 10.1103/PhysRev.96.336.

[53] Homer D. Hagstrum. "Theory of auger neutralization of ions at the surface of a diamond-type semiconductor". In: *Physical Review* 122.1 (1961), pp. 83–113. DOI: 10.1103/PhysRev.122.83.

[54] Vincent Callewaert. "Development and application of a non-local theory for the description of positron surface states". PhD thesis. 2018.

[55] D. E. Ramaker et al. "Calculated and measured Auger line shapes in SiO_2". In: *Phys. Rev. B* 19 (10 1979), pp. 5375–5387. DOI: 10.1103/PhysRevB.19.5375.

[56] Masahide Ohno. "Effect of relaxation and decay of a charge transfer shakeup satellite on Auger-electron spectroscopy spectra and Auger-photoelectron coincidence spectroscopy spectra of adsorbates". In: *Jour-*

nal of Electron Spectroscopy and Related Phenomena 162.2 (2008), pp. 83–98. DOI: 10.1016/j.elspec.2007.08.009.

[57] J. J. Lander. "Auger peaks in the energy spectra of secondary electrons from various materials". In: *Physical Review* 91.6 (1953), pp. 1382–1387. DOI: 10.1103/PhysRev.91.1382.

[58] A. H. Weiss et al. "Modeling of the energy spectra of individual steps of the L23 → M2,3M2,3 → M2,3VV → VVVV cascade chain in MnO". In: *Journal of Electron Spectroscopy and Related Phenomena* 161 (2007), pp. 160–163. DOI: 10.1016/j.elspec.2007.03.011.

[59] M. Salmerón, A. M. Baró, and J. M. Rojo. "Interatomic transitions and relaxation effects in Auger spectra of several gas adsorbates on transition metals". In: *Physical Review B* 13.10 (1976), pp. 4348–4363. DOI: 10.1103/PhysRevB.13.4348.

[60] Melanie Mucke et al. "A hitherto unrecognized source of low-energy electrons in water". In: *Nature Physics* 6.2 (2010), pp. 143–146. DOI: 10.1038/nphys1500.

[61] S Tanaka et al. "Electron–ion coincidence study for the TiO2(110) surface". In: *Surface Science* 451.1-3 (2000), pp. 182–187. DOI: 10.1016/S0039-6028(00)00025-X.

[62] M. P. Seah. "Quantitative Auger electron spectroscopy and electron ranges". In: *Surface Science* 32 (1972), pp. 703–728. DOI: 10.1016/0039-6028(72)90196-3.

[63] Eugene J. McGuire. "K-Shell Auger Transition Rates and Fluorescence Yields for Elements Be-Ar". In: *Physical Review* 185.1 (1969), pp. 1–6. DOI: 10.1103/PhysRev.185.1.

[64] Eugene J. McGuire. "Atomic L-shell coster-kronig, auger, and radiative rates and flourescence yields for Na-Th". In: *Physical Review A* 3.2 (1971), pp. 587–594. DOI: 10.1103/PhysRevA.3.587.

[65] Ulrike Diebold. "The surface science of titanium dioxide". In: *Surface Science Reports* 48.5-8 (2003), pp. 53–229. DOI: 10.1016/S0167-5729(02)00100-0.

[66] M. P. Seah and W. A. Dench. "Quantitative electron spectroscopy of surfaces: A standard data base for electron inelastic mean free paths in solids". In: *Surface and Interface Analysis* 1.1 (1979), pp. 2–11. DOI: 10.1002/sia.740010103.

[67] Kjeld O. Jensen and A. Weiss. "Theoretical study of the application of positron-induced Auger-electron spectroscopy". In: *Physical Review B* 41.7 (1990), pp. 3928–3936. DOI: 10.1103/PhysRevB.41.3928.

[68] P. A. Sterne, P. Asoka-Kumar, and R. H. Howell. "Atomic-based calculations of two-detector Doppler-broadening spectra". In: *Applied Surface Science* 194.1-4 (2002), pp. 71–75. DOI: 10.1016/S0169-4332(02)00091-0.

[69] P. A. Sterne and J. H. Kaiser. "First-principles calculation of positron lifetimes in solids". In: *Physical Review B* 43.17 (1991), pp. 13892–13898. DOI: 10.1103/PhysRevB.43.13892.

[70] B Barbiellini et al. "Calculation of positron states and annihilation in solids: A density-gradient-correction scheme". In: *Physical Review B* 53.24 (1996), pp. 16201–16213. DOI: 10.1103/PhysRevB.53.16201.

[71] H. E. Bishop and J. C. Rivière. "Estimates of the Efficiencies of Production and Detection of Electron-Excited Auger Emission". In: *Journal of Applied Physics* 40.4 (1969), pp. 1740–1744. DOI: 10.1063/1.1657841.

[72] Badia Boudaïffa et al. "Resonant formation of DNA strand breaks by low-energy (3 to 20 eV) electrons". In: *Science* 287.5458 (2000), pp. 1658–1660. DOI: 10.1126/science.287.5458.1658.

[73] Xiao Chu et al. "Exploration of TiO2 nanoparticle mediated microdynamic therapy on cancer treatment". In: *Nanomedicine: Nanotechnology, Biology, and Medicine* 18 (2019), pp. 272–281. DOI: 10.1016/j.nano.2019.02.016.

[74] Hironobu Saito and Yoshio Nosaka. "Mechanism of singlet oxygen generation in visible-light-induced photocatalysis of gold-nanoparticle-deposited titanium dioxide". In: *Journal of Physical Chemistry C* 118.29 (2014), pp. 15656–15663. DOI: 10.1021/jp502440f.

[75] T. Jahnke et al. "Ultrafast energy transfer between water molecules". In: *Nature Physics* 6.2 (2010), pp. 139–142. DOI: 10.1038/nphys1498.

[76] Ivano Tavernelli et al. "Time-dependent density functional theory molecular dynamics simulations of liquid water radiolysis". In: *ChemPhysChem* 9.14 (2008), pp. 2099–2103. DOI: 10.1002/cphc.200800177.

[77] C. N. Berglund and W. E. Spicer. "Photoemission studies of copper and silver: Experiment". In: *Physical Review* 136.4A (1964), A1044–A1064. DOI: 10.1103/PhysRev.136.A1044.

[78] Simone Taioli et al. "Electron spectroscopies and inelastic processes in nanoclusters and solids: Theory and experiment". In: *Physics Reports* 493.5 (2010), pp. 237–319. DOI: 10.1016/j.physrep.2010.04.003.

[79] L. M. Malard et al. "Raman spectroscopy in graphene". In: *Physics Reports* 473.5-6 (2009), pp. 51–87. DOI: 10.1016/j.physrep.2009.02.003.

[80] V A Chirayath et al. "Positronium formation in graphene and graphite". In: vol. 050002. December. 2019, p. 050002. ISBN: 9780735419292. DOI: 10.1063/1.5135845.

List of Publications and Conferences Attended

Selected Publications

1. R.W. Gladen, V.A. Chirayath, A.J. Fairchild, A.R. Koymen, and A.H. Weiss, "*Digital methods for the coincident measurement ofthe energies of positron-induced electrons and Doppler-shifted annihilation gamma quanta*", Nucl. Instrum. Meth. A, 953, 162887 (2020). `https://doi.org/10.1016/j.nima.2019.162887`

2. V.A. Chirayath, R.W. Gladen, A.D. McDonald, A.J. Fairchild, P.V. Joglekar, S. Satyal, Z.H. Lim, T.N. Shead, M.D. Chrysler, S. Mukherjee, B.M. Barnett, N.K. Byrnes, A.R. Koymen, R.G. Greaves, and A.H. Weiss, "*A multi-stop time-of-flight spectrometer for the measurement of positron annihilation-induced electrons in coincidence with the Doppler-shifted annihilation gamma photon*", Rev. Sci., 91, 033903 (2020). `https://doi.org/10.1063/1.5140789`

3. P.V. Joglekar, R.W. Gladen, V.A. Chirayath, A.J. Fairchild, S. Kalaskar, K. Shastry, Q. Dong, S.L. Hulbert, R.A. Bartynski, W.S.M. Werner, and

A.H. Weiss, "*Measurement of the full electron spectrum associated with the Ag N3VV Auger transitions: Evidence for the contribution of multi-electron Auger processes*", J. Electron Spectros. Relat. Phenomena, 235, 16-22 (2019). https://doi.org/10.1016/j.elspec.2019.06.006

4. V.A. Chirayath, V. Callewaert, A.J. Fairchild, M.D. Chrysler, R.W. Gladen, A.D. McDonald, S.K. Imam, K. Shastry, A.R. Koymen, R. Saniz, B. Barbiellini, K. Rajeshwar, B. Partoens, and A.H. Weiss, "*Auger electron emission initiated by the creation of valence-band holes in graphene by positron annihilation*", Nat. Commun., 8, 16116 (2017). https://doi.org/10.1038/ncomms16116

International Conferences Attended

1. 15th International Workshop on Slow Positron Beam Techniques & Applications (SLOPOS-15) held in Prague, Czech Republic on September 2-6, 2019.

2. 18th International Conference on Positron Annihilation (IPCA-18) held in Orlando, Florida on August 19-24, 2018.

3. American Physics Society (APS) March Meeting held in Los Angeles, California on March 5-9, 2018.

4. Sources Interaction with Matter Detection and Analysis of Low Energy Electrons 2 (SIMDALEE-2) held in Sardinia, Italy on September 18-22, 2017.

5. American Physics Society (APS) March Meeting held in New Orleans, Louisiana on March 13-17 2017.

6. 14^{th} International Workshop on Slow Positron Beam Techniques & Applications (SLOPOS-15) held in Matsue, Japan on May 22-27 2016.

7. American Physics Society (APS) March Meeting held in Baltimore, Maryland on March 14-18 2016.

Peer Reviewed Proceedings from International Conferences

1. A.J. Fairchild, V.A. Chirayath, R.W. Gladen, A.R. Koymen, and A.H. Weiss, "*Positron Annihilation-Induced Auger Electron Spectroscopy Measurements of a TiO_2(110) Surface*", Acta Phys. Pol. A, 137, 87-90 (2020). `https://doi.org/10.1088/1742-6596/791/1/012030`

2. A.J. Fairchild, V.A. Chirayath, R.W. Gladen, A.R. Koymen, and A.H. Weiss, "*Modelling the line shape of very low energy peaks of positron beam induced secondary electrons measured using a time of flight spectrometer*", J. Phys.: Conf. Ser., 791, 012030 (2017). `https://doi.org/10.1088/1742-6596/791/1/012030`

3. A.J. Fairchild, V.A. Chirayath, R.W. Gladen, A.R. Koymen, and A.H. Weiss, AIP Conf. Proc., 2182, 050003 (2019). "*Positron Induced Electron Emission from Graphite*". `https://doi.org/10.1063/1.5135846`

Biographical Information

Alexander Jarrett Fairchild graduated with a Bachelor of Science degree in Physics and a Bachelor of Science degree in Pure Mathematics from the University of Texas at Austin in 2013. He joined the physics department of the University of Texas at Arlington in Fall 2015 as a PhD candidate.